CRYSTALLIZATION IN HARD SPHERE COLLOIDAL SYSTEMS

By

YUEMING HE

Bachelor of Science
South China Normal University
Guangzhou, China
1982

Master of Science
South China Normal University
Guangzhou, China
1987

Submitted to the Faculty of the
Graduate College of the
Oklahoma State University
in partial fulfillment of
the requirements for
the Degree of
DOCTOR OF PHILOSOPHY
December, 1996

CRYSTALLIZATION IN HARD SPHERE
COLLOIDAL SYSTEMS

Thesis Approved:

Thesis Adviser

Dean of the Graduate College

ACKNOWLEDGMENTS

I wish to express my sincere appreciation to my advisor, Dr. Bruce J. Ackerson, for giving me the opportunity to work in his laboratory and for his patient, tireless support, advice and help throughout this work at Oklahoma State University. Many thanks also go to my other Ph. D. Advisory Committee members, Dr. H. L. Scott, Dr. Paul Westhaus, Dr. Penger Tong and Dr. Warren T. Ford. for their helpful suggestions and criticism.

I also want to show my gratitude to my fellow graduate students, Ulf, Keith, Greg and Steven, working together in the laboratory for their timely help and encouragement as well as friendly environment.

Special thanks also go to Mr. Ulf Nobbmann. He helped me to format this dissertation – while he is writing his own dissertation.

This work was support by National Science Foundation and NASA.

Thanks also go to my parents and brother for their love and encouragement.

To my wife, Qiaoping, my sons: Jason and Justin, I wish to express my deep appreciation for the support and love you showed me. I wonder whether I could ever finished this work if they had not sacrificed so much. Thank you to all.

TABLE OF CONTENTS

LIST OF TABLES

LIST OF FIGURES

CHAPTER I

INTRODUCTION

Colloidal Systems

A colloid system or colloid suspension consists of particles having size of about $10^{-9}m$ to $10^{-6}m$, which are dispersed in a liquid. The examples are soap solutions, emulsions, solutions of proteins and synthetic systems such as polystyrene, TPM-silica[1] and poly-(methylmethacrylate) (PMMA)[2] dispersions. The size of the colloidal particles is much larger compared with the solvent particles which are molecular size, so that the colloidal particles are subjected to Brownian motion due to the random kicks by the solvent molecules. The particle size is sufficiently small that the particles' Brownian motion dominates over the sedimentation or convection. A colloidal system may be considered as supermolecular fluid in which the colloidal particles play the role of molecules. The solvent is treated as a continuous background that gives rise to fluctuating forces between the colloidal particles. The effect of averaging over the background solvent gives rise to a potential of mean force, or an effective pair potential of the colloidal particles. Statistical mechanics can be used to calculate the properties of a colloidal system with its effective pair potential of the particles.

Colloidal Particles and Interparticle Forces

There are three major kinds of interparticle forces in the colloidal systems. We can classify colloidal systems into two classes by the different stabilization mechanisms: charge and steric stabilization. The attractive van der Waals force is the same for each class.

Van der Waals Attraction

Van der Waals Attraction is a dipole-induced-dipole attraction. It has the form for two particles with separation distance r as

$$V_A(r) = -\frac{A}{6}[\frac{2a^2}{r^2-2a^2} + \frac{2a^2}{r^2} + ln(1-\frac{4a^2}{r^2})] \tag{1.1}$$

where a is the radius of the particles and A is a constant determined mainly by the polarisabilities of particles and solvent. Thus, if the particles and suspension medium of the system are index matched, $A \rightarrow 0$, then van der Waals attraction can be omitted. From the equation (1.1), we can see that the attraction vanishes as r^{-6} and is infinite at particle contact ($r = 2a$).

If the van der Waals attraction was the only force in the colloidal system, the particles would aggregate. Therefore, an additional stabilizing force is required to keep the particles from sticking together. Two different stabilization methods are available for colloidal systems, charged stabilization and steric stabilization.

Charged Colloidal System and Electrical Force

For charge stabilized systems, particles carry electrical charges on their surface which forms an electric double layer. They can be called "macroions". The electric double layer was formed when some of the ionisable groups on the particle surface dissociated in polar solvents such as water but remained near the surface of the particles. Two macroions repelled each other when they approached due to the Coulomb repulsion from their overlapping electric double layers.

The system is hard to characterize since the charges carried by each particle are unknown. A simple effective pairwise potential of the double layer can be expressed with the "DLVO" potential[3,4]. The DLVO potential has two parts which are van der Waals attraction, equation (1.1), and the electrostatic repulsion. The latter has the screened Coulombic or Yukawa form as follows

$$V(r) = \begin{cases} \infty & r < 2a \\ \frac{q_e^2}{\epsilon r} exp(-\kappa r) & r > 2a \end{cases} \tag{1.2}$$

where a is the particle radius, ϵ is the dielectric constant of the liquid and

$$q_e^2 = \frac{q_0}{1+\kappa a} exp(\kappa a) \tag{1.3}$$

is the effective charge of the particle which is related to the bare charge q_0.

$$\kappa = (\frac{4\pi}{\epsilon k_B T} \sum_j \rho_j q_j^2)^{1/2} \tag{1.4}$$

is an Debye screening parameter, ρ_j and q_j , the ion's number density and charge, respectively. This stabilization method has a long history and can be quite complicated to understand in great detail.

Hard Sphere System and Potential

On the other hand, the steric stabilized system is much simpler. For these systems, the particles are coated with relatively thin surface layers of macromolecular material which looks like a layer of hair on the surface of a sphere [2]. If the particles move close enough to each other to let the hairs overlap, the hairs will repel one another due to entropic effects. When the length of the hair is much less than the size of the particles, the interaction of the particles for this repulsion can be approximated by the simple pairwise hard sphere potential, which is similar to the atomic system at high temperature, with potential given as:

$$V(r) = \begin{cases} \infty & r \leq 2a \\ 0 & r > 2a. \end{cases} \tag{1.5}$$

The hard sphere system has simple thermodynamic properties which are independent of the temperature due to the fact that there is no interaction energy when the particles separate. The phase diagram and the structure of the system depend on only one parameter, ϕ, the volume fraction of the system.

Importance of Colloids in Fundamental Physics and Chemistry

Since the work of Brown[5] in the early nineteenth century, colloidal systems have produced many important contributions to physics and chemistry. Research on the Brownian movement of the colloidal particles provided a new way

to support the concept of the molecules and the kinetic theory of molecular movement.

In 1905, 1906, Einstein [6,7] gave a theory of the Brownian movement based on the theory of molecular movement. From the theory, the mean squared displacement L was given as

$$L = (\frac{tRT}{N3\eta\pi a})^{1/2}, \tag{1.6}$$

where t is the time the particle moves in the path A, η is the viscosity of the medium, a is the radius of the particle, R is the gas constant and N is the number of molecules in a gram-mol (Avogadro's number).

Avogadro's number, N, can be measured experimentally from equation (1.6). Perrin[8] investigated the almost monodisperse suspensions of gamboge and obtained a value for N between 5.6×10^{23} and 9.4×10^{23}. Later, Shaxby[9] obtained $N = 6.08 \times 10^{23}$ by measuring the movement of bacteria. The agreement of the measured value of N from the colloid experiments helped convince people of the concept of the existence of molecules which was not widely accepted at that time.

Colloids and Phase Transitions

Phase transitions are an old and important subject in physics. A theory to fully understand this topic is still missing. One of the phase transitions is the liquid-to-solid transition. Ice formation from water is the best known one in nature. Crystallization in a colloidal system[13] is another example of this kind of transition. One of the many applications of colloidal systems is as the model for this study of the phase transition.

As early as in 1930's, people found that colloidal systems can exhibit an order/disorder phase transition[10]. In late 1950's, three-dimensional crystals were observed in suspensions of tipula iridescent virus, and a light scattering technique was used to study the structures of the crystals[11]. The availability of several synthetic colloidal particle systems with narrow size distribution since late 1940's[12]

gave people the systems used to study the physics of colloidal phase transitions. Since then, the ability of colloidal systems to have phase transition and the properties (large structural relaxation times and weakness of the colloidal crystals) of the colloidal crystals have attracted more and more people to the solidification dynamics of colloidal crystals. Many experiments have been done on the colloidal phase transition.

First the equilibrium phase behavior of the colloidal systems was studied. The crystal structures were measured using a static light scattering technique which measured the light scattering intensity to obtained the structure factor as in X-ray diffraction studies. For hard sphere systems, samples were prepared in a series of volume fractions. Sedimentation measurement is employed to determined the phase diagram. Fluid, coexistence of fluid and crystal, homogeneous crystal, heterogeneous crystal and glass phases were observed as the sample volume fractions increased[13,14]. Freezing and melting points were determined to be at volume fractions of $\phi_f = 0.494$ and $\phi_m = 0.545$, respectively[15]. For the structure of the crystals, a random-stacked close-packed structure was observed[16]. For charged particles, the pairwise potential is a function of suspension condition which is related to the parameters such as electrolyte concentration, particle volume fraction, particle surface charges, etc. Phase behavior may be studied by changing any one of the parameters. Charged sphere systems evidence the same phase transition as hard sphere systems but with lower volume fractions depending on the other parameters, surface charges and electrolyte concentration, due to their long range of interaction[17–19]. The crystal structures were found to be body-centered cubic (BCC) at low concentration and face-centered cubic (FCC) at higher volume fraction [20–22].

For the kinetics of crystallization, several methods were used to do the study. The first is direct observation with a camera and image processing. The second is Bragg angle scattering which monitors the crystal structure of the crystals as the function of time. The third is small angle light scattering which measures

the density fluctuation of the sample. The last one is turbidity which monitors the total scattering by the sample. Details will be given in the next chapter.

Comparison of Atomic and Colloidal System

In pure atomic systems, the dynamics of the liquid to solid phase transition at supercooling is hard to control and measure due to the very fast kinetics of the transition. A computer simulation result showed that the nucleation rate in atomic system is about 10^{-10} second[23], which is presently too fast to measure. As a result, high resolution experimental data are sparse. The process of colloidal crystallization, on the contrary, is several orders of magnitude slower so that it is more easily measured. In addition, colloidal crystals have advantageous properties for phase transition studies. First is the capacity of colloidal crystals to diffract visible light. Bragg reflections are possible once the largest interplanar distance is greater than $\lambda/2$, where λ is light wavelength in the suspension. In the case of the colloidal samples, the spacing of the particles is on the order of the visible light wavelength, therefore, we see colorful crystals. It gives us the opportunities to study the phase transition with light scattering techniques. Second is the very low elasticity of the colloidal crystals due to the large interplanar distance. The colloidal crystal can be shear melted to a metastable fluid state, which is important since temperature is not an control parameter in hard sphere systems. Last, the size of the colloidal crystals is large enough in many cases that it is possible to observe directly single crystal growth. The difference of physical properties between colloid and molecular crystals is due to the difference in their respective microscopic length scales.

Both atomic and colloidal systems are classical statistical mechanics systems. They have the similar pair potential. For equilibrium properties, a colloidal system has phase diagram and crystal structure similar to pure atomic system. In this sense, a dispersion of colloidal spheres can be regarded as assembly of super-atoms. However, the dynamics of two systems is different. The atoms in the pure atomic system follow Newton's equations of motion. But due to the solvent, the

particles of the colloidal system execute Brownian motion and experience solvent mediated hydrodynamic interactions.

Hard Sphere System as Model Systems

Hard sphere systems play an important role as model systems in physics due to the simple pairwise interparticle potential. They are the simplest systems to show disorder to order transition. The question whether crystallization can occur in the hard sphere systems where there is no attraction was hotly debated among the physicists historically. As early as 1939 Kirkwood[24] speculated on the possibility of crystallization of hard sphere systems. The computer simulation work of Alder and Wainwright in 1957 [25] first indicated the hard sphere phase transition. The results showed that the equation of state of a hard sphere system has two density branches: a low density branch corresponding to fluid state and high density branch corresponding to crystalline order. A finally convincing proof of the hard sphere phase transition was given by Hoover and Ree[15]. Their numerical simulations established that the volume fraction of the coexisting fluid and solid phases are $\phi_f = 0.494$ and $\phi_m = 0.545$, respectively. When $\phi < 0.494$, the system is in a fluid state, for $0.494 < \phi < 0.545$, the system is in coexistence of liquid and solid, and for $\phi > 0.545$ up to close packing ($\phi = 0.74$), the system is in the state of long range order.

The "driving force" of the hard sphere phase transition is the system entropy which has two forms. The freezing of hard spheres is the result of the competition between these two forms of entropy: (1) a loss of global entropy due to the ordered structure which has fewer configurations than the disordered structure and (2) a gain of local entropy resulting from the decreasing of excluded volume caused by the localization of the particles in the order structure. In theory, with the application of density functional techniques [26,27], one can predict the hard sphere phase transition that agrees with the computer simulation result of Hoover and Ree[15]. In experiment, Pusey and Van Megen[13] first obtained the phase

diagram of hard spheres using a sterically stabilized PMMA particle system. There is a good agreement of their experiment results with the computer simulations.

No hard sphere atomic systems exists in reality. But at very high temperature, the strong Born repulsion dominates the interaction between two neighbouring particles. As an approximation, the hard sphere interaction is used for atomic systems. For sterically stabilized colloidal particles, when the steric surface layer is thin enough compared to the size of the particle, it is a good approximation to describe the system with the hard sphere potential equation (1.5). The hard sphere system is the simplest system to show the freeing/melting transition. Therefore, it is an important model in physics where theories and computer simulation results can be compared with the experiment data.

Summary

This thesis is organized as follows. Chapter II briefly reviews the studies of dynamics of colloidal system melting/freezing transition with various techniques. The original research is presented in the next three chapters. Nucleation and growth of crystals were measured with the small angle light scattering technique for a smaller size particle system than previously studied. The method, the results and the comparison of the results with a classical theory [28] are presented in chapter III. A range of power growth law exponents in the early time region and punctuated structure factors are observed. * A special photographic technique is proposed and morphology of the colloidal crystals is presented in chapter IV.† Sizes of the crystals were obtained from the slides. Crystal growth data measured in real space are consistent with the small angle light scattering data. A substructure in the crystals was observed, measured and compared to the Mullins-Sekerka instability

*Chapter III will be published (accepted by Phys. Rev. E) by authors: Yueming He, B. J. Ackerson, W. van Megen, S. M. Underwood and Klaus Schätzel.

†Chapter IV will be published (Langmuir (in review)) by authors: Yueming He, B. Olivier and B. J. Ackerson.

length. In chapter V,[‡] turbidity of the system is studied during crystallization. The turbidity measurement is more sensitive for the light intensity than other scattering techniques thus gives us the early time information about the samples. A laser heating effect on the solvent was observed in the early time range compared to that of SALS. It gave us the early time limit for the measurement of crystallization dynamics. In the last chapter, a conclusion is given. A brief review of the classical theory of a hard sphere colloidal crystal nucleation and growth is presented in Appendix A.

[‡]Chapter V will be published (accepted by Physica) by authors: Yueming He and B. J. Ackerson.

BIBLIOGRAPHY

1. A. P. Philipse and A. Vrij, J. Colloid Interface Sci. **128**, 121, (1989).
2. L. Antl, J. W. Goodwin, R. D. Hill, R. H. Ottewill, S. M. Owens, S. Papworth and J. W. Waters, Colloids and Surfaces **17**, 67, (1986).
3. B. V. Derjaguin, L. D. Landau, Acta Physicochim. USSR **14** , 633, (1941).
4. E. J. W. Verwey and J. T. G. Overbeek, *Theory of the Stability of Lyophobic Colloids* (Elsevier, Amsterdam 1948).
5. R.Brown, Phil. Mag. **4**, 161, (1882). Ann. Phys. **14**, 294, (1828).
6. A. Einstein, Ann. Physik, **17**, 549, (1905).
7. A. Einstein, Ann. Physik, **19**, 289, (1906).
8. J. Perrin, Ann. Chim. et Phys. **18**, 5, (1909).
9. J. W. McBain, *Colloid Science* (Heath & Co, Boston 1950), pp. 112-120.
10. I. Langmuir, J. Chem. Phys. **6**, 873, (1938).
11. K. M. Smith and R. C. Williams, Endeavour, **17**, 12, (1958).
12. W. D. Harkins, J. Am. Chem. Soc. **69**, 1428, (1947).
13. P. N. Pusey and W. van Megen, Nature, **320**, 340, (1986).
14. P. N. Pusey and W. van Megen, in *Physics of Complex and Supermolecular Fluids*, Eds. S. A. Safran and N. A. Clark (Wiley, New York,1978).
15. W. G. Hoover and F.H.Ree, J. Chem. Phys. **49**, 3609, (1968).
16. P. N. Pusey, W. van Megen, P. Bartlett, B. J. Ackerson, J. G. Rarity, and S. M. Underwood, Phys. Rev. Lett. **63**, 2153, (1989).
17. M. O. Robbins, K. Kremer and G. S. Grest, J. Chem. Phys. **88**, 3286, (1988).
18. L. P. Voegtli and C. F. Zukokski, J. Coll. Interface Sci. **141** 79, (1991).
19. J. K. G. Dhont, C. Smits, and H. N. W. Lekkerkerker, J. Coll. Interface Sci. **152**, 386, (1992).
20. K. Tokano and S. Hachisu, J. Coll. Interface Sci. **66**, 130 (1978).

21. R. Williams and R. S. Crandall, Phys. Lett. **48A**, 225 (1974).

22. Y. Monovoukas and A. P. Gast, J. Coll. Interface Sci. **128**, 533, (1989).

23. J. Q. Broughton, G. H. Gilmer, abd K. A. Jackson, Phys. Rev. Lett. **49**, 14960, (1982).

24. J. G. Kirkwood, J. Chem. Phys. **7**, 919, (1939).

25. B. J. Alder and T. E. Wainwright, J. Chem. Phys. **27**, 1208, (1941).

26. D. Oxtoby, Nature **347**, 725, (1990).

27. J. F. Lutsko and M. Baus, Phys. Rev. A **41**, 6647, (1990).

28. B. J. Ackerson and K. Schätzel, Phys. Rev. E **52**, 6448, (1995).

CHAPTER II

REVIEWS OF PREVIOUS WORK IN COLLOIDAL CRYSTALLIZATION

Bragg angle scattering

In colloidal crystals there is a periodic arrangements of the colloidal particles as in atomic crystals. If incident light is scattered by this structure, maxima of the scattering intensity appear at the Bragg angle directions. Dynamic crystallization information is obtained by monitoring the time evolution of the Bragg diffraction [1,2]. Dhont et al.[1] used charged TPM-silica and Harland et al.[2] used steric stabilized PMMA hard spheres in dynamic Bragg scattering experiments.

A typical experimental setup is shown in figure 2.1 The sample is held in a cylindrical cuvette which can be rotated in the center C. The key element of the setup is a high resolution diode array camera (DAC). The DAC used in reference [1] has a pixel size of $25\mu m$ or a scattering angular resolution of $0.007°$ and a time resolution of 10 ms. Scattered Bragg peak intensity, $I(q,t)$, where q is the scattering vector, is collected by the camera at certain time intervals for an extended period of time. Maximum intensity, position and width of the Bragg peak as a function of time were obtained and were used to study the dynamics of crystallization. Usually, the sample is rotated slowly ($0.01 \sim 0.06$ Hz) during the experiment to get better statistical data for the crystallization kinetics (averaging over the size, orientation and number of the crystals in the scattering volume of the sample) because only a few crystals present in the scattering volume are oriented to scatter light to the DAC at any time.

X-ray diffraction theory[3] was adapted to analyze the data and calculate the quantities relevant to nucleation and growth in colloidal systems. In reference [1], assuming uniform crystal sizes, crystal cubes of $(N \times N \times N)$ FCC unit cells,

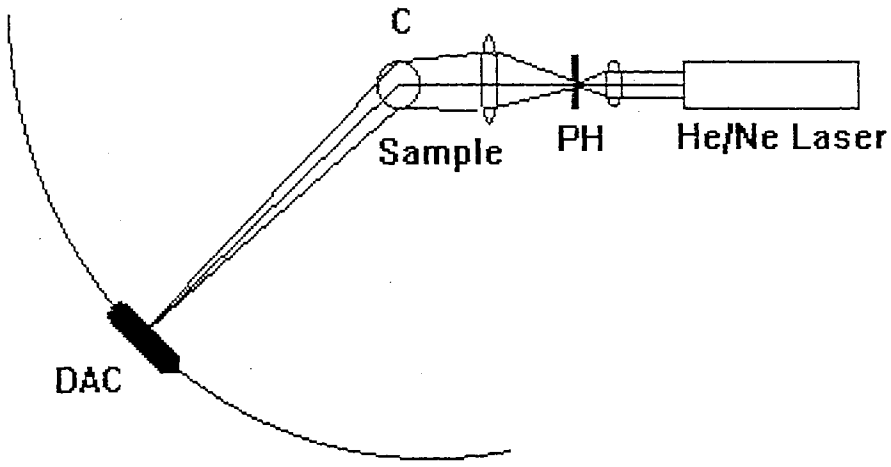

Figure 2.1. Optical setup used for Bragg scattering measurement.

a constant rate of nucleation, interface limited growth, and a constant growth velocity, the authors obtained various quantities: the induction time, the nucleation rate, the crystal growth rate, the size of crystallites and the number of crystallites in the scattering volume as the function of sample concentration.

In reference [2], Harland et al. measured the growth of the lowest order Bragg reflection intensity profile, $I(q,t)$. The structure factor, $S_c(q,t)$, of the crystals were obtained by dividing $I(q,t)$ by the single particle form factor , then subtracting the structure factor of the hard sphere fluid at the same volume fraction. The integral of $S_c(q,t)$ with respect to q under the main Bragg peak gives the extent of crystallization $X(t)$. The average linear size of the crystals, $L(t)$, is obtained from the width of the peak at half maximum, $w_q(t)$. Therefore, the number density of the crystals is $N_c(t) = X(t)/L^3(t)$. A accelerated nucleation rate, $N_c(t) \sim t^3$, was observed. The Maximum nucleation rate density, $c = dN_c/dt$, is consistent with the nucleation rate density (assumed constant) predicted by the classical theory[4–6]. The authors had trouble obtaining the data for low concentration samples $0.49 < \phi < 0.53$. They said that the data of low concentration samples ($\phi < \phi_m$) suffer from considerable statistical uncertainties due to poor orientational averaging over the relatively small number of crystals in the illuminated region. Thus the Bragg angle scattering method loses sensitivity for the lower concentration samples.

Transmitted light intensity measurement (turbidity)

Turbidity measures the transmitted light intensity of a sample as the function of time. It is used widely in the colloidal related industries to measure particle size and size distributions[7–9] and in physics to measure critical point behavior[10,11], particle interactions[12], and dynamics of the colloidal crystallization [13]. Aastuen et al.[13] monitored the transmitted light intensity and proposed a model based on the Avrami's theory[14,15] of crystallization. They obtained the nucleation rate density, c, by fitting the transparency data (as the function of time) to their model.

In the model, the effect of the light scattering due to the system density fluctuations is neglected assuming the light scattering is strictly a volume effect. If the effect of wall growth is excluded, the transmitted light intensity, I_t, would be

$$I_t = I_0 exp(-\alpha_b d_b - \alpha_l d_l) \tag{2.1}$$

where α_b, α_l are absorption coefficients and d_b, d_l are lengths for bulk crystals and liquid respectively. α_b and α_l will be considered as constant parameters for a particular concentration sample. d_b and d_l are obtained by a statistical method in which the most probable length is calculated as follows:

$$d_l = \int_0^{d/2} 2m(t)dx, \tag{2.2}$$

and $d_b = d - d_l$, where d is the total length of the sample (cell length), $m(t) = \exp(-(\frac{c\pi}{3})v^3t^4)$ is the probability that a point is liquid after time t in the condition of interface limited growth with constant growth rate v. These results, substituted into equation (2.2), yield the result:

$$I_t = I_0 exp[8(\alpha_b - \alpha_l)d \exp(-\frac{c\pi}{3}v^3t^4)] \exp(-\alpha_b d). \tag{2.3}$$

The nucleation rate density c is obtained by a nonlinear least-square fit of the form of equation (2.3) for transmitted light intensity, I_t, with three parameters (α_b, α_l, and c) to measured transmitted intensities. The constant growth rate, v, in equation (2.3) was obtained by measuring the crystal growth in real space.

Crystal direct observation and morphology

The colloidal crystals are large enough to observe growth with weak magnification. The interparticle spacing in colloidal crystals is on the order of wavelength of visible light so that a colorful picture of the crystals is observed when they scatter incident white light. Monovoukas et al.[16] studied charged sphere crystal growth in thin cells with a optical polarizing microscope in transmission. Structure and orientation information of crystals is obtained with the sample between two crossed polarizers. Fcc crystals orient with their (110) planes parallel to the cell

wall. Dynamical diffraction theory[17] is employed to explain the experimental data.

Aastuen et al.[13,18] observed the charged sphere crystal growth using camera with microscope and video equipment. Figure 2.2 show the experimental setup used by the authors. Nucleation and growth of single BCC crystallites was observed when the samples were sheared melted to the metastable state. They found that crystals are nearly spherical and their surfaces are rough. Interface limited growth was observed for all samples (densities between $1\mu m^{-3}$ and $3\mu m^{-3}$). The growth rates are a function of particle concentrations, and are fit to the Wilson[19] and Frenkel[20] growth law. The growth rate is determined by self diffusion.

Recently, Würth et. al.[21] directly observed the BCC colloidal crystal growth in the (110) direction with video microscopy and image processing technique for systems of highly charged spheres and precision control of ionic strength. Their measured data are consistent with the data of Aastuen et al. They observed that the growth velocities are constants with the time for all the samples with different fixed volume fractions and salt concentrations; and the growth velocities as the functions of volume fraction and salt concentrations can be unified to a master function and fitted with the Wilson-Frenkel growth law, if the velocities were plotted versus the reduced density difference. The microstructure of the interface was discussed with a model in which there are several particle layers that continuously decay from crystalline into liquid within a finite thickness of the interface.

Small angle light scattering

During the order/disorder transition of colloidal samples, the density fluctuates. Schätzel and Ackerson[22,23] used a time resolved small angle light scattering technique to monitor the density fluctuations and obtain crystallization information. Sterically stabilized PMMA hard spheres ($r = 500nm$) were used in the studies. In their scattering setup, a microscope objective and a pin hole were used to spatially filter and expand a laser beam. The beam was scattered by the sample and the scattered light was stopped by a screen which is about $1m$ away

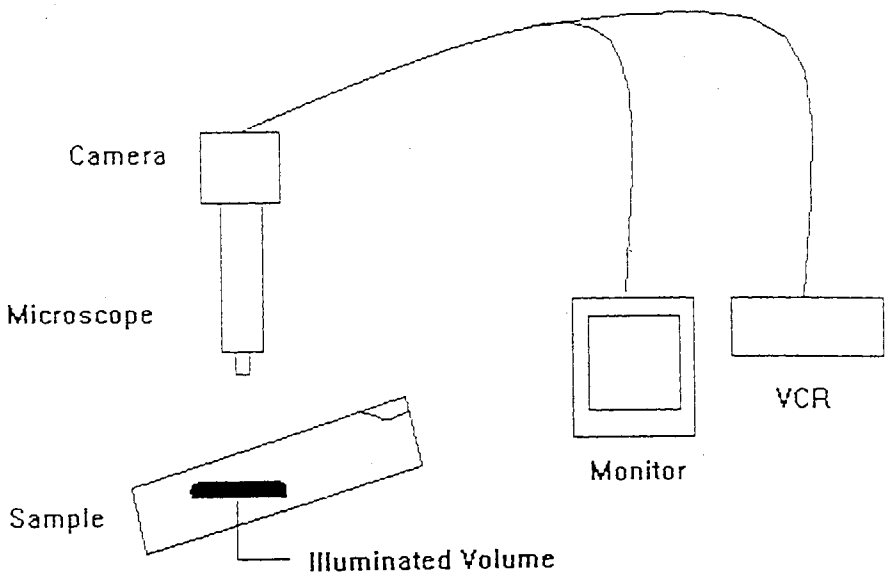

Figure 2.2. Experimental setup to observe the crystal growth directly.

from the sample. Analogous with phase seperation in binary liquid mixtures, the scattered intensity appears like a bright "ring" (peak intensity at finite scattering vector). The shape and intensity change with time, as the phase transition proceeds. A series of small angle scattering images was recorded with a CDD camera controlled by a PC. The images were processed to extract the data of the peak intensity, positions and the contributions of the rings as the functions of the time. From the data, what were found by the authors are as follows: Two time regions of the order/disorder transition of the hard sphere system were observed. In small time region, power-law growth in peak intensity was found. For samples near melting concentration, diffusion limited growth was observed instead of interface limited growth[18] for charged sphere system. In large time region, ripening growth was observed. Crystals grow with $t^{1/3}$ for samples with densities lower than the melting point and with $t^{1/2}$ or faster for higher density samples. The data for low concentration samples show that the length scale determined by the peak position first increases but then decreases in the "crossover" time region and grows again in large time region. The structure factor (intensity contributions of the rings) can be scaled to a common master function for samples near melting point. There are a deviations to the common master function for samples with lower or higher concentrations.

As mentioned in references[21,23], the difference of the crystal growth velocity between hard sphere and charged sphere is due to their pairwise interactions. Systems with long range interaction begin to crystallize at small volume fraction and the density difference between crystal and liquid is small compared to the hard sphere system which has a crystal density about 10% above that of the liquid at coexistence. Therefore, in charged stabilized systems the crystal can grow without diffusion limitation by the large distance particles, and the growth rate is constant with the time. On the other hand, the large change in volume fraction for hard sphere depletes the liquid phase near the crystal. This leads to a highly complex and nonlinear growth with the time.

BIBLIOGRAPHY

1. Jan K. J. Dhont, C. Smath, and Henk N. W. Lekkerkerker, J. Colloid Interface Sci. **152**, 386, (1991).

2. J. L. Harland, S. I. Henderson, S. M. Underwood and W. van Megen, Phys. Rev. Lett. **75**, 3572, (1995).

3. R. W. James, *The Principles of the Diffraction of X-Ray*, Edited by L. Bragg (Cornell Univ. Press, N. Y., 1965).

4. W. B. Russel, Phase Transitions **21**, 127 (1990).

5. J. S. van Duijneveldt and H. N. W. Lekkerkerker, in *Science and Technology of Crystal Growth*, edited by J. P. Erde and O. S. L. Bruinsma (Kluwer Academic, Dordrecht, 1995).

6. B. J. Ackerson and K. Schätzel, Phys. Rev. E **52**, 6448, (1995).

7. H. G. Brath anf S. T. Sun, Anal. Chem. **65**, 55R, (1993).

8. T. Kourti and J. F. MacGregor, ACS Symp. Ser, No. 427, 34, (1991).

9. E. Dickinson, Food Chem. **51**, 343, (1994).

10. P. Calmettes, I. Lauguës, and C. Laj, Phys. Rev. Lett. **28**, 478, (1972).

11. T. Narayanan and K. S. Pitzer, International J. Thermophys., **15**, 1037, (1994).

12. U. Apful, R. Grunder, and M. Ballauff, Colloid Polym. Sci. **272**, 820, (1994).

13. D. J. W. Aastuen, N. A. Clark, J. C. Swindal, and C. D. Muzny, Phase Transitions **21**, 139 (1990).

14. M. Avrami, J. Chem. Phys. **9**, 177, (1941).

15. G. S. Zhdanov, *Crystal Physics*, translated and edited by A. F. Brown (Academic Press, New York, 1965).

16. Y. Monovoukas and A. P. Gast, Langmuir **7**, 460, (1991).

17. W. H. Zachariasen, *Theory of X-Ray Diffration in Crystals*, Wiley, New York, (1945).

18. D. J. W. Aastuen, N. A. Clark, L. K. Cotter, and B. J. Ackerson, Phys. Rev. Lett. **57**, 1733 (1986); **57**, 2772 (1986).

19. H. A. Wilson, Philos. Mag. **50**, 238, (1900).

20. J. Frenkel, Phys. Z. Sowjetunion **1**, 498, (1932).

21. M. Würth, J. Schwarz, F. Culis, P. Leiderer, and T. Palberg, Phys. Rev. E **52**, 6415, (1995).

22. K. Schätzel and B. J. Ackerson, Phys. Rev. Lett. **68**, 337, (1992).

23. K. Schätzel and B. J. Ackerson, Phys. Rev. E **48**, 3766, (1993).

CHAPTER III

CRYSTALLIZATION DYNAMICS IN HARD SPHERE SUSPENSIONS

Abstract

Density fluctuations are monitored by small angle light scattering during the crystallization of 0.22μm radius, hard colloidal spheres. Measured structure factors show an intensity maximum at finite scattering vectors. The shape of the intensity distribution scales at early times during nucleation and growth and again at large times during ripening. At intermediate times there is a crossover region where scaling ceases to be valid. Both the amplitude and the position of the maximum intensity show quasi-power law behavior in time. The values of the observed exponents are within the range expected for classical growth models. The breadth of the intensity distribution increases with increasing volume fraction, suggesting greater crystal polydispersity with increasing volume fraction. The lower volume fraction intensity distributions suggest crystals have a compound or internal structure, while the observed decrease in characteristic length in the crossover time regime may indicate breakup of crystals to this smaller internal structure. The results of measurements are compared with results calculated for nucleation and growth of crystals in suspensions of hard spheres. Results also are compared with earlier measurements made on samples containing 0.50μm radius spheres. Differences in the two systems are discussed in terms of interparticle potential, polydispersity and gravitational effects.*

*will be published (accepted by Phys. Rev. E) by: Yueming He and Bruce J. Ackerson; Department of Physics and Center for Laser Research; Oklahoma State University ; Stillwater, OK 74078-0444;

W. van Megen and S. M. Underwood; Department of Applied Physics; Royal Melbourne Institute of Technology; Melbourne, Victoria, Australia;
Klaus Schätzel; Institut für Physik; Johannes Gutenberg Universität; D-55099 Mainz, Germany

Introduction

The dynamics of crystallization, the disorder to order transition from a metastable fluid to a crystalline solid, is very rapid and hard to characterize in simple atomic systems. Only recently have advances in instrumentation permitted kinetic studies of crystallization in metallic glasses by using x-ray diffraction with millisecond time resolution[1]. In complex fluids crystallization dynamics is orders of magnitude slower and the lattice constants are on the order of the wavelength of light. Thus time resolved optical analogues of x-ray diffraction[2–6] and microscopy[7] have proved useful in characterizing homogeneous nucleation and growth in these systems.

In colloidal systems the suspended particles order into crystalline lattices from initially shear melted[8] amorphous metastable fluid state. These samples differ from pure atomic systems in that the sample volume is fixed by the suspending fluid, and crystallization occurs at fixed volume rather than fixed pressure. Furthermore, the particles exchange energy and momentum with the solvent. Any latent heat produced is rapidly dissipated by the solvent with negligible change in temperature. Finally, the colloidal particle interactions are essentially repulsive due to charge stabilization or steric stabilization to prevent particle aggregation. Despite these differences between atomic and colloidal systems, we expect the essential features of the phase transition is similar in atomic and complex fluid systems.

Most homogeneous colloidal crystallization work has focussed the crystal order parameter, a nonconserved parameter used to characterize the disorder to order phase transition. Aastuen et al. [2] have made direct observations of growing crystallites in aqueous suspensions of charge stabilized polystyrene spheres as a function of particle volume fraction. The size of the crystals was found to be directly proportional to the elapsed time, indicating interface limited growth. The velocity increased and saturated with increased sample volume fraction and was characterized by the classical Wilson-Frenkel growth law. Dhont et al.[4] used time

resolved light scattering to monitor the first order Bragg peak during crystallization in suspensions of slightly charged silica particles. Interface limited growth was assumed implicitly and a classical analysis made to determine induction times, nucleation and growth rates, and the size and numbers of the crystals as a function of particle volume fraction. The nucleation rate density was found to have a much weaker dependence on volume fraction than predicted[9].

Recently a conserved parameter, the particle density, has been monitored during the crystallization process[5,6,10]. Small angle light scattering measurements were made during the crystallization process in suspensions of sterically stabilized spheres in a solvent which has nearly the same index of refraction as the particles. The observed scattered intensity distribution had a maximum at finite scattered wave vector and was observed to scale over nearly the full observation time. As a result, the experimental data was represented by the position and magnitude of the intensity maximum as a function of time. Two distinct time regimes were observed and termed "nucleation and growth" and "ripening". In the nucleation and growth region the intensity maxima were observed to follow a power law increase in time with an exponent of four for volume fractions equal to or less than the melting value. Similarly the position of the maximum moved towards zero scattering angle with increasing time, following an inverse square root time dependence near melting volume fractions. Thus a characteristic length was increasing as the square root of time and was consistent with diffusion limited rather than interface limited growth. The intensity growth exponent was explained in terms of a constant nucleation rate and the diffusion limited growth of crystals.

In the ripening region, the growth of the maximum intensity was much slower with an exponent of unity or less. The exponent for the position of the maximum was one third for volume fractions less than the melting value. This is consistent with the exponent for Ostwald ripening in a two phase region. For volume fractions greater than melting the exponent was observed to be one half, consistent with the exponent for growth through domain wall motion. Dynamical scaling was also examined and found to give the expected scaling exponent of three

for this three dimensional system for volume fractions equal to the melting value or less. For larger volume fractions, the exponent was observed to be two and is not yet understood.

In this work we present results of similar small angle light experiments for suspensions of smaller radii colloidal particles. A number of samples closely spaced in volume fraction were studied. The growth exponents for both the intensity and the characteristic length were larger than found at corresponding volume fractions for the previously studied $0.50\mu m$ radii particles. All samples, exhibited a decrease in scattered intensity and reduction in characteristic length in the crossover region between nucleation/growth and ripening. This combined with changes observed in the shape of the small angle intensity distribution suggest crystal breakup or dissolution in the crossover region before ripening commences. The intensity distribution shape functions became broader as the volume fraction of particles increases. This is attributed to a larger polydispersity of the scattering entities with increasing volume fraction.

In the following section the samples, experimental apparatus and procedure are discussed. This is followed by a presentation of the results. Finally we compare the data with theory for classical crystallization in suspensions of hard spheres and with measurements taken for suspensions with larger radii spheres. The differences are discussed in terms of interparticle potential, polydispersity and gravitational effects.

Experiment

Particles

The colloidal suspensions used in these experiments contained uniformly sized polymethylmethacrylate (PMMA) spheres coated with a thin ($\sim$ 10nm) layer of poly-12-hydroxystearic acid [11]. This coating provided sufficient steric stabilization to prevent flocculation. The particle radius was determined to be 220nm

with a polydispersity of 7% relative standard deviation by dynamic light scattering on diluted suspensions. The solvent was a mixture of tetralin (46wt%) and decalin (54wt%) in a ratio adjusted to closely match the index of refraction of the suspended particles. Exact matching was not possible due to difference in refractive index of the particle core and coating. Also the matching point is sensitive to temperature and probing wavelength. However, samples with particle volume fractions on the order of 50% appeared clear to the eye and showed a total scattering of less than 50% of the incident light for a path length of 10mm at a wavelength of 633nm. The losses were due primarily to small angle and Bragg scattering.

Samples having different particle concentrations were prepared by loading optical quality cuvettes (10mm×10mm×50mm) with an index matched stock sample of known weight of each solvent and particle component. The particles were then centrifuged to the bottom of each cuvette and different weights of the supernatant were withdrawn to obtain a series of samples having particle weight fractions ϕ_w ranging from 0.391 to 0.491. The particles were redispersed by vigorous agitation of the cuvettes, which were then left undisturbed for approximately two months. During this time crystallization commenced and the crystals being more dense than the amorphous phase settled. The phase diagram shown in figure 3.1 was determined using the sedimentation tracking method of Paulin and Ackerson.[12]. The volume fraction $\phi = (0.494/0.395)\phi_w$ has been rescaled from the weight fraction to make the freezing point coincide with the value for hard spheres, $\phi_f = 0.494$ [13]. It is seen that this rescaling brings the melting point $\phi_m = 0.55 \pm 0.01$ into close agreement with that for hard spheres (0.545 ± 0.02). The required rescaling was larger than that for PMMA particles having twice the radius[12] but was the same order as that required for similar sized particles (325nm in radius) suspended in mixtures of decalin and CS_2[14]. It is believed that absorption of tetralin or CS_2 into the particle coating (or core) may be responsible for this effect [14–16]. The weight of each cuvette was monitored to account for any change in particle volume fraction due to solvent evaporation over the duration of these experiments.

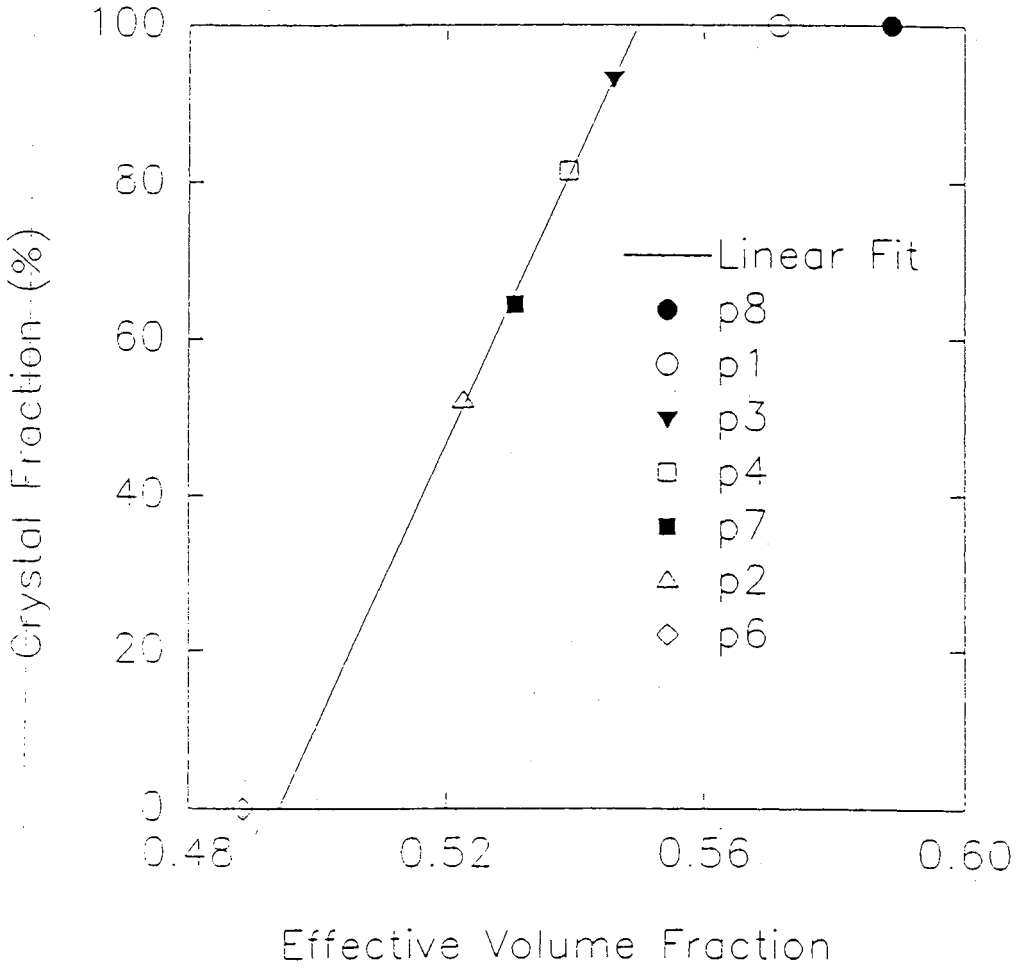

Figure 3.1. Phase diagram for the colloidal system used in the experiment. The freezing point is fixed at 0.494 as described in the text and a fit determines the melting point to be a volume fraction of 0.55.

Small angle light scattering setup

The small angle light scattering setup shown in figure 3.2 was modified slightly for some measurements from that reported previously[6]. A small HeNe laser beam (5 mW, polarized) was spatially filtered and expanded using a microscope objective (20×) and a pin hole (25 micron diameter) in a commercial mechanical (Newport) unit. A single "best form" lens ($f = 80$ mm, anti-reflection coated for 633 nm) refocused the filtered beam onto the detection screen. An aperture adjusted to coincide with the first diffraction minimum ($\sim$ 9mm) produced by the pinhole was placed just before the sample. Careful aperture adjustment minimized diffraction both from the aperture and from scattering by sample cell walls. The detection screen was adjusted to lie between 0.68 to 1.25m from the sample. The distance chosen depended on the particular sample.

Scattered light was detected in either a transmission or reflection geometry. In the reflection geometry used previously[6], the focused primary beam passed through a 2 to 5mm hole in the center of the screen to a distant beam stop. The smaller hole sizes were needed for the relatively smaller scattering patterns produced by larger crystals of the lower volume fraction samples. Scattered light was detected by CCD-video camera placed slightly off-axis, typically just below the main beam and close to the sample. In the transmission geometry the primary beam was incident on a beam stop placed directly on the detection screen. The CCD-video camera was placed on axis with the beam a distance of 60 cm behind the detection screen.

Measurements in either geometry gave identical results, except that the magnitude of the scattered light is approximately sixfold larger in the transmission geometry. This larger intensity proved useful for the relatively weak scattering produced by the larger volume fraction samples. These two arrangements kept the geometric distortions negligible for the observed small angle scattering. The camera resolved 192 by 165 pixels and exposure times were kept close to 200 ms. The scale of the scattering wave vector $q = 4\pi n sin(\theta/2)/\lambda$ was calibrated by placing a grating with 200 lines/inch in the position of the sample and detecting

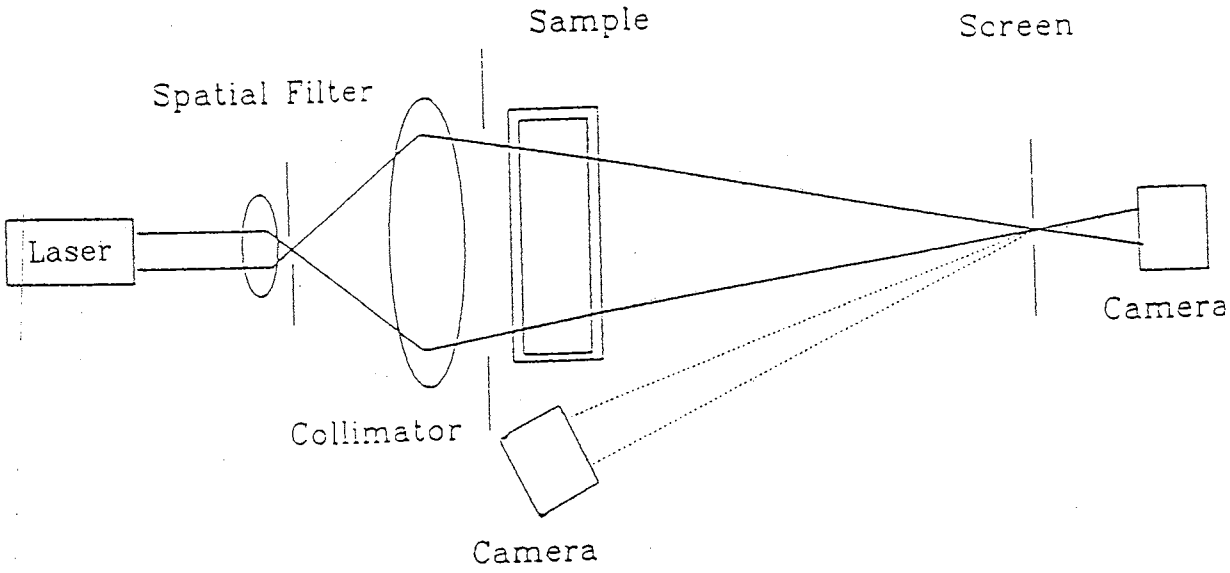

Figure 3.2: Optical setup used for small angle light scattering. The different camera positions correspond to transmission and reflection geometries. The transmission geometry setup has six times more sensitivity compared to the reflection geometry.

the positions of the diffracted maxima using two orthogonal orientations of the grating. Here the index of refraction of the solvent is given by n, the incident laser wavelength by λ, and the scattering angle by θ.

Data analysis

Data analysis followed the same procedure developed previously[6]. The CCD-video camera was driven by a personal computer which accepted the digitized image data having 8 bit resolution and stored the data on magnetic disks. Frame rates varied from one frame every 20 seconds (immediately after shear melting) to one every hour at large times. At the end of a data collection run, the processing involved careful centering of the series of scattering images followed by the calculation of radial intensity distributions $I(q)$.

To eliminate detector dark count, low angle static scattering produced by the sample cuvette, and a small amount of residual static scattering from the optical system, a radial intensity distribution from an early image was subtracted from each of the other intensity distributions. Typically the chosen image exhibited the smallest intensity values throughout the useful q-range. In most cases all early images were almost equivalent. However, index of refraction changes, associated with temperature equilibration or sample flow relaxation after shear melting, can produce scattering changes in this time range and must be avoided. The temperature of the samples was maintained to within $\pm 1^{\circ}C$. After compensating for differences in optical setup, apertures and exposure times, all intensities can be represented approximately on the same scale. Because the smaller particle samples studied here exhibit nucleation and growth on a faster time scale than the previously reported samples with larger radii particles, faster initial frame rates were required to obtain image data suitable for subtraction.

Background subtracted intensity distributions evidenced a ring structure with a maximum in the intensity at finite wave vector q_m. The value of the maximum and its position changed with time as shown in figure 3.3. The value of the maximum I_m was determined by fitting a second order polynomial to the data in

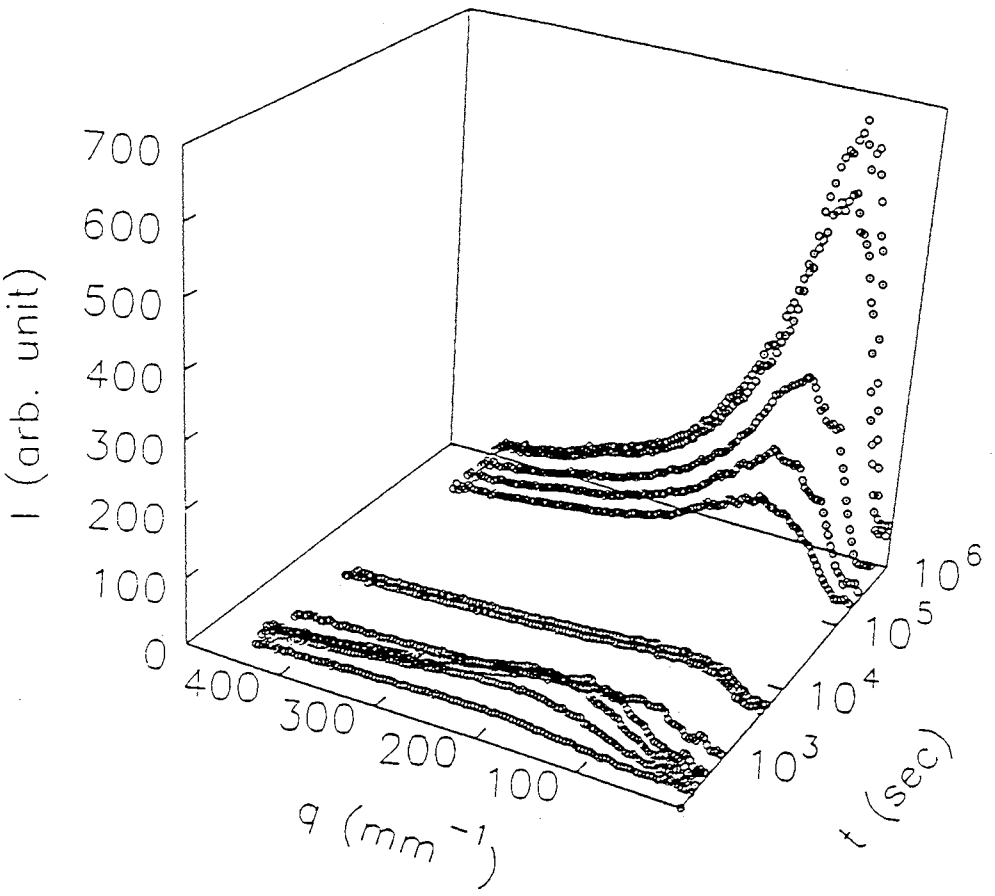

Figure 3.3. Measured light scattering intensity as a function of scattering vector and time for sample p3 ($\phi = 0.594$). Three distinct regions are observed: nucleation and growth ($t < 510$ sec), crossover ($510 < t < 192000$ sec) and ripening ($t > 192000$ sec).

a limited region around the peak. The ring position could be characterized most accurately by the larger wavevector $q_{1/2}$, where the intensity distribution fell to half its maximum value. I_m and $q_{1/2}$ were studied as functions of time and also used to obtain scaled structure factors as follows

$$S(Q,t) = I(q,t)/I(q_m,t), \quad Q = q/q_{1/2}(t). \tag{3.1}$$

Results

Time dependence

Figure 3.4 and figure 3.5 show, respectively, the parameters I_m and $q_{1/2}$ for the intensity maximum and location as a function of time elapsed since the cessation of shear melting. The double logarithmic scales demonstrate the large dynamic range of the data and any approximate power law growth behavior. For all samples the I_m show the same qualitative form. There is an inital rapid growth to a maximum value followed by a decrease to a lower value. When runs are made to sufficiently large elapsed times, I_m again evidences an increase in value. For purposes of discussion we will consider this behavior to consist of three parts as done in previous studies [6]: (1) an "initial nucleation and growth" region from zero time to the time where the maximum in scattered intensity I_m occurs, (2) a "crossover" region from the time of the first maximum to approximately the point where I_m begins the second increase in value, and (3) the "ripening" region where the large elapsed time increase in I_m occurs. Any breaks in these intensity data correspond with adjustments in the beam intensity to avoid saturating the CCD-video camera as the scattered intensity increases.

In the nucleation and growth region, I_m exhibits nearly power law growth in elapsed time with an exponent 4.66 ± 0.02 ($\phi = 0.531$) at one of the lowest volume fractions and increasing to a maximum value of 7.15 ± 0.16 ($\phi = 0.545$) before decreasing to 5.57 ± 0.23 ($\phi = 0.549$) for a sample near melting and further decreasing to 3.6 ± 0.1 ($\phi = 0.551$) for the fully crystallized sample. At the larger

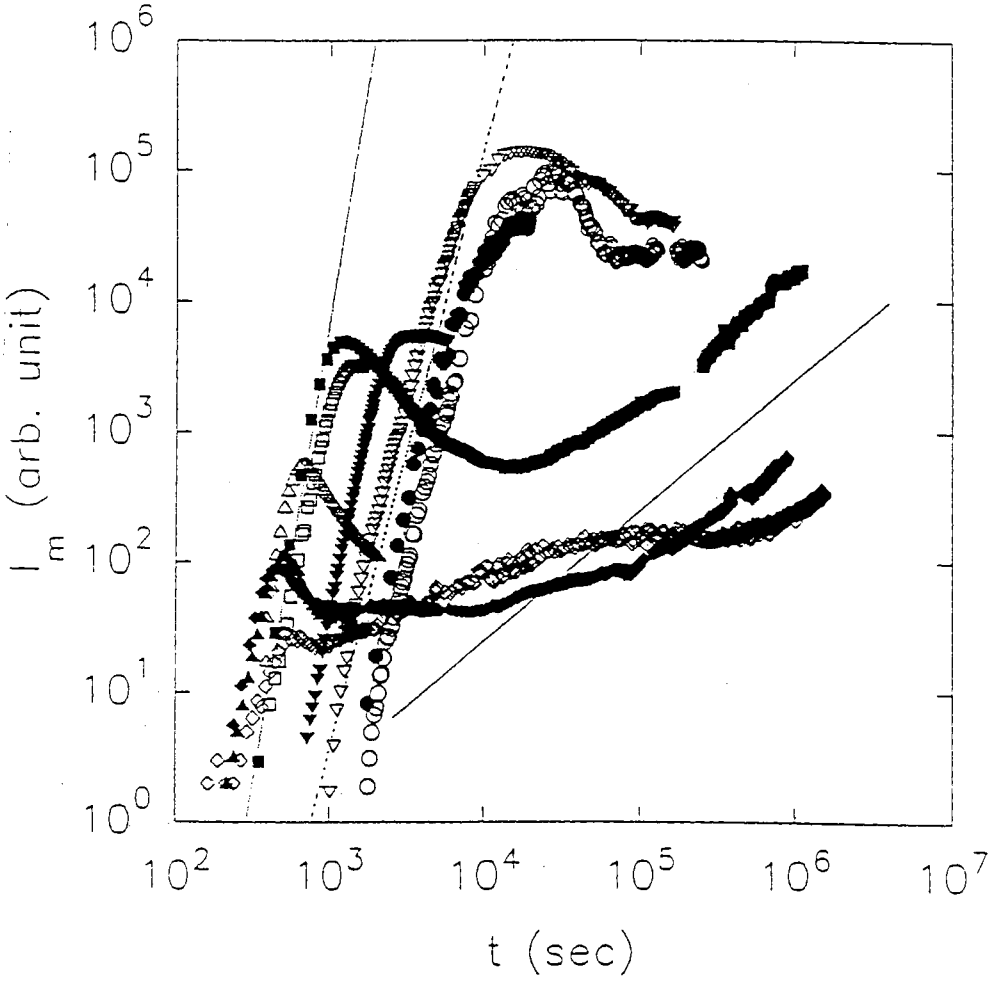

Figure 3.4. Peak intensity $I_m(t)$ as a function of time for different volume fraction samples. Power laws t^7 (dotted line), $t^{4.5}$ (dashed line) in early time region and t^1 (solid line) in late time region are indicated.

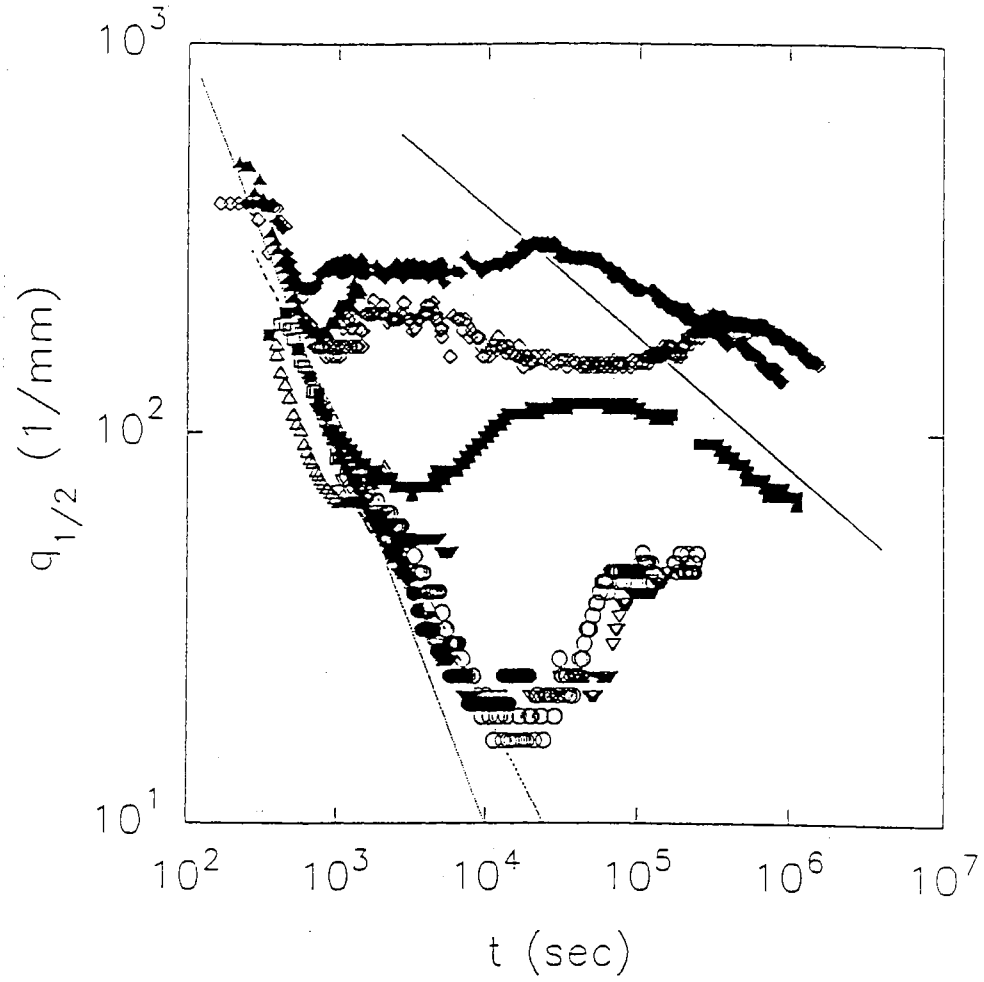

Figure 3.5. Characteristic scattering vector $q_{1/2}(t)$ as a function of time for different volume fraction samples. Power laws $t^{-0.75}$ for low concentration samples (dotted line), and t^{-1} for samples near the melting point (dash line) in early time region and $t^{-1/3}$ (solid line) in late time region are indicated.

volume fractions, I_m remains fairly constant for a large range of elapsed time (two days) in the crossover region, while at the lower volume fraction measured, I_m is not constant for a similar range of crossover time. In the ripening region the data at the largest measured elapsed times may be characterized by linear or sublinear power law behavior. The quoted error in the exponential values is determined from the best fit to the data.

In figure 3.5, $q_{1/2}$ is shown as a function of elapsed time, where it is seen that all volume fractions appear to have the same qualitative behavior. The characteristic wavevector initially decreases in magnitude indicating the growth of a characteristic length. However, this wavevector evidences a minimum and then increases with increasing elapsed time. This implies a decrease in the characteristic length in this elapsed time region. At sufficiently large elapsed times, the characteristic wavevector again decreases indicating a growth of the characteristic length. Like the I_m data, this data may be discussed in terms of three regions. The initial growth of a characteristic length scale corresponds to a nucleation and growth region. The time where the characteristic length scale decreases to the time where it again increases corresponds to a crossover region. A ripening region corresponds to the large elapsed times where the characteristic length scale increases. This identification is somewhat ambiguous since the I_m maximum and the $q_{1/2}$ minimum do not occur at exactly the same time, the minimum being later in time. With this descrepancy in mind we will use this terminology (nucleation/growth, crossover, and ripening) to discuss the time dependent data.

In the nucleation and growth region $q_{1/2}$ decreases with an approximate power law behavior ranging from 0.75 ± 0.02 ($\phi = 0.531$) at the smallest volume fraction measured to 1.01 ± 0.08 ($\phi = 0.549$) for the sample near the melting point. In the crossover region the characteristic length remains fairly constant as does the intensity for the larger volume fractions. For the lower volume fractions the characteristic length changes as does the intensity. For the largest elapsed times we compare the data with decreasing power law exponent of 1/3. While the data approximates this power law behavior, it is not clear if this is the ultimate

asymptotic behavior of the data. Measurements at even larger elapsed times would require better temperature control and laser stability.

Scaling

The normalized or scaled structure factor is shown in figures 3.6, 3.7 and 3.8 using the data in figure 3.3 for a sample near the melting point ($\phi = 0.549$) . From this data we conclude that the scattered intensity does not scale over the full time domain, because it cannot be completely characterized by I_m, $q_{1/2}$ and a single shape function. However, the scaling is punctuated. For limited time regions, scaling is observed to hold. These regions correspond to the initial nucleation and growth phase for times less than 600 seconds and to the ripening phase for times greater than 150 thousand seconds. Despite the great time lapse separating the two regions, the shape functions indicated by the solid lines in figures 3.6, 3.7 and 3.8 is very similar. The crossover region are much less settled where the shape function, being much broader, deviates markedly from that observed in the other two regions. Furthermore, it changes rapidly to this form which shows approximate scaling in the time range between 600 seconds and 6000 seconds but evolves slowly at larger elapsed times to the ripening form.

The shape functions also depend on the volume fraction as shown in figures 3.9, 3.10 and 3.11. A double logarithmic plot of $S(Q)$ is given as a function of Q and parametrized by volume fraction. The shape function for each volume fraction is shifted by an order of magnitude from the neighboring ones for clarity of presentation. As the volume fraction decreases, the scattered intensity maximum moves to smaller angles and cannot be resolved reliably with our apparatus for volume fractions less than 0.525. As the volume fraction increases the shape function broadens in all scaling time domains. To make more quantitative comparisons the data has been fit by the Furukawa form [17]:

$$S(Q,\phi) = \frac{(1+\gamma(\phi)/2)Q'^2}{\gamma(\phi)/2 + Q'^{2+\gamma(\phi)}} \tag{3.2}$$

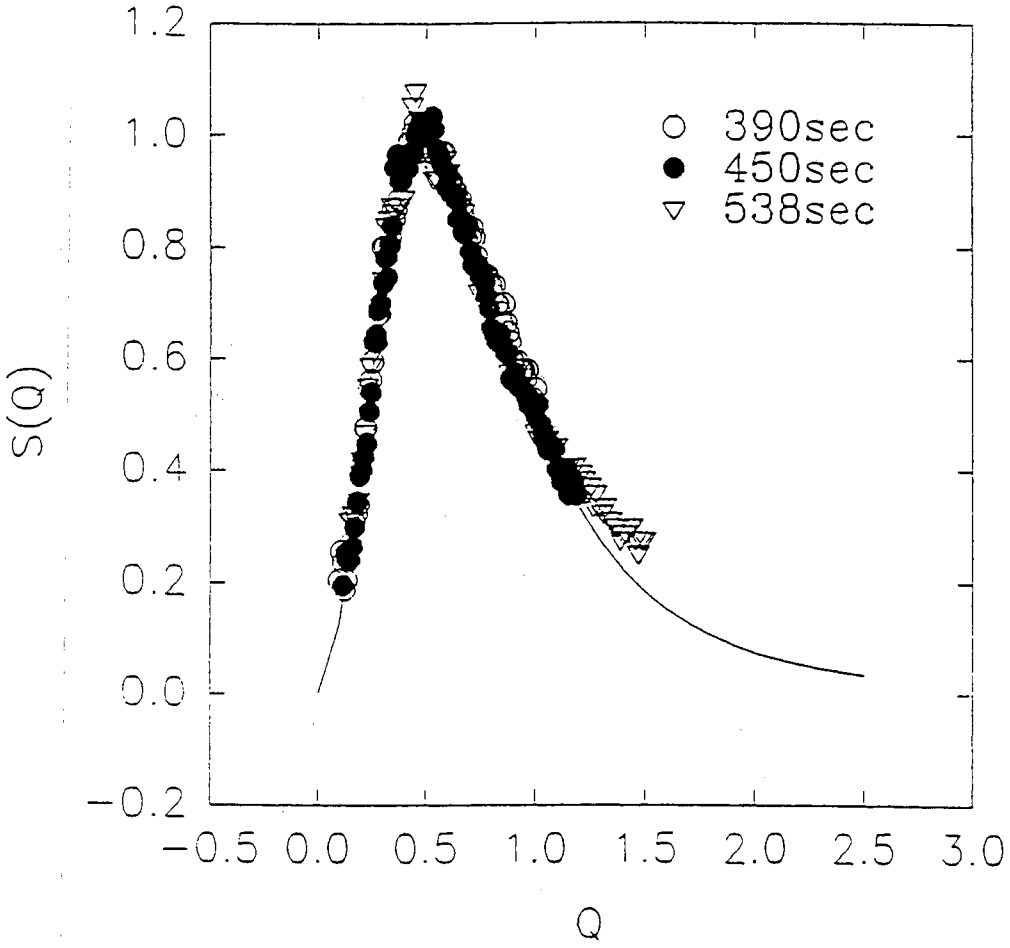

Figure 3.6. Structure factors for data in figure 3.3 in "nucleation and growth" time regions are shown and as well as F urukawa scaling function $F(Q)$ (line) as a guide to the eye.

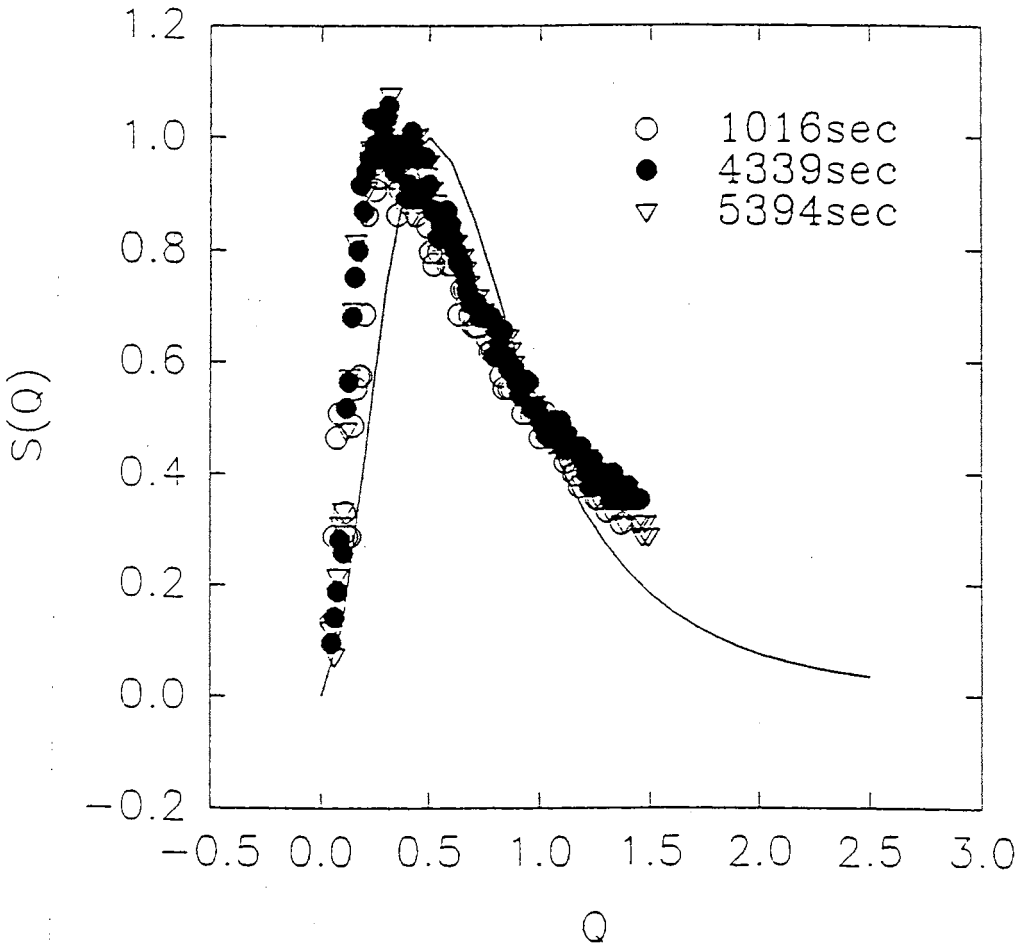

Figure 3.7. Structure factors for data in figure 3.3 in "crossover" time regions are shown and as well as Furukawa scaling function $F(Q)$ (line) as a guide to the eye.

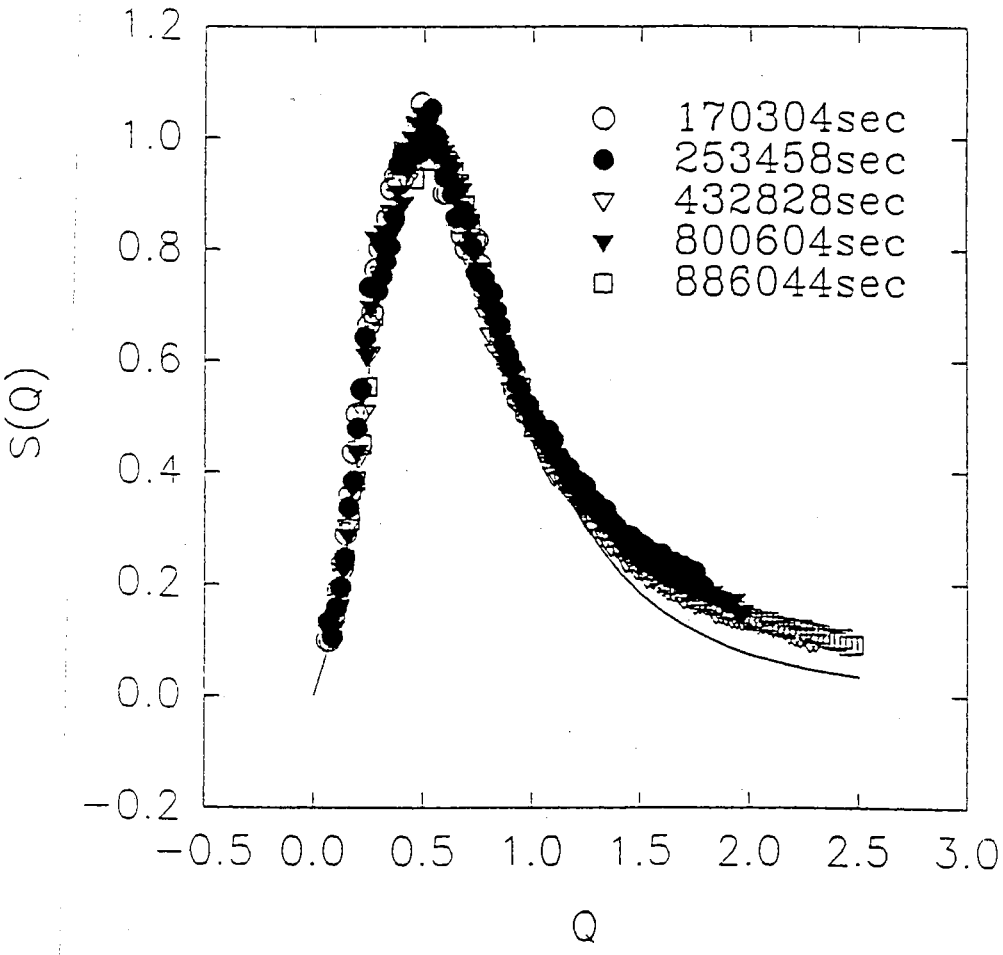

Figure 3.8. Structure factors for data in figure 3.3 in "ripening" time regions are shown and as well as Furukawa scaling function $F(Q)$ (line) as a guide to the eye.

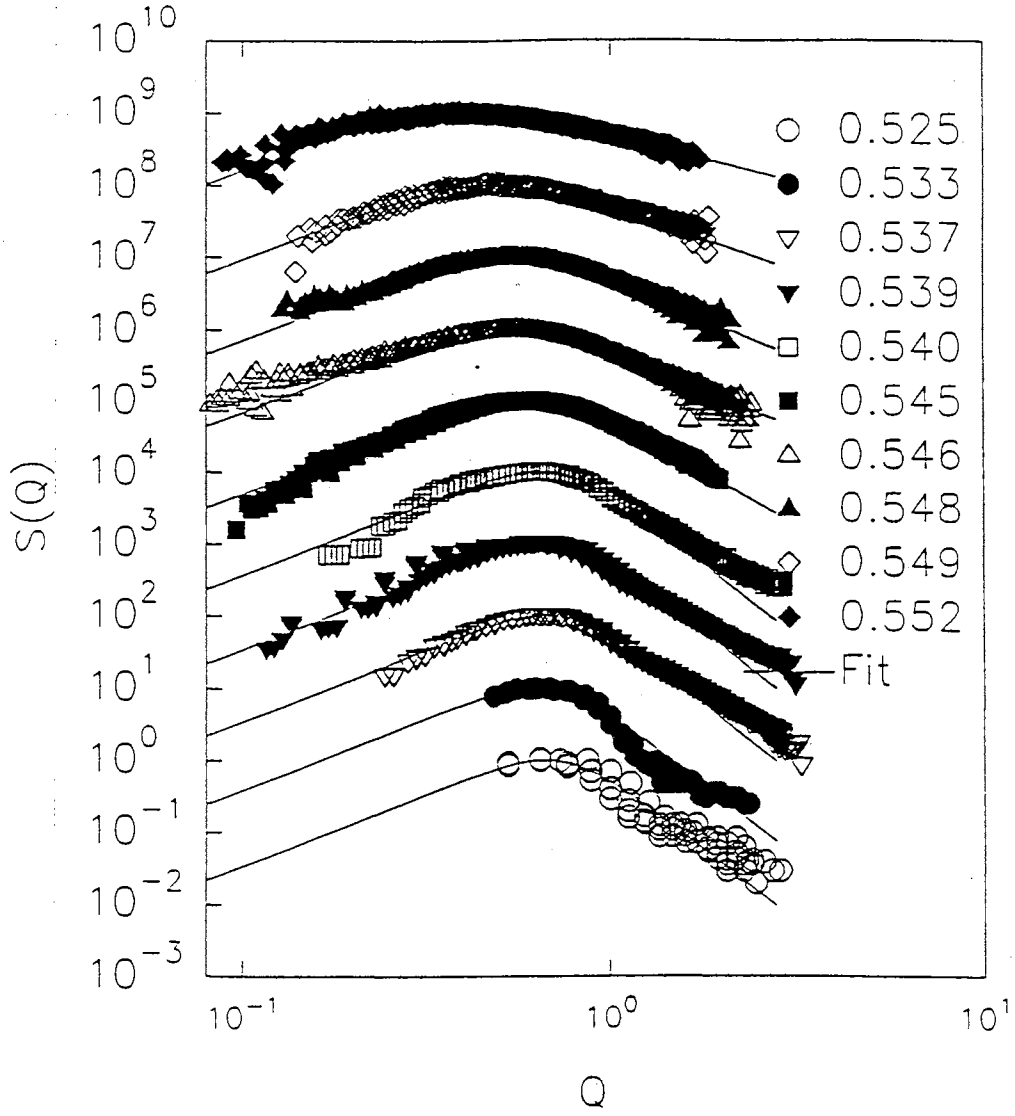

Figure 3.9. Structure factors for various volume fraction samples in "nucleation and growth" time region.

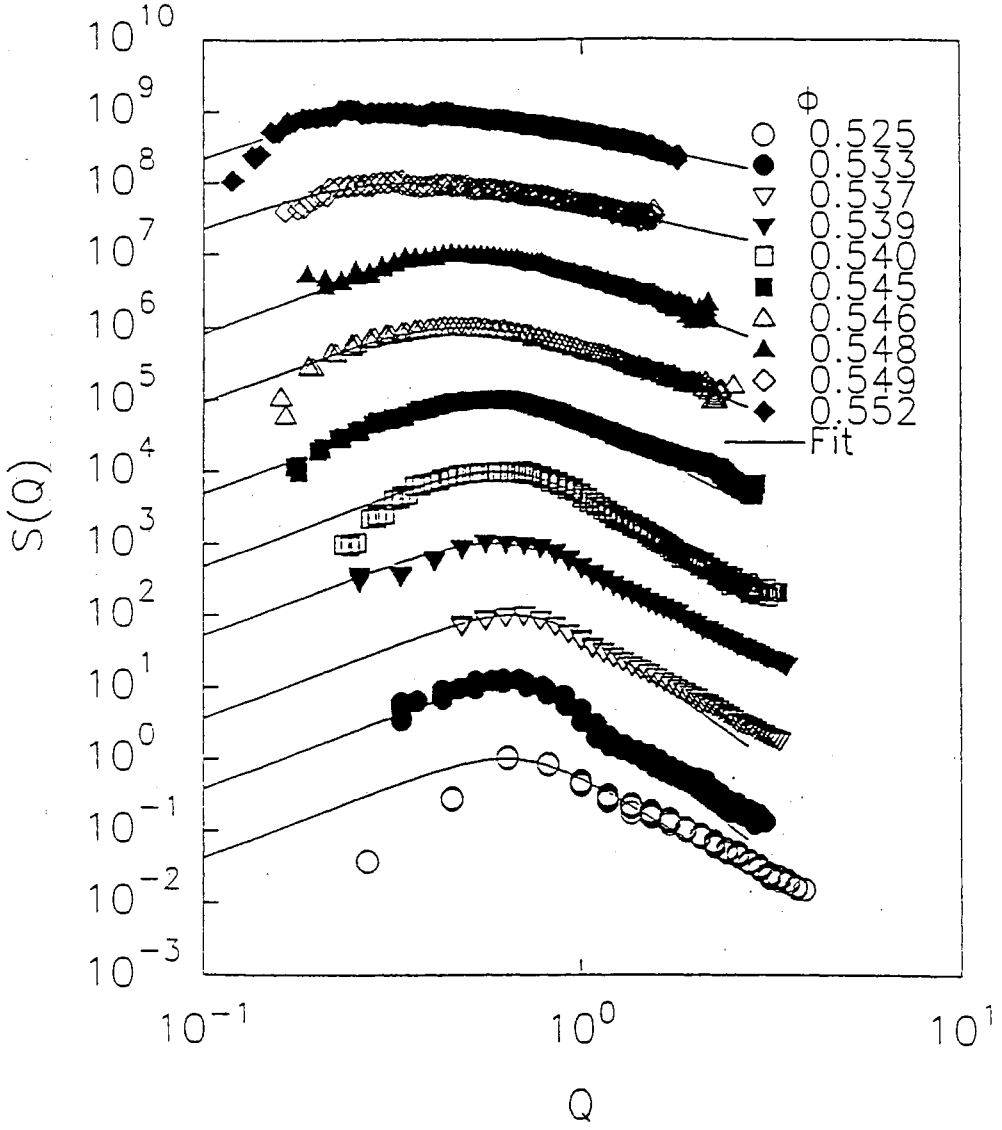

Figure 3.10. Structure factors for various volume fraction samples in "crossover" time region.

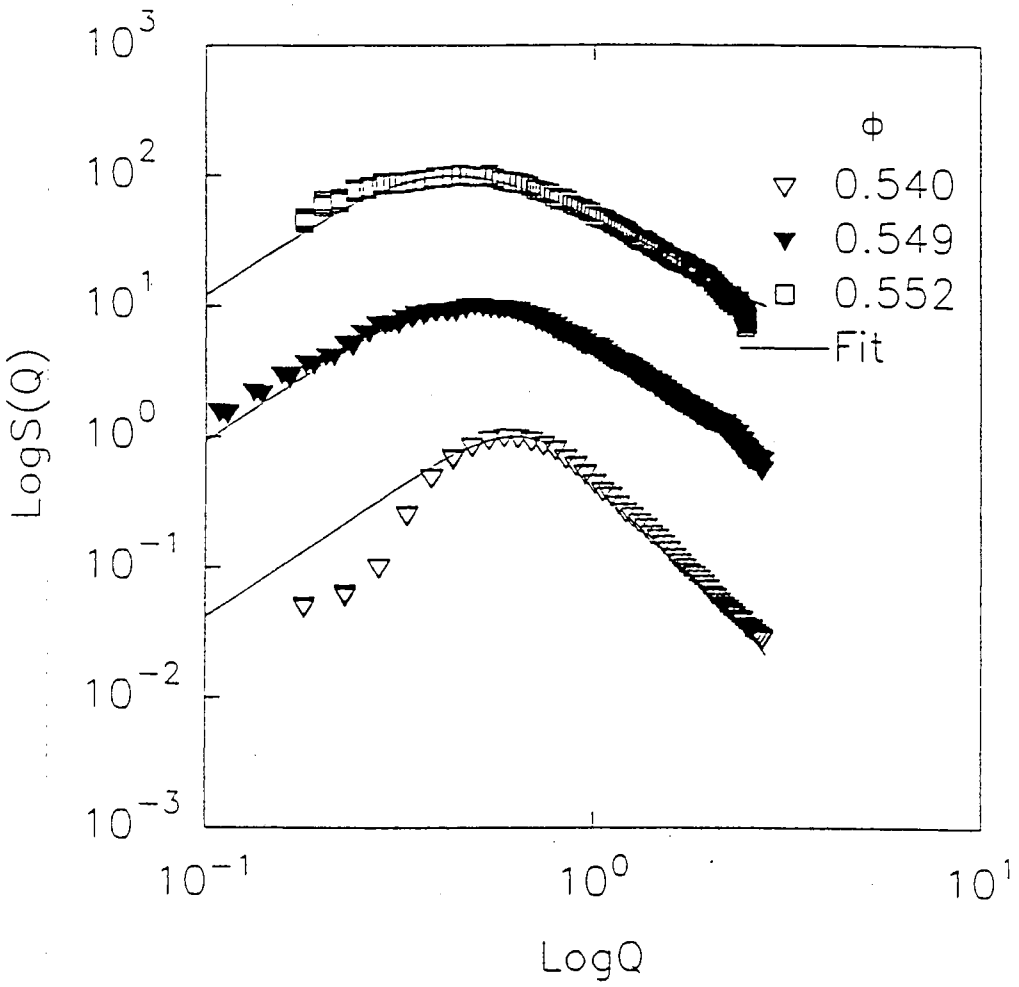

Figure 3.11. Structure factors for various volume fraction samples in "ripening" time region.

where

$$Q' = f(\phi)Q. \tag{3.3}$$

Here the exponent $\gamma(\phi)$ and the scale parameter $f(\phi)$ are fitting parameters which depend on volume fraction. Table I presents values for $\gamma(\phi)$, and values for $f(\phi)$ are redundant since they are a result of the definition of $q_{1/2}$ not being at the intensity maximum. Due to solvent evaporation during the duration of these experiments a given sample could be used to obtain data at several different volume fractions, and these are included in Table I. The form of equation (3.2) is quadratic in the small $Q\prime$ limit. The data in the nucleation and growth region, where small $Q\prime$ data is most accessible, are reasonably consistent with this form. In the ripening region the larger characteristic lengths make this region less accessible. For the larger volume fraction samples measured,the Furukawa form gives a reasonable fit to the data for the full $Q\prime$ range. However at the lower volume fractions, there is a more complicated large $Q\prime$ asymptotic dependence which may be constructed from two power law decays with different exponents. In Table I values of $\gamma(\phi)$ are given for a fit which neglects the large $Q\prime$ asymptotic behavior and a result in parenthesis which fits to the large $Q\prime$ values. For the smaller volume fraction sample ($\phi = 0.539$) we see an evolution from the complex decay behavior in the nucleation and growth region at large $Q\prime$ values to a single power law decay in the ripening region. We do not want to argue any general significance for using the Furukawa form (and in fact, the exponents are far different from those usually found in liquid-gas and fluid demixing transitions), but we find it a convenient form to fit the data.

Discussion

The motivation for this work was to check previous results with a different system, to expand the scattering vector space available to our apparatus

by effectively reducing the crystal size, to reduce the effects of sedimentation by using smaller size particles, and to expand the range of volume fractions studied. However, measurements at large volume fractions were ultimately limited by diminished sample scattering with either size particles. At smaller volume fractions, crystallite sizes typically were larger for the smaller particles systems and confounded our attempts to improve apparatus resolution. The region between nucleation/growth and ripening, the "crossover region", became more pronounced for the smaller particle samples and limited our ability to study ripening compared to the larger particle systems. We now make more explicit these differences with earlier work and offer explanations in terms of possible deviations from hard sphere behavior, sample polydispersity and gravitational effects.

Comparison with previous hard sphere studies

The data presented here for 0.22μm radius particle samples extend and contrast with earlier small angle light scattering studies made for suspensions containing 0.50μm radius particles[6]. Other than the differences in particle radius the same solvents, PMMA particle cores, and steric stabilizers are used in both of these sample systems. Numerous studies on both systems indicate that they approximate suspensions of hard colloidal spheres[12,14–16]. Qualitatively, the crystallization process is similar. After cessation of shear melting, there is a rapid increase in the intensity of forward scattered light. The intensity distribution is in the shape of a ring which exhibits scaling and collapses in size during the "nucleation and growth" phase. There is a "crossover" region followed by a "ripening" phase. The shape function in the nucleation and growth region is found to be similar to that in the ripening region for the larger volume fraction samples.

A comparison of the two different radii samples is given in figures 3.12, 3.13 and 3.14. The reduced elapsed time $\tau_c = D_0 t_c / a^2$ taken to reach the maximum intensity I_m (beginning of the crossover region) is shown in figure 3.12 as a function of volume fraction. Here a is the particle radius, D_0 is dilute solution particle diffusion constant and t_c is the elapsed time to the maximum in I_m. The

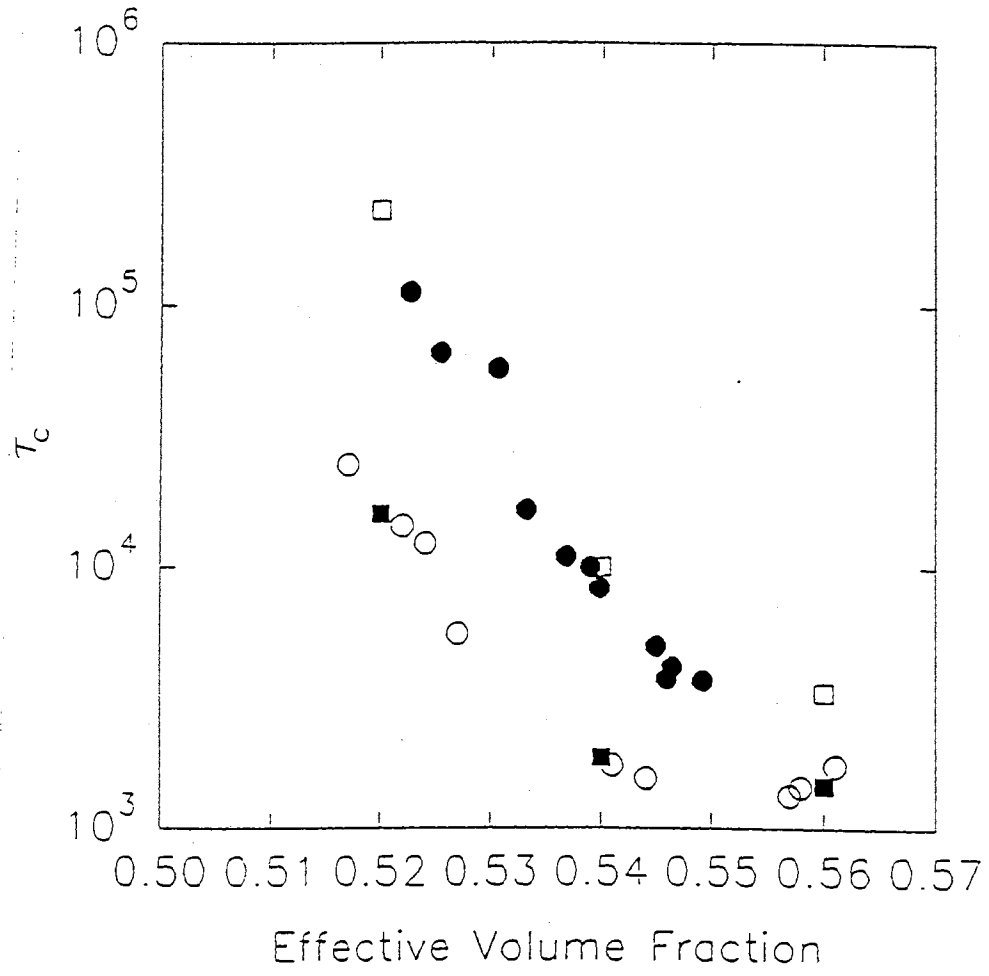

Figure 3.12. The elapsed time to the I_m maximum given by Dt_c/a^2 as a function of volume fraction for 0.49 μm (o) and 0.22 μm (•) radius particles. The open and solid squares are from computer simulations with $\delta = 0.1, 0.05, 0.004$ for open squares and $\delta = 0.04, 0.026, 0.013$ for the closed squares, respectively.

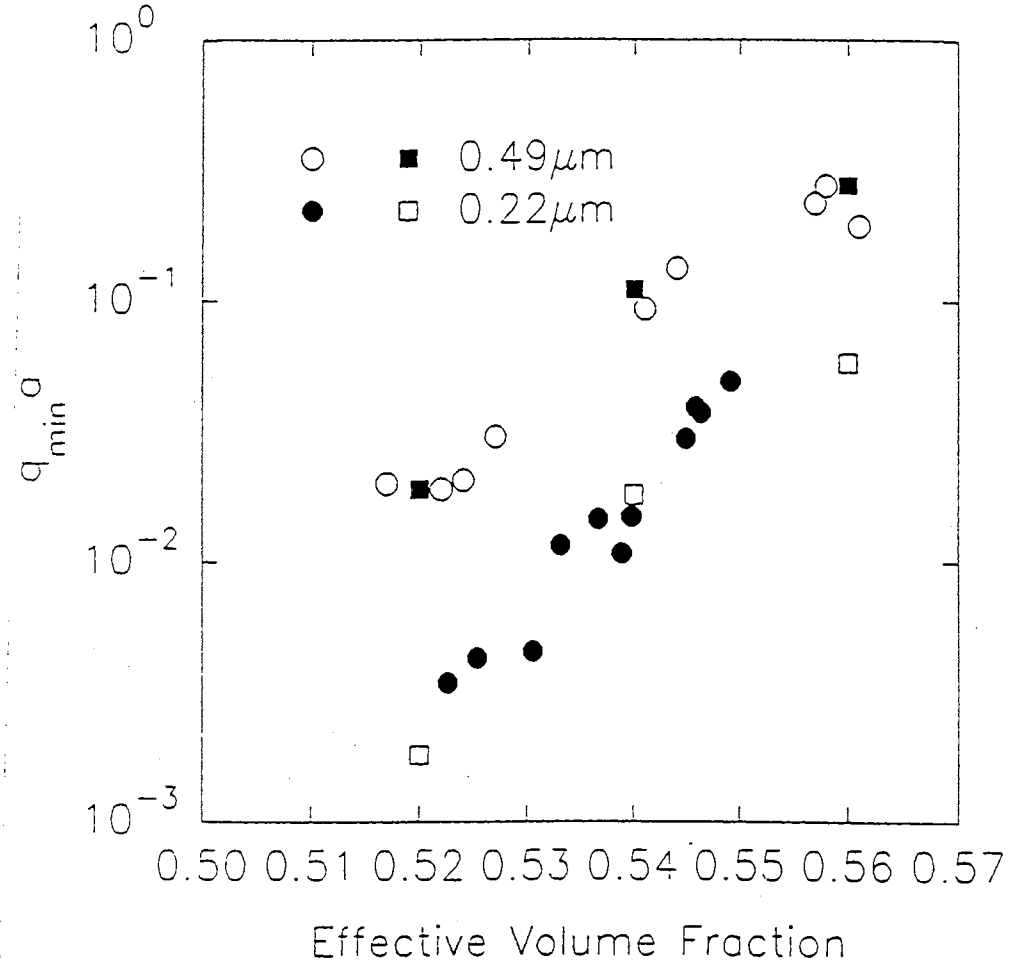

Figure 3.13. The reduced $q_{1/2}$ minimum given by $q_{min}a$ as a function of volume fraction for 0.49 μm (o) and 0.22 μm (•) radius particles. The open and solid squares are from computer simulations with $\delta = 0.1, 0.05, 0.004$ for open squares and $\delta = 0.04, 0.026, 0.013$ for the closed squares, respectively.

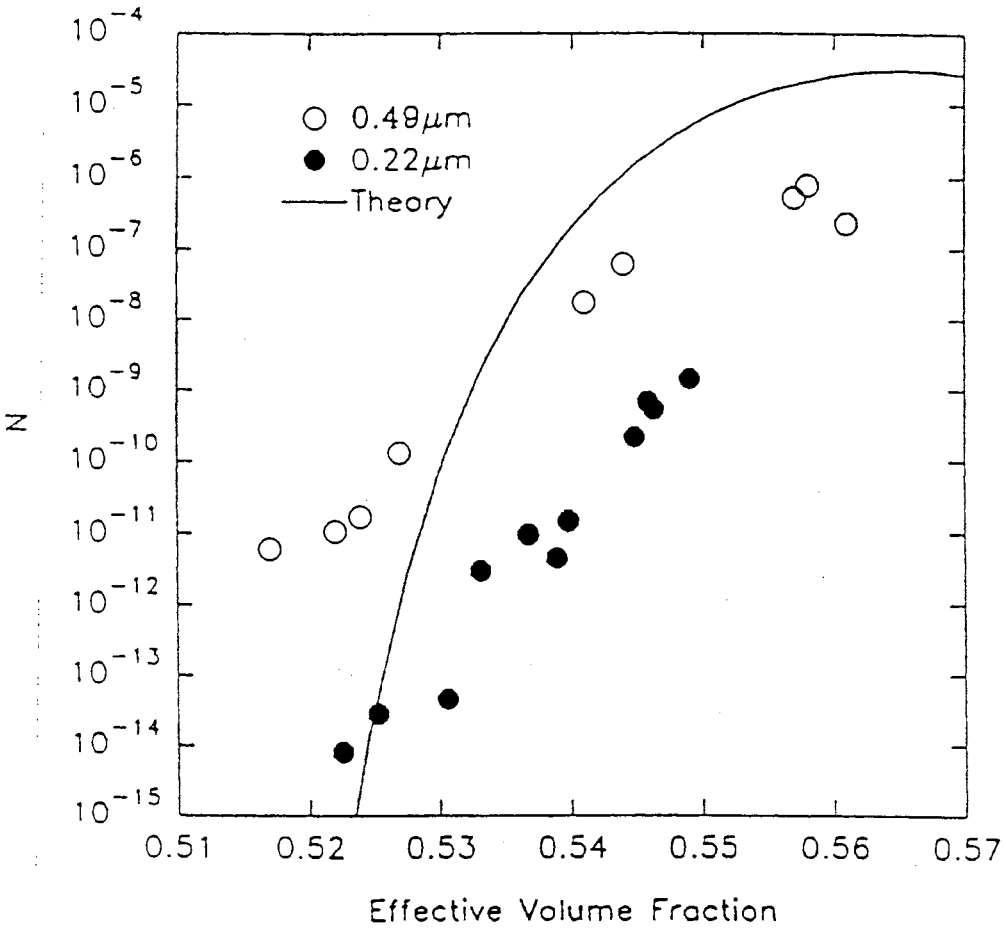

Figure 3.14. The nucleation rate density given by N as a function of volume fraction for 0.49 μm (o) and 0.22 μm (•) radius particles. The solid curve is the predicted value from classical nucleation theory for hard spheres.

reduced wavevector $q_{min}a$ at the beginning of the crossover region is a local minimum for the smaller radii particles and is shown as a function of volume fraction in figure 3.13. In figure 3.14 an estimate of the nucleation rate density is given using values presented in figures 3.12 and 3.13. During nucleation and growth it is assumed that crystal positions are random (uncorrelated) and that the small angle scattering is produced by the crystal form factors[6,10]. The growth process produces a depletion zone around each crystal, and this leads to a maximum in the small angle scattering at finite wavevector. Model calculations have been made for crystal-depletion zone structures which conserve the total particle number[10] and these give $R = 1.8/q_{\frac{1}{2}}$ as an estimate of crystal size, R. If the equilibrium complement of crystal is realized at t_c and assuming $q_{min} = 1.8/R_c$ remains valid, then the nucleation rate density, N, in the coexistence region is given by

$$N = \frac{(\frac{\phi - 0.494}{.545 - .494})}{4\pi R_c^3 t_c/3}. \tag{3.4}$$

This is simply the fraction of sample filled with crystal divided by the size of the average crystal and the elapsed time of the measurement.

Recently a classical theory for the nucleation and growth of colloidal crystals has been proposed [9,34] and evaluated numerically (with some modifications) for suspensions of hard spheres [23]. Within this classical theory the critical nucleus size, r^*, reduced by the particle radius, a, is given by

$$(r^*/a) = 8\pi\gamma_{f-s}a^2/(3\phi_s(\mu_f - \mu_s) \tag{3.5}$$

and the free energy "barrier to nucleation" at this critical size is given by

$$\Delta G(r^*) = (4\pi\gamma_{f-s}a^2/3)(r^*/a)^2. \tag{3.6}$$

Here the averaged crystal surface tension is given by γ_{f-s} and the difference in chemical potential between the metastable fluid and crystal by $\mu_f - \mu_s$, while the crystal volume fraction is ϕ_s. The chemical potentials and the surface energy are

known from computer simulations of hard spheres [13] and analytic calculations [37,36,34]. The nucleation rate density is given by

$$N = \beta(D_s(\phi_f)/a^5)\phi_f^{5/3} exp(-\Delta G(r^*)/kT) \tag{3.7}$$

where $D_s(\phi_f)$ is a self diffusion constant which may be estimated from experiments [34] and β is a parameter expected to be of order unity, although in application of classical theory to atomic systems it may vary from unity by several orders of magnitude [38]. Crystal growth is assumed to follow a Wilson-Frenkel law,

$$dX/d\tau = \delta[1 - exp((\mu_f - \mu_s)/kT)], \tag{3.8}$$

where X is the crystal diameter reduced by the particle radius, $\tau = D_o t/a^2$ is the reduced time introduced previously, and $\delta = \alpha D_s(\phi_f)/2D_o$ is a reduced velocity with alpha an adjustable parameter thought to be of order unity. The self diffusion constant in the Wilson-Frenkel law need not be identical to the one presented in the nucleation rate density.

The theory is compared with experiment for growth by using the "known" values for the surface tension and chemical potentials, but adjusting the parameter δ so that the size R_c at time t_c agrees with the experimentally observe values. These sizes and times are shown in figures 3.12, 3.13 and 3.14 for the two different size particle suspensions. For pure hard spheres δ is a function of volume fraction only, and we find a fit to the small particle growth data gives δ values approximately the same (within $\sim 2x$) that for the larger particle samples at the same volume fraction. The reduced nucleation rate density theoretical results are also shown using a form for the self diffusion constant, $D_s(\phi) = D_o(1 - \phi/0.58)^{1.74}$, given by van Duijneveldt [34] and assuming β is unity. Clearly the two different particle sizes give different results, and the theory could fit either (but not both) equally well if one has complete freedom to adjust β. The theory shows a much stronger dependence on volume fraction than the data as the freezing point is approached.

The source of the discrepancies between the two different particle size systems merits further comment. While it has been claimed that these particle

systems are close approximations of hard sphere systems, it has also been argued that the stabilizing layer introduces some "softness" into the interaction which becomes more important as the ratio of the stabilizing layer thickness to the particle radius increases[18]. The rate of crystallization has been reported to increase in silica particle systems when this ratio is increased[3]. Furthermore, charge stabilized particle suspensions, though at much lower particle volume fraction, have soft interparticle interactions and evidence a rapid crystal growth linear in elapsed time to produce rather large crystals[7]. Another indication of softness could be the increase in scaling factor applied to ϕ_w to obtain ϕ as particle size decreases. These observations may lead one to suspect that softer interparticle interactions between the smaller particles are responsible for the observed differences reported above. However, the rate of nucleation is actually slower for the smaller particles (figure 3.14) when scaled to account for particle size. Furthermore, the phase diagram is consistent with that for hard spheres where the coexistence region width is 10% of the freezing value. For softer repulsive potentials the coexistence region is expected to become relatively more narrow [19,20]. Other studies of the width of the coexistence region, which change ratio of stabilizing layer thickness to particle radius for PMMA core particles and a poly(12-hydroxystearic acid) coating, show similar hard sphere behavior[16]. In addition, low shear viscosity measurements on PMMA particles by Mewis[18] show expected hard sphere behavior. At large stresses or volume fractions the softness of the interaction may need to be taken into account, but this "softness" does not seem to be important for nonsheared samples undergoing crystallization. We conclude that "soft" interparticle interactions are not the primary cause for the observed differences between the large and small particle suspensions.

Another factor which could influence the crystallization properties of the suspensions is the polydispersity. It is measured to be 7% for the small particle samples and 5% for the larger particles samples[6]. This is not a large difference but may be significant. As polydispersity increases both the nucleation rate and the growth rate may be reduced. A single large particle in the presence of small

ones can distrupt or delay the formation of a critical nucleus of smaller particles, until the larger particle has diffused out of the way. Similarly, the growth rate is slowed, because not every particle is the right size to fit into the growing front of a crystal. Evidently the self diffusion constants appropriate for nucleation and growth in monodisperse suspensions should be modified to include this slower diffusive process. Polydispersity can also slow the ripening process, because "misfits" are expelled from crystals into the grain boundaries. These impurities act to pin the boundaries and slow the ripening.

The reduced nucleation rate density noted in figures 3.12, 3.13 and 3.14 for the smaller particle samples are in agreement with these arguments, since the polydispersity is larger for these samples. The larger crystal sizes observed in the smaller particle samples result from the reduced nucleation rate density, which allows more volume for a crystal to grow into before the onset of ripening. For sufficiently high polydispersities, the order-disorder transition is suppressed [39]. However, in our studies the polydispersity is not sufficiently large to evidence any narrowing of the coexistence region for the smaller particle samples. Thus we conclude that polydispersity is a candidate for the observed differences measured in the two different size particle samples but a quantitative theory needs development. Evidently polydispersity has no significant influence on the growth rate.

Another difference between the two sample systems is the effect of sedimentation. In dilute suspension the sedimentation velocity is given by the ratio of buoyant weight of the particle to the Stokes' drag[21] and is proportional to the particle radius squared. When sedimentation velocities are scaled by this number, the values obtained depend only on particle volume fraction[12]. Thus the ratio of the sedimentation velocities of the small to the large particles is 0.19, and this five-fold difference is evident in the time taken to characterize the phase diagram for each system (13 days vs 62 days, respectively, from the sedimentation data of large particle sample p4[6] and small particle sample p7 which have almost the same concentration). No measurable sedimentation is observed in these systems until elapsed times corresponding to ripening, as can be seen in figure 3.15.

However, at t_c, the onset of the crossover region, the samples have probably realized the equilibrium complement of crystal and must simply phase separate over a long period of time into colloidal liquid and colloidal crystal rich regions. For the volume fractions studied (greater than $\phi \sim 0.52$), the samples contain $\sim 50\%$ crystal or more in equilibrium. Assuming uniformly sized spherical particles and placing them at the vertices of a cubic lattice, one finds that the separation between surfaces of nearest neighboring particles is less than 2% of their diameter. Thus very little sedimentation is required to achieve large percolation clusters of crystals. These networks would be sensitive to gravitationally induced stresses. Since the gravitational forces on particles are proportional to the bouyant weight, restructuring is expected to occur faster in the larger particle samples. Indeed the crossover region is smaller or absent in the larger particle samples. We believe this is the primary cause of the differences in time to ripening in the two different systems. However, polydispersity could also slow the ripening by trapping "miss-fits" in the grain boundaries, but the "pinning" of grain boundaries can give a smaller power law growth behavior than that observed here.

Small times

The intensity maximum I_m initially increased proportional to the fourth power of the elapsed time in the larger particle systems for volume fractions at and below the melting point. Above the melting point the power law exponent was difficult to determine because the data was near the noise floor of the apparatus. The exponent appeared to be somewhat less and on the order of three. For the same time range the characteristic wavevector $q_{1/2}$ showed little measurable change at the largest volume fractions but decreased with a power law exponent of 0.5 at the melting point and a slightly larger exponent at the smallest volume fractions studied. These exponents suggested a diffusion limited growth process in contrast to the linear growth observed in charge stabilized particle suspensions [2]. A simple crystal growth model was introduced to explain these data [5,10]. It was assumed that randomly positioned single crystals and associated depletion zones produced

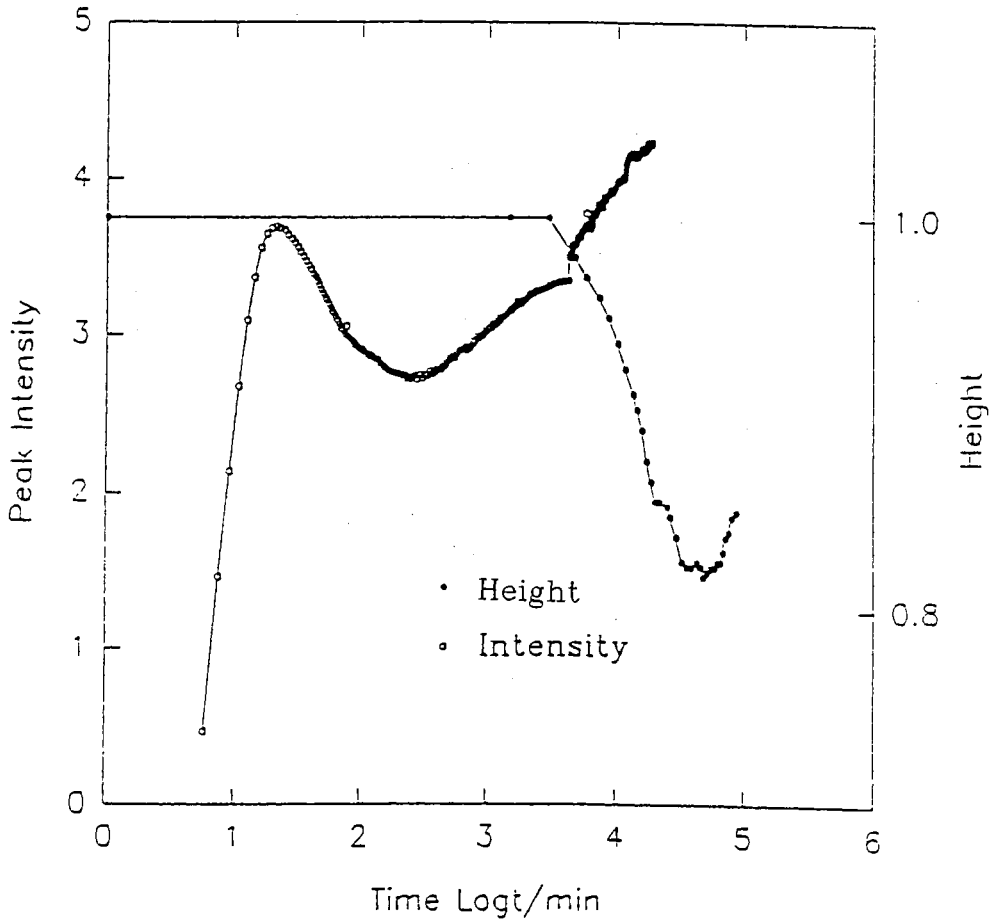

Figure 3.15. This plot compares the time evolution of $I_m(t)$ in sample p4 with the observed sedimentation. Measurable sedimentation is observed only well into the ripening range.

the small angle scattering. The magnitude of the scattering is proportional to the sixth power of the crystal size times the number of scatterers. This size is proportional to the reciprocal of the characteristic wavevector and a constant rate of nucleation is assumed. With these assumptions one finds

$$I_m \sim q_{1/2}^{-6} t \sim t^{6\alpha+1} \tag{3.9}$$

where α is the exponent characterizing the time dependence of the wavevector. For $\alpha = 0.5$ the growth exponent for the intensity is 4.0, as observed[6].

For the small particle samples the growth exponents for I_m are found to be larger, being 4.66 at $\phi = 0.531$ and increasing to a maximum of 7.15 at $\phi = 0.545$, then decreasing to 5.75 at the melting point. The noise floor limited accurate determination of growth exponents for $\phi > 0.552$ which appeared smaller (~ 3.3) than that determined at the melting point. The characteristic wavevector exponents α were also found to be larger, approximately 0.75 at lower volume fractions up to 1.01 at the melting point.

To determine the validity of the model summarized by equation (3.9), we plot the intensity growth exponent and $6\alpha + 1$ as a function of volume fraction in figure 3.16. At the lower volume fractions these exponents agree with the model, suggesting a constant nucleation rate as assumed previously for the larger particle systems. Near melting, however, the exponents differ by order unity indicating only an initial burst of nuclei. This has also been suggested as an explanation for the behavior of the largest volume fraction of the larger particle samples[6].

A range of exponents similar to those measured for α has been observed recently[23] in calculations of crystal growth based on the classical theory of nucleation and growth adapted to suspensions of hard spheres[9]. In these calculations the volume fraction and the speed with which particles become incorporated into the growing crystal determines whether the growth is diffusion limited ($\alpha = 0.5$), interface limited ($\alpha = 1.0$), or has an approximate power law behavior with an intermediate exponent. For growth in the coexistence region with a large incorporation rate, the growth is diffusion limited with $\alpha = 0.5$. For smaller incorporation

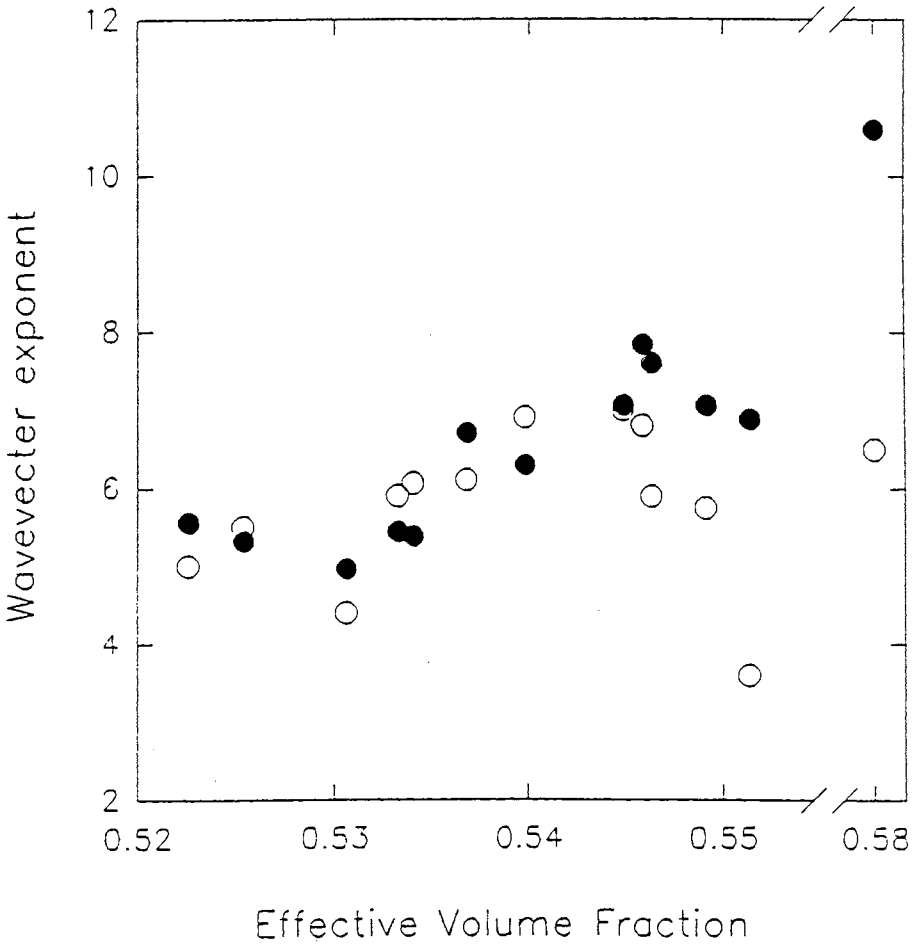

Figure 3.16. Intensity growth exponent (o) and $6\alpha + 1$ (•) as a function of volume fractions.

rates the growth is slower and not diffusion limited. The growth evolves as an approximate power law with exponent $\alpha > 0.5$. Thus the slower growth of the smaller particle samples (due to polydispersity?) is consistent with the larger growth exponents. The maximum growth exponents we found in our model calculations for the smaller hard sphere particle suspensions were for $\phi = 0.52$, from $\alpha = 0.58$ at $\delta = 0.5$ to $\alpha = 0.74$ at $\delta = 0.05$, for $\phi = 0.54$, $\alpha = 0.75$ at $\delta = 0.05$, and for $\phi = 0.56$, $\alpha = 0.55$ at $\delta = 0.005$. With increasing volume fraction, the growth exponent increases slightly as does the experimental data. However, for volume fractions greater than freezing, the theoretical value is much reduced from unity, due to finite size effects. The growth never has time to approach the limiting value because of competition with neighboring crystals for metastable fluid.

The crossover region for the smaller particle samples is similar for all volume fractions studied in the coexistence and fully crystalline phases. At the beginning of the crossover, the intensity maximum I_m decreases with increased elapsed time while $q_{1/2}$ increases in value, indicating a decrease in the characteristic length scale. The same behavior is observed for the larger particle samples for volume fractions less than approximately 0.54. However, for volume fractions at or above melting in the larger radii particle systems, I_m exhibited a brief inflection and no decrease in value with increasing elapsed time. Correspondingly $q_{1/2}$ became constant before decreasing again in the ripening region. The shape function evidenced deviations from the early and late elapsed time forms similar to that shown in figures 3.6, 3.7 and 3.8. Given the relationship between scattered intensity and characteristic length scale in equation (3.9), the decrease in scattered intensity would seem to correlate with the observed decrease in characteristic length scale. For the smaller volume fraction samples ($\phi < 0.535$), the intensity maximum I_m and $q_{1/2}$ reverse directions at the same time (t_c). However, as the concentration of crystals becomes large enough that depletion zones overlap, the proposed scattering mechanism for the nucleation and growth region is corrupted. This is suggested for volume fractions $\phi > 0.535$ by the fact that the intensity maximum I_m begins its decrease before $q_{1/2}$ reaches its minimum (largest characteristic length). Thus

we picture independent, spatially uncorrelated nuclei to form and grow initially; but as the sample fills with crystals and depletion zones overlap and control the growth of crystals, the crystals become spatially correlated. The crossover region represents the change from a length scale correlated with the "size" of individual crystals to a length scale correlated with the "separation" between neighboring crystals. Since the crystals are in contact in the ripening region, the later length scale is also a measure of crystal "size".

Bragg scattering from the first order peak has been monitored during the crystallization process for a similar hard sphere suspension [40]. This method works best for volume fractions at melting or larger due to the large number of crystallites scattering to the diode array detector. The small angle scattering works better for smaller volume fractions where there is increased scattered intensity due to increased crystal size, in general. Thus the two methods complement one another. The integrated intensity of the Bragg peak, X, is a measure of the crystal fraction. It shows a rapid increase with exponent $\mu = 3$ at volume fraction $\phi = 0.530$ and exponent $\mu = 4$ at volume fraction $\phi = 0.548$ followed by a saturation or very slow increase. The reduced times for this change in behavior correlate well with the reduced time in figures 3.12, 3.13 and 3.14. The argument given in equation (3.9) should be modified for Bragg scattering to read $X \sim t^{3\alpha+1}$ if the nucleation rate is assumed constant. The growth exponents then become $\alpha = 0.66$ and $\alpha = 1.0$ for volume fractions $\phi = 0.530$ and 0.548 where we found via SALS $\alpha = .63$ and $\alpha = 1.0$, respectively. This interpretation gives the same growth exponents determined by both methods. If the peak width is used as a measure of the crystal size, then the growth exponents are half the values cited above and the nucleation rate increases approximately with the square of the elapsed time. However, it is in this volume fraction range that these growth law measurements are the least reliable in the Bragg scattering method. Also, the Bragg measurements detect only those crystal planes which are oriented to scatter to the detector, while SALS is sensitive to the whole crystal structure. These planes may grow differently than the crystal as a whole. Finally we note the saturation of X above t_c indicates that

crystallization is completed by this time and this assumption leading to equation (3.4) is valid.

Late times

The extended crossover region for the small particle samples has limited our ability to characterize the ripening region. For three samples (ϕ = 0.540, 0.549, 0.552) data runs have been extended to more than two weeks. In the last week I_m approaches a nearly linear increase with elapsed time, while $q_{1/2}$ decreases with a power law near one third. This is similar to the behavior observed in the larger particle samples at the melting point. It may be understood[5] as a ripening process where nearly equilibrium values of liquid and crystal are present, but larger crystals grow at the expense of smaller ones. For example, if the characteristic crystal size is R, then the scattering intensity for a single crystal will go like R^6, the number of scatterers like R^{-3} and the total scattered intensity as R^3. This total intensity increases linearly in time if $q_{1/2}^{-1} \sim R \sim t^{1/3}$. The growth exponent equal to 1/3 is common in coarsening processes, especially where the order parameter is conserved (known as Lifshitz-Slyozov ripening [24]). Crystallization is described by a nonconserved order parameter, but evidently, the small angle scattering and the crystallization process are controlled by a conserved quantity, the particle density. In contrast with the larger particle samples this growth exponent extends into the fully crystalline region (volume fraction 0.552). In the fully crystalline region the larger particle samples evidenced a larger exponent ($\sim 1/2$) which may increase further with increasing volume fraction. This larger exponent might be expected in fully crystalline samples (Lifshitz-Allen-Cahn behavior[25]).

Scaling and dynamical scaling

Dynamical scaling is often observed[26–30] in nonequilibrium phase transformations or coarsening processes. At sufficiently large times the scattered intensity distribution is given by

$$I(q,t) = q_{1/2}^{-d}(t)F(q/q_{1/2}(t)) \tag{3.10}$$

where d is the dimensionality of the system and F is a shape function. In figure 3.17, I_m is plotted as a function the measured peak intensity I_m is plotted as a function of the corresponding characteristic scattering vector $q_{1/2}$ value in the ripening region for sample volume fractions 0.540, 0.549 and 0.552. The limited data for each sample are compared with the solid line representing a power law behavior with exponent 3.0. All samples measured show reasonable agreement with an exponent corresponding to three dimensional space. While larger particle samples showed the same dynamical scaling in the coexistence region and near the melting point, the exponent was close to 2.0 for the largest volume fractions. This exponent value remains unexplained.

The shape functions do not have universal form but depend on the underlying physical process. General arguments[17] give $F \sim q^2$ as the small wave vector limit for scattering from conserved quantities like particle density. On the other hand, the large wavevector behavior for spinodal decomposition[31,32] is expected[17] to go as $F \sim q^{-4}$ due to well defined surfaces and scattering in the Porod limit[33]. In electrorheological fluids[35] the large wavevector behavior goes as $F \sim q^{-3}$ due to Porod scattering from essentially two dimensional objects. For irreversible aggregation processes[30], the large wavevector limit goes as q^{-d_f} due to the fractal dimension d_f of the scattering clusters. In our samples we expect the small wavevector behavior $F \sim q^2$; however, due to the large characteristic size in the ripening region we could not confirm this behavior with the present apparatus. The large wavevector behavior suggests $F \sim q^{\beta}$ where $1 < \beta < 4$. We believe this results from scattering from a polydisperse collection of crystallites. The polydispersity increases with increasing volume fraction but grows self-similarly at a given

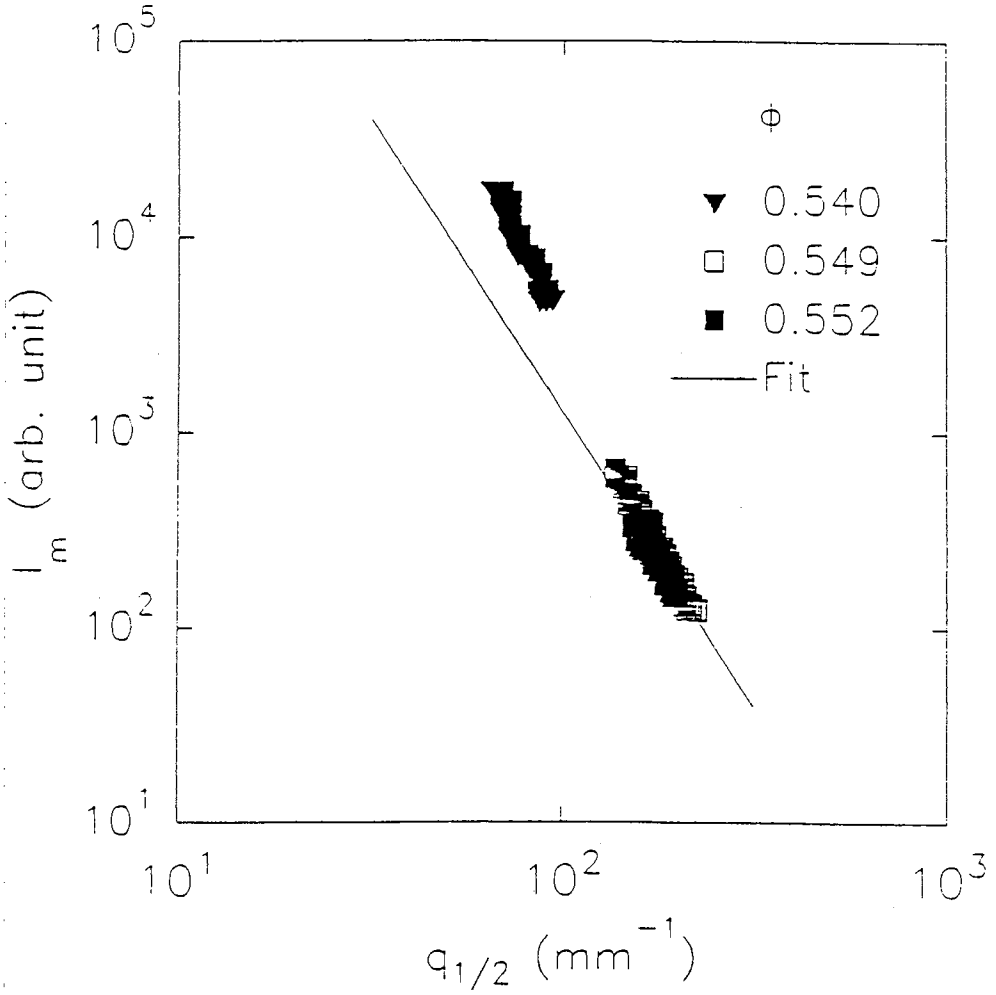

Figure 3.17. Peak intensity $I_m(t)$ as a function of characteristic scattering vector $q_{1/2}$ in ripening region. The linear fit shows a slope of -3 (line) which is expected for dynamical scaling in 3 dimensions.

volume fraction. We do not have a theoretical model for the crystal size distribution but note that the classical theory of nucleation predicts a lower barrier to nucleation as the volume fraction (undercooling) of the metastable state increases. This lower barrier is conducive to a more polydisperse or broader distribution of nucleus sizes.

In the nucleation and growth time regime, the lower volume fraction samples evidence a more complex behavior in the large $Q\prime$ portion of the intensity distribution as seen in figures 3.9, 3.10 and 3.11. When the data is fit near the maximum intensity with $\gamma \sim 4.0$ in the Furukawa function, it is clear that a smaller exponent is needed to fit the largest $Q\prime$ intensities. Preliminary microscopy studies for these lower volume fraction samples indicate that there is some substructure within the crystals[22]. Thus, this complex intensity distribution may indicate both scattering from crystals (near the maximum) and from the substructure (for the high $Q\prime$ tail). In the crossover and ripening regions this complex behavior is eliminated. Because this transformation is accompanied by a decrease in the characteristic length as noted for figure 3.5, it is natural to suggest that the crystals are breaking up into the smaller substructures. The breakup may result from gravitational stresses or dissolution of crystal at internal defects. The computer calculations[23] of crystal growth indicate that these crystals should be compressed to higher than equilibrium osmotic pressures so internal stresses are expected to be present.

Acknowledgements

It is with deep regret that we inform the readers of the untimely death of Klaus Schatzel during the final preparation of this manuscript. B.J.A. and K.S. were supported by grant from the North Alantic Treaty Organization. B.J.A. and Y.H. gratefully acknowledge support from the National Science Foundation through grants numbered DMR 9122589 and DMR 9501865.

Sample	p2	p7	p7	p4	p4	p4	p4	p3	p3	p3
ϕ	0.525	0.533	0.537	0.539	0.540	0.545	0.546	0.548	0.549	0.552
Nuc./Growth	4.0	4.1	4.0(3.4)	4.0(3.5)	4.0(3.0)	2.9	2.2	2.2	1.8	1.3
Crossover	3.1	3.7	3.6	2.8	3.0	2.75	1.8	1.9	1.1	1.1
Ripening				2.9				1.82	1.53	

Table 3.1.

BIBLIOGRAPHY

1. S. Brauer, H. E. Fischer, J. O. Ström-Olsen, M. Sutton, and A. Zaluska, Phys. Rev. B **47**, 11757 (1993).

2. D. J. W. Aastuen, N. A. Clark, J. C. Swindal, and C. D. Muzny, Phase Transitions **21**, 139 (1990).

3. C. Smits, J. S. van Duijneveldt, J. K. G. Dhont, H. N. W. Lekkerkerker, and W. J. Briels, Phase Transitions **21**, 157 (1990).

4. J. K. G. Dhont, C. Smits, and H. N. W. Lekkerkerker, J. Coll. Int. Sci., **152**, 386 (1992).

5. K. Schätzel and B. J. Ackerson, Phys. Rev. Lett. **68**, 337 (1992).

6. K. Schätzel and B. J. Ackerson, Phys. Rev. E **48** , 3766 (1993).

7. D. J. W. Aastuen, N. A. Clark, L. K. Cotter, and B. J. Ackerson, Phys. Rev. Lett. **57**, 1733 (1986); **57**, 2772 (1986).

8. B. J. Ackerson and N. A. Clark, Phys. Rev. Lett. **46**, 123 (1981).

9. W. B. Russel, Phase Transitions **21**, 127 (1990).

10. B. J. Ackerson and K. Schätzel, in *Complex Fluids*, edited by L. Garrido (Springer, Heidelberg, 1992)), p. 15.

11. L. Antl, J. W. Goodwin, R. D. Hill, R. H. Ottewill, S. M. Owens, S. Papworth, and J. A. Waters, Colloids Surfaces **17**, 67 (1986).

12. S. E. Paulin and B. J. Ackerson, Phys. Rev. Lett. **64**, 2663 (1990).

13. W. G. Hoover and F. H. Ree, J. Chem. Phys. **49**, 3609 (1968).

14. P. N. Pusey and W. van Megen, Nature (London), **320**, 340 (1986).

15. B. J. Ackerson, J. Rheol. **34**, 553 (1990).

16. S. M. Underwood, J. R. Taylor, and W. van Megen, Langmuir **10**, 3550 (1994).

17. H. Furukawa, Physica A **123**, 497 (1984).

18. J. Mewis, W. J. Frith, T. A. Strivens, and W. B. Russel, AIChE J. **35**, 415 (1989).

19. S. Paulin, B. J. Ackerson and M. S. Wolfe, J. Colloid Interface Sci., to be published.

20. J. D. Weeks, Phys. Rev. B **24**, 1530 (1981).

21. T. G. M. van de Venn, Colloidal Hydrodynamics, (Academic Press, New York, 1989).

22. Y. He, B. J. Ackerson and B. Olivier, submitted for publication.

23. B. J. Ackerson and K. Schätzel, Phys. Rev. E **52**, 6448, (1995).

24. I. M. Lifshitz and V. V. Slyozov, J. Phys. Chem. Solids **19**, 35 (1965).

25. S. M. Allen and J. W. Cahn, Acta Metall. **27**, 1085 (1979)

26. P. A. Rikvold and J. D. Gunton, Phys. Rev. Lett. **49**, 286 (1982).

27. J. L. Lebowitz, J. Marro, and M. H. Kalos, Actd Metall. **30**, 297 (1982).

28. T. Hashimoto, M. Itakura, and H. Hasegawa, J. Chem. Phys. **85**, 6118 (1986).

29. P. Wiltzius and A. Cumming, Phys. Rev. Lett. **66**, 3000 (1991).

30. M. Carpineti and M. Giglio, Phys. Rev. Lett. **68**, 3327 (1992).

31. Y. C. Chou and W. I. Goldburg, Phys. Rev. A **23**, 858 (1981).

32. C. M. Knobler and N. C. Wong, J. Phys. Chem. **85**, 1972 (1981).

33. G. Porod, in *Small Angle X-Ray Scattering*, edited by O. Glatter and O. Kratky, (Academic Press, New York, 1982).

34. J. S. van Duijneveldt and H. N. W. Lekkerkerker, in *Science and Technology of Crystal Growth*, edited by J. P. van der Eerden and O. S. L. Bruinsma, (Kluwer Academic, Dordrecht, 1995).

35. J. E. Martin, J. Odinek and T. C. Halsey, preprint.

36. D. W. Marr and A. P. Gast, Phys. Rev. E, **47**, 1212 (1993).

37. W. A. Curtin, J. Chem. Phys., **39**, 6775 (1989).

38. K. F. Kelton, in *Solid State Physics*, edited by E. Reich and D. Turnbull, **45**, 75 (Academic Press, New York, 1991).

39. P. N. Pusey, in *Liquids, Freezing and the Glass Transition*, edited by D. Levesque, J. P. Hansen, and J. Zinn-Justin (Elsevier, Amsterdam, 1990).

40. J. Harland and S. Henderson and S. Underwood and W. van Megen, Phys. Rev. Lett. **75**, 3572 (1995).

CHAPTER IV

MORPHOLOGY OF CRYSTALS MADE OF HARD SPHERES

Abstract

A special photographic technique is used to monitor the growth and morphology of crystals in suspensions of hard colloidal spheres. The crystals evidence irregular rectangular and rosette shapes with sharp edges. These edges indicate that the growth occurs below the roughening transition and a simple model for roughening is adapted to hard sphere systems to understand our observations. There is a visible substructure in the crystals which does not result from the aggregation of smaller crystallites. The substructure is measured and compared to the Mullins-Sekerka instability length for hard spheres. The reduction in crystal size inferred between growth and ripening in small angle scattering experiments is attributed to the existence of this crystal substructure. For hard sphere systems this remarkable ordering process is the result of entropy increasing in thermodynamically isolated systems.*

Introduction

A thermally activated collection of identical hard spheres is one of the simplest classical many-body systems. Because the hard sphere interaction is infinitely repulsive at contact and zero otherwise, the potential energy of the system is the same for all particle configurations. As a result temperature is not an important thermodynamic parameter but particle density is. The occurance of a fluid

*will be published (Langmuir (in review)) by: Yueming He, B. Olivier and Bruce J. Ackerson; Department of Physics and Center for Laser Research; Oklahoma State University; Stillwater, OK 74078-0444

to crystal phase transition as density is increased was hotly debated[1] because there is no force to hold the crystal together and so the transition must be driven by entropy. Yet the fluid phase would appear to have a larger entropy than the crystal phase. However, computer simulations[2,3] established the existence of this transition, with the volume fraction of spheres at the freezing point being 0.494 and 0.545 at the melting point. Thus the system is only half full of spheres when freezing begins. Density functional theories[4] support these results and suggest that the transition is driven by a competition between global and local entropies. Entropy can drive even more complex transitions. Recent computer simulations[5] have confirmed that a mixture of two different radii hard spheres will form a complex AB_{13} structure having 128 particles in a unit cell. However, due to electronic and quantum effects which dominate at the atomic level, it is difficult to find an atomic or small molecule system which closely approximates hard spheres.

On the other hand, hard sphere interactions have been approximated at the colloidal particle level using steric stabilization to minimize the van der Waals attraction between particles[6,7]. The particles typically are very uniform in size with diameter in the colloidal range between a tenth and one micron. Suspensions of these particles in organic solvents evidence properties consistent with expected hard sphere behavior. Sedimentation velocities as a function of volume fraction[8,9] show neither a decrease due to longer ranged particle repulsions nor an increase due to particle attractions as compared to predicted theoretical results for hard spheres[10]. These suspensions evidence a fluid to crystal phase transformation with increasing volume fraction particles[11,8,12] which has a coexistence region width in volume fraction equal to one tenth the freezing value $((\phi_{melting} - \phi_{freezing})/\phi_{freezing} \sim 0.1)$ expected for hard spheres but not for softer repulsive potentials [13]. Shear induced microstructures have been understood in terms of the steric interaction of hard spheres[14].

The crystal structure in these suspensions has been determined using light diffraction, the analogue of x-ray powder diffraction for atomic systems[15]. The crystal structure data is described well as a registered random stacking of close

packed planes of spheres. This can be considered as a highly faulted face centered cubic or three dimensional hexagonal close packed structure. Face centered cubic structures are favored energetically when there are long range repulsions between particles extending to second nearest neighbors. Hexagonal close packed structures are favored energetically for attractive interactions of second nearest neighbors. For hard spheres there is no energy of interaction between second nearest neighbors and this leads to the random close packed structure results.

Recently small angle light scattering has been used to monitor the nucleation and growth process in suspensions of hard spheres[16–18]. The scattered intensity distribution scales during nucleation and growth while the characteristic length increases approximately as a power law in time with exponents distributed between one half and unity, the expected limiting values of diffusion and interface limited growth respectively. This growth region is followed by a crossover region where the characteristic length scale is observed to decrease in time before increasing again at the largest observation times. This reduction in crystal size was not expected nor understood.

While microphotography has been used to study growth and morphology of colloidal crystals in charge stabilized particle suspensions, it has not been applied to the more basic hard sphere suspensions. In suspensions of charged stabilized particles, crystals appear spherical, not faceted, indicating growth above the roughening transition[19,20]. The crystal size grows linearly with elapsed time, indicating interface limited growth. On the other hand, unstable Mullins-Sekerka[21,22] growth also has been observed[23]. It is not clear what the morphology of hard sphere crystals should be given the nature of the interparticle interaction and given that the microstructure is highly faulted or random. Computer simulations are not yet powerful enough to answer question involving such long times and large numbers of particles. Are the crystals faceted or do they grow above the roughening transition? Do growth instabilities influence morphology? What can be learned about the mysterious crystal size reduction in the crossover region between growth and ripening? In this article we examine the growth and morphology of hard

sphere crystals using a special microphotographic technique. We evaluate theories for roughening and growth instabilities in the hard sphere limit. The crystal length scale reduction in time, seen in small angle light scattering experiments, is examined photographically.

Experimental Procedure

The sample used in these experiments is comprized of $0.22\mu m$ radius polymethylmethacrylate (PMMA) spheres suspended in a mixture of tetralin and decalin. The solvent ratio is chosen to match the refractive index of the particles and render the suspensions transparent. The particles are sterically stabilized against aggregation with a $\sim 10nm$ thick surface layer of poly-12-hydroxystearic acid. The volume fraction of the sample studied drifted slightly during the three month observation time but was determined by weighing to be in the range $0.522 < \phi < 0.524$. These volume fractions are referenced to the freezing volume fraction as described elsewhere[11,8]. This sample at equilibrium is in the liquid/crystal coexistence region. Before measurements the sample is shear melted to an amorphous metastable fluid state and the elapsed time, t, is measured from the cessation of shear melting. Since crystals appear to the eye approximately an hour after shear melting, there is sufficient time for convection to cease without disturbing the nucleation and crystal growth.

The sample is contained in couvette ($1.0cm \times 1.0cm \times 5.0cm$) with one of the vertical rectangular faces perpendicular to the optical axis of the camera to minimize image distortions. A Nikon series N2000 camera is used with *Kodachrome DX* $35mm$ slide film. The camera optics affords a magnification of approximately $2X$ in the slide image with a further magnification of approximately $12X$ in making figure 4.1.

The sample is illuminated using a $500W$ tungsten light source which is collimated and weakly focussed with a cylindrical lense ($f = 50cm$) into a thin vertical sheet having an minimum halfwidth of approximately $100\mu m$. The angle that the optical axis of the camera makes with the plane of the sheet of light

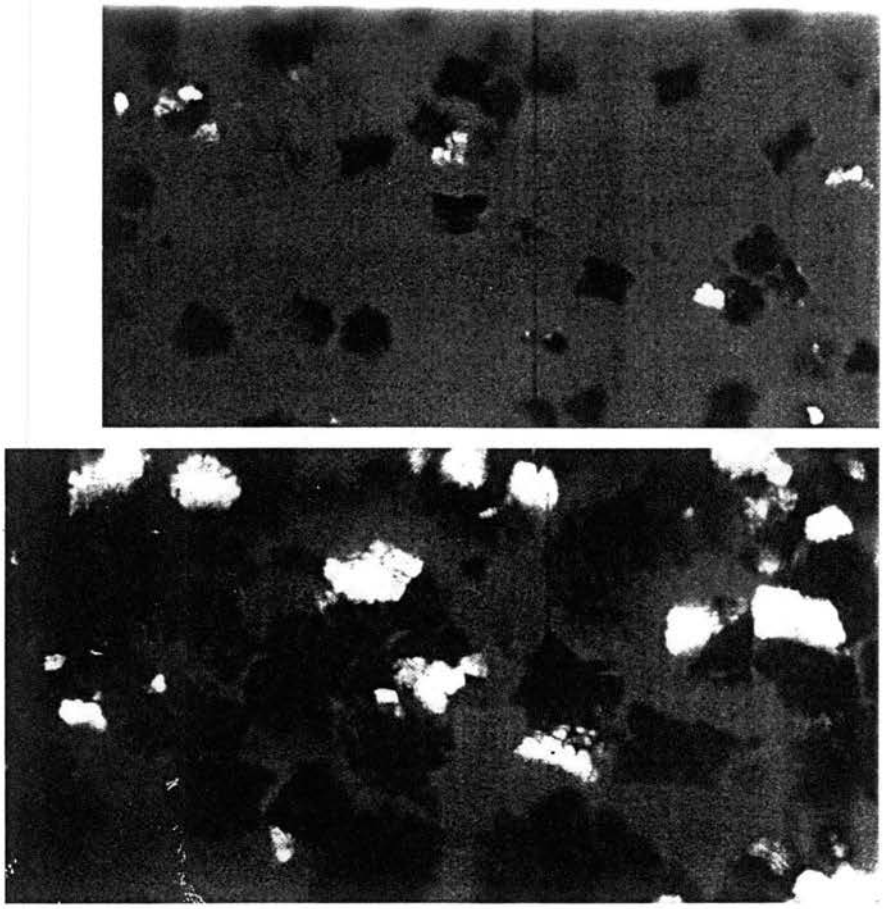

Figure 4.1. Crystal images of a sample ($\phi \sim 0.523$) with a magnification of approximately $24X$ at $t = 135min$ above and $t = 242min$ bellow. We can see the substructures and dendritic growth in the later picture.

corresponds to the first order Bragg scattering angle for one wavelength in the visible spectrum. For this radius particle and wavelength $\lambda = 514.5nm$, the Bragg angle is approximately 55 degrees. Exposure times ranged from 30 to 90 seconds depending on the width of the incident sheet and the actual elapsed time during the crystallization process. The exposure times were, however, much smaller than times corresponding to observable changes in the crystal growth.

The growth of individual crystals, as shown in figures 4.2 and 4.3, are captured from the original photographic slides by the following image processing procedure. The slides are illuminated with diffuse light and digitized using a CCD camera and high resolution frame grabber. The resolution, however, was limited by the camera to approximately 640 $\times$ 480 pixels on a 3/4" active surface. The magnification was increased by a factor of $9X$ by using a continuously focusing microscope attached to the camera. Care was taken to insure a uniformly illuminated photograph in order to minimize artifacts which could arise from non-uniform background fields. The image processing consisted of contrast enhancement of regions of interest.

Small angle light scattering measurements were made for this sample following the procedure in earlier studies[16–18]. The circular scattered intensity pattern evidences a maximum at finite scattered wavevector. The position of the maximum initially decreases in radius, increases, and decreases again. In figure 4.4 the initial decrease and increase may be seen. Also shown in this figure are estimates of crystal radius from photographs. The radius is estimated from the square root of the average area of the ten largest crystals observed in each photographic slide at each time. The image processing technique described above is used to capture images from slides. Schatzel and Ackerson[17] gave a relationship between average crystal size, R, and the larger wavevector at half the maximum peak value (done to increase measurement accuracy), $q_{1/2}$, as $q_{1/2} = 1.8/R$. This has been used to reduce the radius data for figure 4.4. These measurements were taken last when evaporation increased the sample volume fraction to 0.524.

Figure 4.2. Time evolution of a crystal. This series of pictures are captured from the photographic slides by a CCD camera attached with a continuously focusing microscope and a PC.

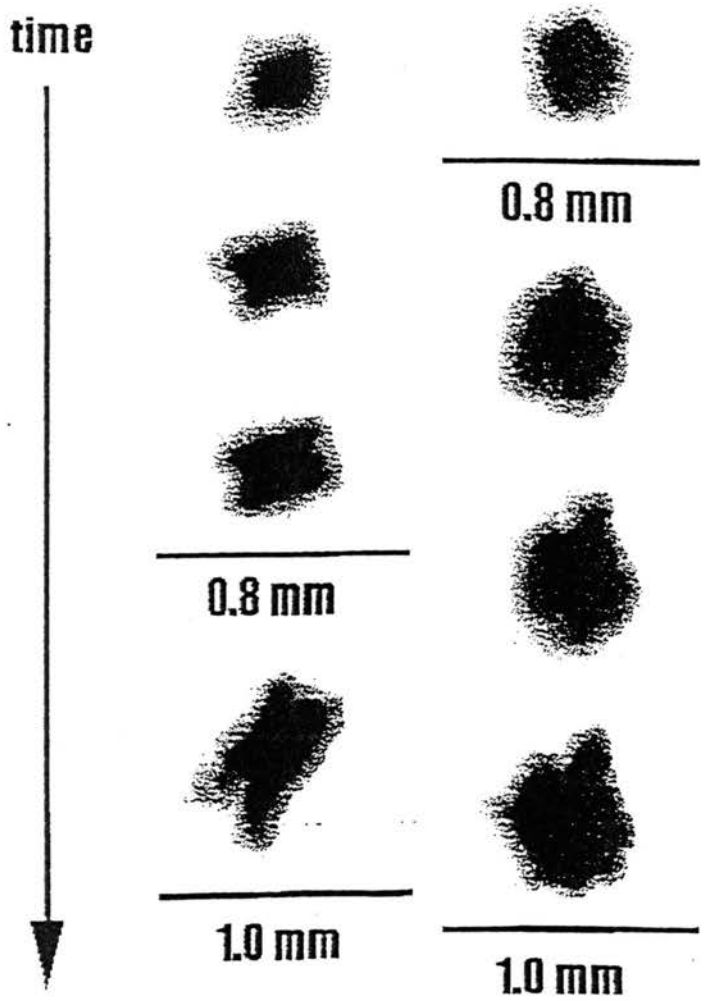

Figure 4.3. Pictures are captured from the photographic slides by a CCD camera attached with a continuously focusing microscope and a PC. Growth of two characteristic crystals are shown. Protrusions are developing.

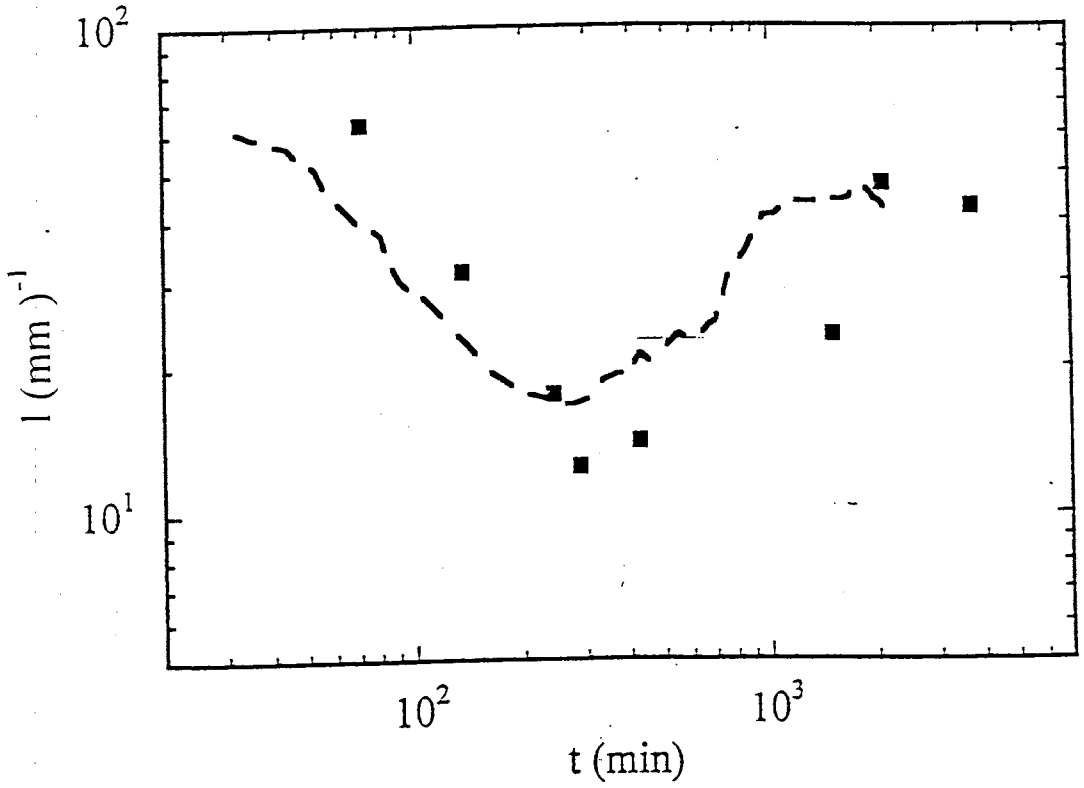

Figure 4.4. Changes of crystal size with elapsed time. The line is small angle light scattering data, $q_{1/2}(t)$. The fill square is $1.8/R$, which R is the square root of the average area of the ten largest crystals in each photographic.

Results and Discussion

Figure 4.1 shows images from photograph slides taken at the first order Bragg angle at $t = 135min$ (a) and $t = 242min$ (b) after shear melting. The lighter crystals have their planes "properly" oriented relative to the incident beam to Bragg scatter the incident light. The darker structures are crystals having non-Bragg scattering orientations relative to the incident sheet of light. These "dark" crystals scatter less light than the surrounding metastable fluid which is near its maximum scattered intensity at this angle. Thus, all crystals within the illuminated region are visible when the crystal size is comparable to the sheet width. Bragg scattering crystals are observed first in time, presumably due to the large scattered intensity and smallness of the crystal size compared to the sheet width in present studies.

Other photographic observations[24] have not used a thin sheet illumination of the sample and only observe the Bragg scattering crystals. In these other experiments light from the forground and background obscures the non-Bragg scattering crystals. Our sheet illumination produces greater clarity of the crystal image, at least in the center of the field of view, where the object plane of the camera and the sheet illumination overlap.

As shown in figure 4.1 the crystals appear sharply defined, largely with rectangular or rosette shapes. At the larger time shown in figure 4.1, the crystals are still sharply defined at the outer boundary, but significant internal structure is also visible and is reminiscent of dendritic growth. These characteristic morphologies were found throughout the sample for all data runs. At even larger times the dark crystals appear to fill the volume of the sample. Here it becomes difficult to resolve individual crystals, and the crystal substructure length scale becomes the dominant visible feature. The crystal substructure does not result from an aggregation of a collection of smaller crystals into a single larger crystal. Rather this substructure may result from a growth instability similar to that which leads to dendritic growth. Figure 4.3 shows the growth of two characteristic crystal

shapes which have been isolated from the original photographic slides. We can see that one crystal with a rectangular cross section grew uniformly and then later developing protrusions at its corners. The protrusions have a width approximately equal to $100\mu m$ at later times. The second crystal in the digitized image has the characteristic rosette shape at early times but also develops an instability at later times. The width of this protrusion is approximately $150\mu m$.

We can compare these length scales with that predicted by Mullins and Sekerka[21,22] for crystal growth instabilities of a planar interface. The Mullins-Sekerka instability results from a competition between diffusion causing growth and surface tension suppressing growth. A planar crystal interface growing into a metastable fluid is found to be unstable to small spatial undulations with wavelengths greater than

$$\lambda/a = 2\pi\sqrt{(l/a)(d/a)}. \tag{4.1}$$

Here the wavelength, λ, is reduced by the particle radius, a, and the mobility ratio of the particle to solvent[25] is set equal to unity. In this equation the reduced diffusion length is given by l/a and the reduced capillary length by d/a. For hard spheres the reduced capillary length is expressed as

$$d/a = \frac{\frac{4\pi a^2\gamma}{3kT}}{\Delta\phi^2\frac{d\mu}{d\phi}} \tag{4.2}$$

where the chemical potential of the metastable fluid may be calculated from fits to computer simulations of the equation of state [26,27]. In these calculations we use the forms for the fluid and crystal (metastable) states, respectively, $\Pi/nkT = Z(\phi_f) = 0.904/((\phi_f - 0.731) + 0.016)$ and $\Pi/nkT = Z(\phi_c) = 2.17/(0.738 - \phi_c)$. Here Π is the osmotic pressure, n is the particle number density, kT is the thermal energy, ϕ_f is the (metastable) fluid volume fraction and ϕ_c is the (metastable) crystal volume fraction[28]. $\Delta\phi = \phi_{melt} - \phi_{freeze}$ is the miscibility gap, ϕ_{melt} is the crystal melting volume fraction, ϕ_{freeze} is the liquid freezing volume fraction. The ratio of the surface energy to thermal energy $\gamma a^2/kT$ is taken to be 0.16[29,30].

The Helmholtz free energy and (for hard spheres) the entropy per particle is given by $A/kT = -S/k = \int Z(\phi)(d\phi/\phi) + c$. If the number of particles is given by N, then the chemical potential is given by $\mu = (\partial NA/\partial N)_{T,V}$ so that

$$\frac{d\mu}{d\phi} = \frac{Z(\phi_f)}{\phi_f} + \frac{dZ(\phi_f)}{d\phi_f} \tag{4.3}$$

The diffusion length is given by

$$l/a = 2D/va \tag{4.4}$$

where D is a diffusion constant and v is the velocity of the growth front. The growth velocity may be estimated using the Wilson-Frenkel growth law for hard spheres[31,28].

$$v = \frac{D_s(\phi_f)}{2a}(1 - Exp[-\Delta\mu/kT]) \tag{4.5}$$

where the self diffusion constant, D_s, is given in the literature[29,31]. The chemical potential difference between the crystal and metastable states, $\Delta\mu$, may be calculated as outlined above and are given in the literature[28]. If the diffusion constant in equation (4.4) is the self diffusion constant in equation (4.5), the minimum instability length is approximately $13\mu m$. If the diffusion constant in equation (4.4) is identified with the collective diffusion constant , the instability length is approximately $36\mu m$. These lengths, which are evaluated for a volume fraction of 0.52, are smaller than the measured lengths cited above by a factor of five. The fastest growing length in this model is larger by a factor of $\sqrt{3}$, which improves the agreement with experimental values. However, crystals do not represent flat surfaces so a comparison with instabilities in the growth of a spherical crystal may be more appropriate. Here the instability begins when the crystal has a radius approximately seven times the critical nucleus radius[25]. At a volume fraction 0.52 the critical nucleus radius is $\sim 8\mu m$ so the initial deviation from spherical behavior should be observed for a radius $\sim 60\mu m$, which is consistent with our observations.

The crystals in figure 4.1 appear to have sharp edges indicating that the growth process may occur "below the roughening transition [19,20,32]". This equilibrium transition has been understood in terms of the two dimensional Ising model[33]. Sharp or faceted surfaces correspond to low temperatures where there is condensation into large regions of "gas" or "liquid". At high temperature the "rough" surface exists which is represented by a single phase in the Ising model. Obviously, the Ising model depends on the energy of interaction between particles and therefore displays a temperature dependent transition. Jackson[19,20] has developed a simpler model which determines the equilibrium state of minimum free energy of a surface based on particle interaction energy with the bulk crystal and with other particles on the surface, as well as, a bulk entropy change and a configurational entropy associated with the particle configurations on the surface.

In the hard sphere colloidal systems, there is no change in internal energy with changing particle configurations so roughening would have to be purely an entropy driven effect. Jackson's model can still be used even if the energy terms are eliminatied. One needs the entropy change between the liquid at the freezing volume fraction and the crystal at the melting volume fraction. This change can be determined from computer simulations[3,26] using simple thermodynamic relationships as outlined above. This difference has a value $S_c - S_f = -1.2N_A k$, where S_c is the bulk crystal entropy, S_f is the bulk liquid entropy, N_A is the number of liquid particles transfered to the solid surface, and k is the Boltzmann constant. This change is negative indicating that the entropy of the crystal is lower than the liquid, and unfavorable, if entropy is to be maximized. The reader should not be surprised by this result because the coexisting liquid is at one volume fraction and the crystal at another. For a metastable fluid at equilibrium densities corresponding to a fully crystalline solid, the entropy of the metastable fluid is lower than the corresponding equilibrium crystal, in agreement with our understanding that entropy is maximized in equilibrium[34]. The Jackson model Helmholtz free energy, F, for crystallization at constant pressure and volume, corresponding to our crystallization conditions, is given by

$$\Delta F/NkT = 1.2\rho + \rho Ln(\rho) + (1-\rho)Ln(1-\rho). \tag{4.6}$$

In this expression $\rho = N_A/N$ is the fraction of crystal surface sites occupied. The first term on the right hand side is the bulk entropy change cited above, while the second and third terms correspond to the surface configurational entropy. A rough surface is half occupied, while a purely smooth surface is fully occupied or empty. For the bulk entropy change $(-1.2N_Ak)$ used in this theory, the minimum free energy is at an occupancy of $\rho = 0.23$. While this value indicates something between the extremes of smooth or rough, the model is crude but indicates how purely entropic "forces" can produce rough or smooth surfaces. Crystals of hard spheres may show sharp interfaces because the bulk entropy loss on adding a particle to the interface may dominate the configurational entropy gain. Clearly a better calculation would be more definitive. In the case of repulsive charged colloidal particles, we expect a larger free energy cost in adding particles to a crystal surface. Therefore, the surfaces should be rougher than that for hard spheres, as observed.

As noted for figure 4.1, a high degree of substructure is evident in the larger crystals. One might suspect that the different substructures in a single crystal are actually different crystals having different orientations but were seeded and grew from a common nucleus. However, we note from figure 4.1 that the crystals oriented to Bragg scatter, represent a single orientation and many times have dimensions comparable to the dark crystals, not the substructure length scale in the dark crystals. This suggests that the crystals have a fairly uniform stacking plane orientation, but registration differences within a plane lead to different stacking structures growing parallel to one another. The boundaries between these different stacking structures are visible as substructure boundaries. Growth instabilities, such as the Mullins-Sekerka instability discussed previously, could lead to this kind of boundary development. Unstable growth which favors the development of protrusions would maintain the layer stacking oreintation. However, there would be no communication of registration order between spatially separated protrusions.

As layers are added independently onto each of the protrusions the detailed differences in the adjacent crystals leads to a substructure boundary as the protrusions merge and grow together.

In figure 4.4 the length scales measured by small angle light scattering and photography are compared. The agreement between the two measurements is striking. Both indicate an initial increase in length scale as the crystals are nucleated and grow. The size and growth rates are comparable. However, after half an hour, the length scale begins to decrease in both measurements. For sufficiently long times, not shown here, it increases again. The decrease in size was first observed in small angle scattering[17] and was not understood. However, it is now observed photographically. The photographs indicate that the crystals grow independently from the melt and exhibit an internal substructure with a characteristic length scale before overlapping or touching at the completion of the growth phase. At this time the sample appears full of crystals. The crystals have lost their individual identity and the substructure is the dominant length scale. Crystals which Bragg scatter directly to the camera are also reduced to this substructure length scale. This reduction in Bragg scattering size means that the crystals must have broken up or dissolved along substructure boundaries and undergone some local reorientation. Theoretical calculations[28] and Bragg angle scattering measurements[35] have indicated that the growing crystals are compressed to higher than equilibrium densities during growth. When a full complement of crystals is created at the completion of growth and the metastable fluid density is reduced to nearly the equilibrium value, the compressed crystals must then be in an unstable situation in which expansion fractures them and dissolution occurs along the substructure boundaries before ripening commences.

The shape of the crystals undoubtedly is related to the underlying microscopic order. Light diffraction studies[15] reveal that this order is a registered random stacking of close packed (111) layers of particles to make highly faulted face centered cubic or hexagonal close packed crystals. We have not yet been able to index a crystal with respect to its shape, because the crystals are exceedingly

soft and destroyed by weak shear flows. However, we speculate that the stacking of (111) layers may have a rectangular shape when viewed end on and a rosette shape when viewed straight on.

Conclusions

In conclusion we remind the reader that the remarkable ordering observed during crystallization in these hard sphere systems is the result of entropy increasing in thermodynamically isolated systems.

Acknowledgements

The authors gratefully acknowledge support of this work by NASA through grant NAG3-1624.

BIBLIOGRAPHY

1. G. E. Uhlenbeck, in *The Many Mody Problem*, edited by J. K. Percus, (Wiley interscience, New York, 1963).
2. B. J. Alder, W. G. Hoover, and D. A. Young, J. Chem. Phys. **49**, 3688, (1968).
3. W. G. Hoover and F. H. Ree, J. Chem. Phys. **49**, 635, (1968).
4. M. Baus, Molecular phys. **50**, 543, (1983).
5. M. D. Eldridge, P. A. Madden, and D. Frenkel, Nature, **365**, 35, (1993).
6. H. de Hek and A. Vrij, J. Coll. Interface Sci. **84**, 409, (1981).
7. L. Antl, J. W. Goodwin, R. D. Hill, R. H. Ottewill, S. M. Owens, S. Papworth and J. W. Waters, Colloids and Surfaces **17**, 67, (1986).
8. S. E. Paulin and B. J. Ackerson, Phys. Rev. Lett. **64**, 2663 (1990).
9. R. Buscall, J. W. Goodwin, R. H. Ottewill, and Th. F. Tadros, J. Coll. Interface Sci. **85**, 78, (1982).
10. C. W. J. Beenakker and P. Mazur, Physica (Amstrdem), **126A**, 349, (1984).
11. P. N. Pusey and W. van Megen, Nature **320**, 340, (1986).
12. S. M. Underwood, J. R. Taylor, and W. van Megen, preprint (1994).
13. J. P. Hansen and D. Schiff, Physics, **25**, 1281, (1973).
14. B. J. Ackerson, J. Rheol. **34**, 553 (1990).
15. P. N. Pusey, W. van Megen, P. Bartlett, B. J. Ackerson, J. G. Rarity, and S. M. Underwood. Phys. Rev. Lett., **63**, 553, (1989).
16. K. Schätzel and B. J. Ackerson, Phys. Rev. Lett. **68**, 337 (1992).
17. K. Schätzel and B. J. Ackerson, Phys. Rev. E **48** , 3766 (1993).
18. Y. He, B. J. Ackerson, K. Schätzel, S. M. Underwood and W. van Megen, submitted for publicatio.
19. K. A. Jackson, in *Liquid metals and Solidification*, Page 174, (ASM, Cleveland, 1958).

20. K. A. Jackson, in *Progress in Solid State Chemistry*, Vol. 4, edited by H. Reiss, (PerramonPress, New York, 1967).

21. W. W. Mullins and R. F. Sekerka, J. Appl. Phys. **34**, 323, (1963).

22. W. W. Mullins and R. F. Sekerka, J. Appl. Phys. **35**, 444, (1964).

23. D. W. Marr and A. P. Gast, Phys. Rev. E **47**, 1212 (1993).

24. D. J. W. Aastuen, N. A. Clark, L. K. Cotter, and B. J. Ackerson, Phys. Rev. Lett. **57**, 1733 (1986); **57**, 2772 (1986).

25. J. S. Langer, Rev. Mod. phys. **52**, 1, (1980).

26. L. V. Woodcock, Ann. N. Y. Acad. Sci., **37**, 274, (1981).

27. K. R. Hall, J. Chem. Phys. **57**, 2252, (1972).

28. B. J. Ackerson and K. Schätzel, Phys. Rev. E **52**, 6448, (1995).

29. J. S. van Duijneveldt and H. N. W. Lekkerkerker, in *Science and Technology of Crystal Growth*, edited by J. P. Erde and O. S. L. Bruinsma (Kluwer Academic, Dordrecht, 1995).

30. D. W. Marr and A. P. Gast, Phys. Rev. E **47**, 1212 (1993).

31. W. B. Russel, Phase Transitions **21**, 127 (1990).

32. J. D. Weeks and G. H. Gilmer, in *Advances in Chemical Physics*, **40**, 157, (1979).

33. J. D. Weeks, in *Ordering in Strongly Fluctuating Condensed Matter Systems*, edited by T. Riste, (Plenum Press, New York, 1980).

34. B. J. Ackerson, Nature, **365**, 11, (1993).

35. J. L. Harland, S. I. Henderson, S. M. Underwood and W. van Megen, Phys. Rev. Lett. **75**, 3572, (1995).

CHAPTER V

CRYSTALLIZATION IN SUSPENSIONS OF HARD SPHERES AND TURBIDITY

Abstract

The dynamics of crystallization have been investigated for suspensions of hard spheres by small angle light scattering, direct imaging, and Bragg scattering. This work reports preliminary but complementary measurements of turbidity during crystallization. The change in turbidity correlates with small angle light scattering for the smaller volume fractions studied, where the signal is strong. However an initial exponential time dependence in turbidity is observed, which has a decay time independent of the sample volume fraction. This signal dominates at larger volume fractions where small angle light scattering measurements are weak and Bragg studies are more easily performed. We identify this initial transient decay with a laser induced heating of the sample.*

Introduction

Uniformly sized colloidal particles, which are stabilized against irreversible aggregation, will spontaneously order into regular crystalline arrays at sufficiently large particle concentration [1]. In these suspensions the interparticle separation is on the order of the wavelength of visible light, and the crystallization process is slow (on the order of seconds to days), making them amenable to study by a variety of experimental techniques from direct observation [2], Bragg angle scattering[3,4], small angle scattering[5,6] and turbidity measurements[7].

*will be published (accepted by Physica A) by: Yueming He and Bruce J. Ackerson; Department of Physics and Center for Laser Research; Oklahoma State University; Stillwater, OK 74078-0444

Recently sterically stabilized "hard sphere" suspensions have been investigated by both small angle scattering [8,5,6], direct imaging[9] and Bragg angle scattering[4]. The small angle scattering revealed different time domains referred to as nucleation/growth (see figure 5.2 for times less than 2000s), crossover (figure 5.2 between 2000s and 100000s) and ripening (figure 5.2 for times greater than 100000s). In the nucleation/growth and ripening regions the scattered intensity distributions are found to scale, such that the scattered intensity maximum amplitude, I, and position, $q_{\frac{1}{2}}$, are sufficient to describe the scattered intensity completely, given the intensity distribution at one time. In the crossover region, the intensity distribution does not scale and evolves in time. For samples with $0.22\mu m$ particle radii, the intensity distribution in the three different time domains was fit to a Furukawa form and found to broaden systematically as the sample volume fraction increased. This is attributed to an increase in colloidal crystal polydispersity with increasing volume fraction[6].

For samples with $0.50\mu m$ particle radii in the liquid-crystal coexistence region, the time evolution of $q_{\frac{1}{2}} \sim t^{-1/2}$ in the nucleation/growth region indicates a diffusion limited growth process, contrary to earlier observed or assumed interface limited growth processes where $q_{\frac{1}{2}} \sim t^{-1}$ [2,3]. For samples with $0.22\mu m$ particle radii in the liquid-crystal coexistence region, the time evolution is described by $q_{\frac{1}{2}} \sim t^{-\alpha}$ with $\alpha \sim 0.75$ to 1.0. These discrepancies were investigated in a model calculation for the growth of hard sphere crystals [10]. This model, based on the Wilson-Frenkel growth law and computer simulation results for hard sphere thermodynamic functions, shows both diffusion limited growth in the coexistence region and interface limited growth for volume fractions greater than the melting value, if the particle incorporation rate into the crystal is large. For reduced incorporation rates, quasi-power law behavior is observed with exponents $0.5 < \alpha < 1.0$ in long lived transients to the final asymptotic diffusion limited or interface limited forms. The observed crystal growth rates indicate that our experimental observations occur within these transients. The model also indicates that the nucleated crystal initially will be compressed to densities larger than the equilibrium value

but undergo a slow relaxation to the equilibrium value. Bragg angle studies indicate such a compression and relaxation[4], but quantitative comparisons are yet to be done.

Nucleation rate densities, $N \sim 1/(4\pi R^3 T_c/3)$, may be estimated from the crystal size $R \sim 1/q_{\frac{1}{2}}$ at the crossover time T_c when the sample is assumed to have its full complement of crystal. If a reduced nucleation rate density is calculated to account for differences in sample particle size, it is found that the $0.22\mu m$ particle radii samples have a reduced nucleation rate density at least two orders of magnitude smaller than the $0.50\mu m$ particle radii samples at the same volume fraction[6]. It has been suggested that the smaller particles might have a softer interparticle repulsion than the larger particles. But the conventional wisdom is that this softer repulsion should lead to a larger nucleation rate density. We have attributed this difference to sample polydispersity which is ~ 0.07 and ~ 0.05 for the smaller and larger particles, respectively. The reduced growth velocities (particle incoporation rates) are the same for both large and small particle samples, however. Finally we note that the nucleation rate density may be calculated from classical nucleation theory[10]. As the freezing point is approached the variation with volume fraction is dominated by thermodynamics. Since the thermodynamics of hard spheres is established, it is troublesome that the experimentally measured values show a much weaker volume fraction dependence than the classical prediction.

Direct observations of hard sphere colloidal crystals have been made at the first order Bragg angle for volume fractions near 0.52[9]. Both bright crystals (oriented to Bragg scatter) and dark crystals (improperly oriented to Bragg scatter) are observed. The dark crystals evidence sharp edges, which indicate faceted rather than rough surfaces. Simple arguments have been given by Jackson to estimate the roughening transition[11]. These arguemts have been adapted to the purely entropic hard sphere liquid- crystal transition to understand observations. The dark crystals also evidence an internal structure, which is indicated in the small angle scattering results, as well[6]. Direct observations do not indicate that this structure results from an aggregation of smaller crystals into a single larger

crystal. However, the length scale of this substructure compares favorably with numerical estimates of the Mullins-Sekerka instability length for these samples[12]. The reduction in crystal sized in the crossover region (increase in $q_{\frac{1}{2}}$) is attributed to the breakdown of crystals to this substructure length scale.

In the small angle and Bragg scattering experiments reviewed above there are initial transients observed which complicate data analysis. These transients are assumed to be related to the shear melting process and subsequent viscous damping of fluid motion in the sample. However, effects related to sample absorption have been ignored. For some samples, measurements of transmitted intensity indicate that nearly half the light is scattered or absorbed[5]. Such a loss due only to scattering would indicate significant multiple scattering. However, the samples appear clear, so multiple scattering was considered minimal. Furthermore, small angle scattering measurements have been performed with a helium neon (633nm) laser, because illumination with shorter wavelengths (488nm) produced noticable thermal blooming. In this paper we present preliminary results for turbidity measurements which complement earlier small angle and Bragg angle studies. The turbidity measurements show an initial transient which is not related to the crystallization process. We argue that it is due to heating by the incident laser beam. The time scale for this decay sets the lower time limit for which reliable scattering data may be obtained. For larger times the turbidity may be explained in terms of scattering by the growing crystals.

Theory

Turbidity is defined as the light intensity reduction per unit penetration length in the sample. For a finite sample thickness d, the turbidity is given as

$$\tau = \frac{1}{d} ln(\frac{I_o}{I_d}) \tag{5.1}$$

where I_0 is the light intensity incident on the sample and I_d is the intensity exiting through the sample. The reduction in intensity is produced by absorption or scattering of the incident radiation. However, the samples examined in this study

are index matched to reduce multiple scattering and appear transparent. The transmitted intensity, $I_d(t)$, is monitored as a function of elapsed time since shear melting and would appear to be a result of the structural reorganization of the particles during the crystallization process.

If the turbidity change is due only to scattering, then the turbidity may be related to the total scattered intensity, $i(\theta)$, by the metastable fluid, small angle and Bragg sources as

$$\tau = 2\pi \int_0^\pi i(\theta) sin\theta d\theta. \tag{5.2}$$

Although the relative magnitudes of the metastable fluid, small angle and Bragg scatterings are not known, the angular dependencies have been measured. For the metastable fluid, the Percus-Yevick structure factor has been used to fit data, and the integrated intensity has been measured for Bragg angle scattering[4]. For small angle measurements[6], the measured intensity is found to evolve as

$$i(\theta) = I(t)S(\theta, t) \tag{5.3}$$

where $I \sim t^{6\alpha+1}$, $S(\theta, t)$ is a normalized structure factor and α is the growth exponent for the length scale measured in small angle scattering, $R \sim 1/q_{\frac{1}{2}} \sim t^{\alpha}$. The Furukawa form[13] for the structure factor

$$S(\theta, t) = \frac{(1 + \gamma/2)Q^2}{(1 + \gamma/2) + Q^{2+\gamma})} \tag{5.4}$$

has been used most recently to fit small angle scattering data[6]. Here $Q = q/q_{\frac{1}{2}}$ with $q = 4\pi n sin(\frac{\theta}{2})/\lambda$, where n is the solvent index of refraction, θ is the scattering angle, and λ is the incident radiation vacuum wavelength.

Experimental Procedure

The sample used in these experiments is comprized of $0.22\mu m$ radius polymethylmethacrylate (PMMA) spheres suspended in a mixture of tetralin and decalin. The solvent ratio is chosen to match the refractive index of the particles

and render the suspensions transparent. The particles are sterically stabilized against aggregation with an $\sim 10nm$ thick surface layer of hydroxystearic acid. The volume fraction of particles in each sample is determined by the weight ratio of solid to solvent but scaled to the freezing volume fraction as described elsewhere[14]. Two samples in this study ($\phi = 0.525, 0.538$) were between the freezing value ($\phi_{freezing} = 0.494$) and the melting value ($\phi_{melting} = 0.545$), and two samples ($\phi = 0.554, 0.563$) were above the melting value but less than the kinetic glass transition value.

A schematic diagram of the apparatus used in these experiments is detailed in figure 5.1. This apparatus is adapted from earlier small angle scattering studies[5,6]. A polarized helium neon laser beam is expanded, spatially filtered by a pinhole, and weakly focussed to a distant screen used for small angle scattering. The beam width at the sample is slightly less than the width of the sample container to avoid spurious reflections and small angle scatter. One diode detector monitors the input beam intensity and another, behind the small angle scattering detection screen, monitors the transmitted intensity or transparency of the sample. The output of these diodes is digitized and recorded by a personal computer.

Samples are prepared for measurement by shear melting[15] which is assumed to leave the sample in a metastable fluid or amorphous state. After complete shear melting by agitation and tumbling for several days, the sample is mounted on the measuring apparatus. The sample holder is driven by a stepping motor, which shear melts the sample by turning it end over end once a minute for several minutes, before repositing the sample cell precisely to the initial orientation for the next measurment. This allows signal averaging, especially at the larger volume fractions where the signal is weaker and a few hundred crystallization runs are averaged.

Figure 5.2 shows turbidity data determined from intensity data using equation (5.1). Intensity data is normalized for incident laser fluctuations and further normalized by the initial transmitted intensity value, $I_d(t = 0)$, for presentation here. The volume fractions in the coexistence region show the turbidity

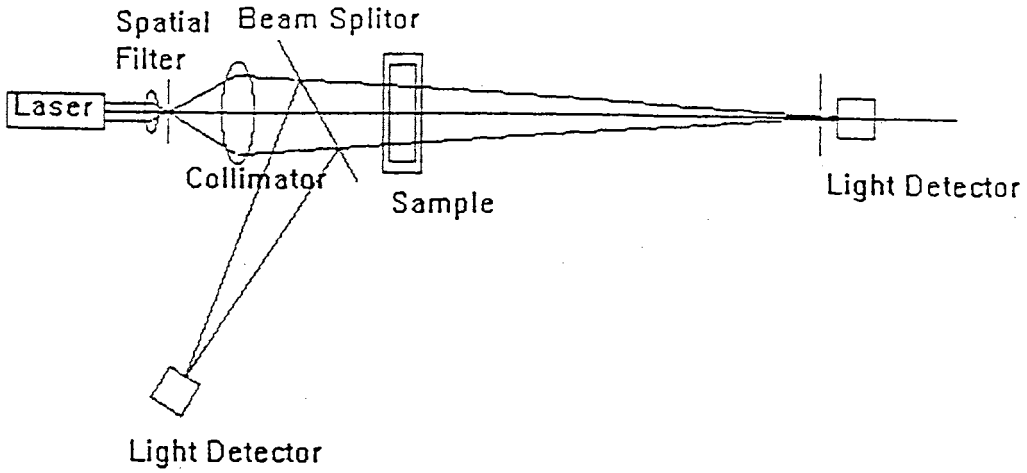

Figure 5.1. Schematic diagram of the apparatus used in both small angle and turbidity measurements showing spatially filtered, expanded laser beam which is weakly focussed through the sample to the small angle scattering screen and collected by a photodiode. A second photodiode monitors the magnitude of incident laser beam.

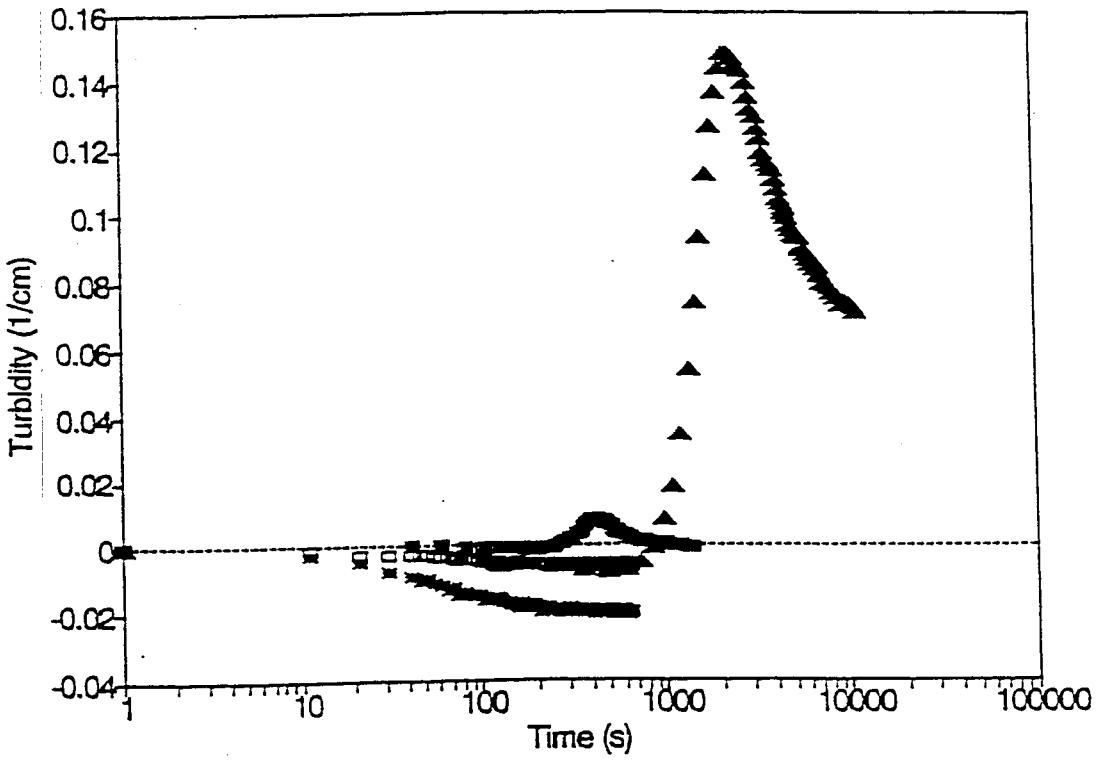

Figure 5.2. Turbidity measurements for volume fractions ($\phi = 0.563$ open squares, $\phi = 0.554$ asterisks, $\phi = 0.538$ filled squares, and $\phi = 0.525$ filled triangles).

to decrease initially but this is followed by an increase to a maximum value at a time identified as the crossover value in earlier work[6], where the the initial nucleation and growth process ends and ripening begins. The turbidity decreases for larger times. For volume fractions greater than the melting value, the turbidity only decreases for the times measured; however, these times also should include the crossover region (at least for $\phi = 0.554$).

Discussion

Turbidity measurements at the smallest volume fraction measured mirror the same change in intensity and suggest a strong dependence on the small angle scattering. The small angle scattered intensity, $I(t)$, increases at early times during nucleation and growth as shown in figure 5.3. At the beginning of the crossover region this intensity decreases but is followed by an increase in value in the ripening region. By contrast, Bragg scattering[4] exhibits an increase in intensity in the nucleation and growth region which saturates without decreasing in magnitude for times greater than the crossover value. Photographic studies[9] suggest that crystals break up into smaller pieces at the beginning of the crossover. Thus the small angle scattering increases due to nucleating and growing crystals but decreases at the crossover due to the decreased size of crystallites. Since the total volume of crystallites need not decrease as the crystals fracture, the Bragg scattered intensity will saturate.

Figure 5.4 shows turbidity data for $\phi = 0.525$ compared against turbidity calculated using equations (5.1), (5.2) and (5.3) with $\gamma = 4$, and experimentally measured small angle values for $I(t)$ and $q_{\frac{1}{2}}(t)$. The amplitude of the calculated turbidity is scaled to fit the amplitude of the direct turbidity measurements. This calculation neglects increasing contributions from Bragg angle scattering and decreasing contributions from the metastable fluid, but fits the data well. It does not fit the initial decrease in turbidity nor does it do well beyond the maximum at the crossover time. However, beyond the crossover time the static structure factor

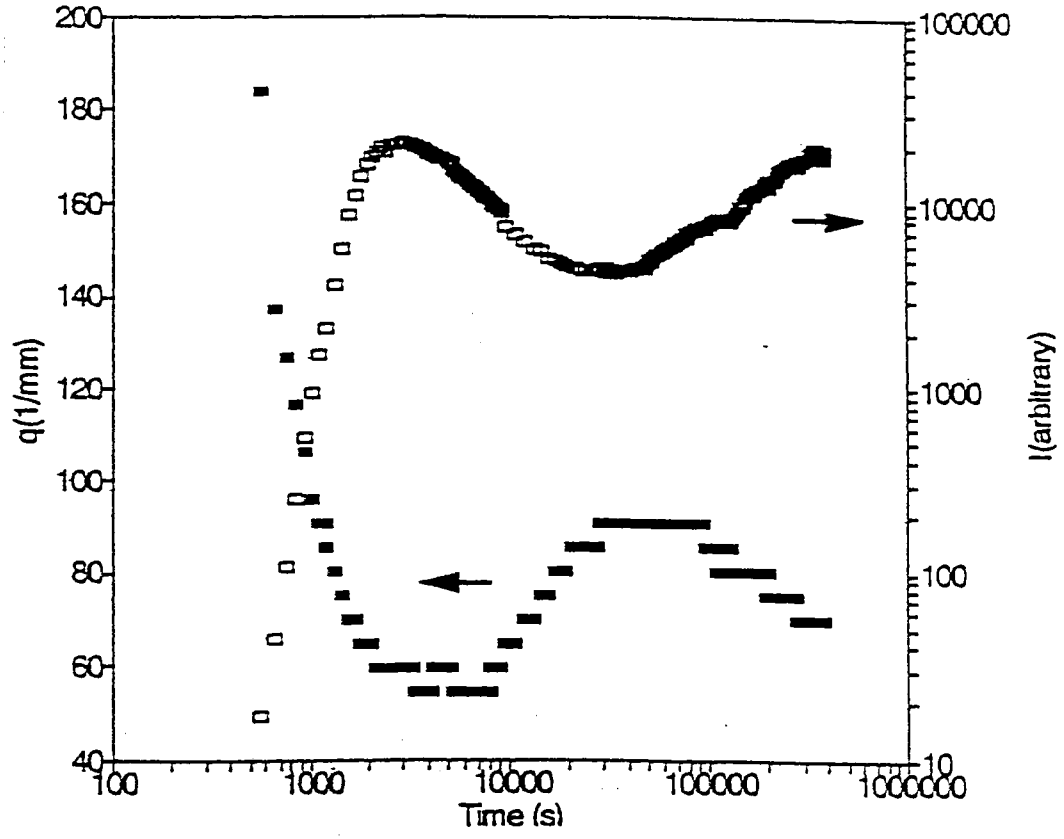

Figure 5.3. Small angle light scattering measurements of the reciprocal length scale, $q_{\frac{1}{2}}$, and the maximum intensity, I, as a function of elapsed time for sample $\phi = 0.525$.

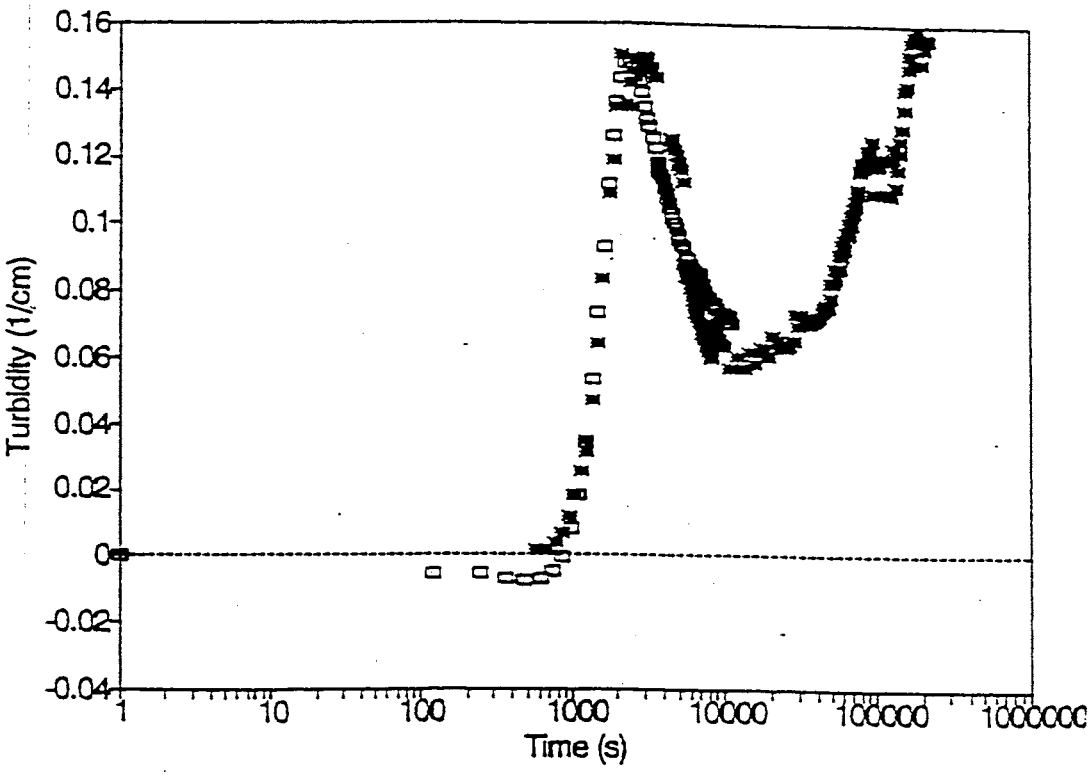

Figure 5.4. Turbidity for sample $\phi = 0.525$ as a function of time compared to theory which includes only the small angle scattering to account for changes in the transmitted intensity.

form (equation (5.4)) changes[6] and will influence the fit in the appropriate direction. Clearly the small angle scattering dominates the turbidity at small volume fractions.

The initial time decay observed in the turbidity data indicates a decrease in turbidity or clarification of the sample. This trend has been observed by Aastuen et al.[7] and was related to the decreased scattering produced by crystals relative to the metastable fluid. These measurements did not rigorously exclude the small angle scattering from measurements of the transmitted intensity as done in the results presented here. However, one may expect such an effect as follows. The metastable fluid scattering will be reduced in proportion to the volume of fluid replaced by crystal. But the crystal scattering may have a dependence on the average crystal radius greater than a power of three. If the crystals do not significantly attenuate the radiation incident upon them[16], then the maximum scattered intensity of the Bragg peak is proportional to the square of the number of scatterers in the crystal or the square of the volume of the crystal. However the integrated intensity is measured and this decreases the power dependence on average crystal radius to a power of four. Thus, for small crystal radii, the loss of scattering from the metastable fluid may be greater than the scattering by the crystal for sufficiently small crystal radii. The same power law dependence holds true for the small angle scattering and is reflected in the theoretical form presented in equation (5.2). However, this reasoning does not explain the initial time dependence observed in our experiments.

Figure 5.5 shows the turbidity data for the $\phi = 0.525, 0.554$, and 0.563 volume fraction samples fitted by a single exponential function with decay time, $T = 65s$. Note that the 0.563 sample signal amplitude was scaled to superimpose on the other sample data. There is an initial decay in the turbidity which is independent of volume fraction, which suggests that it is not a result of the crystallization process. Both small angle and Bragg angle measurements show an enormous change in time scale with volume fraction, with the smaller volume fraction samples evidencing these crystallization effects only at much larger times

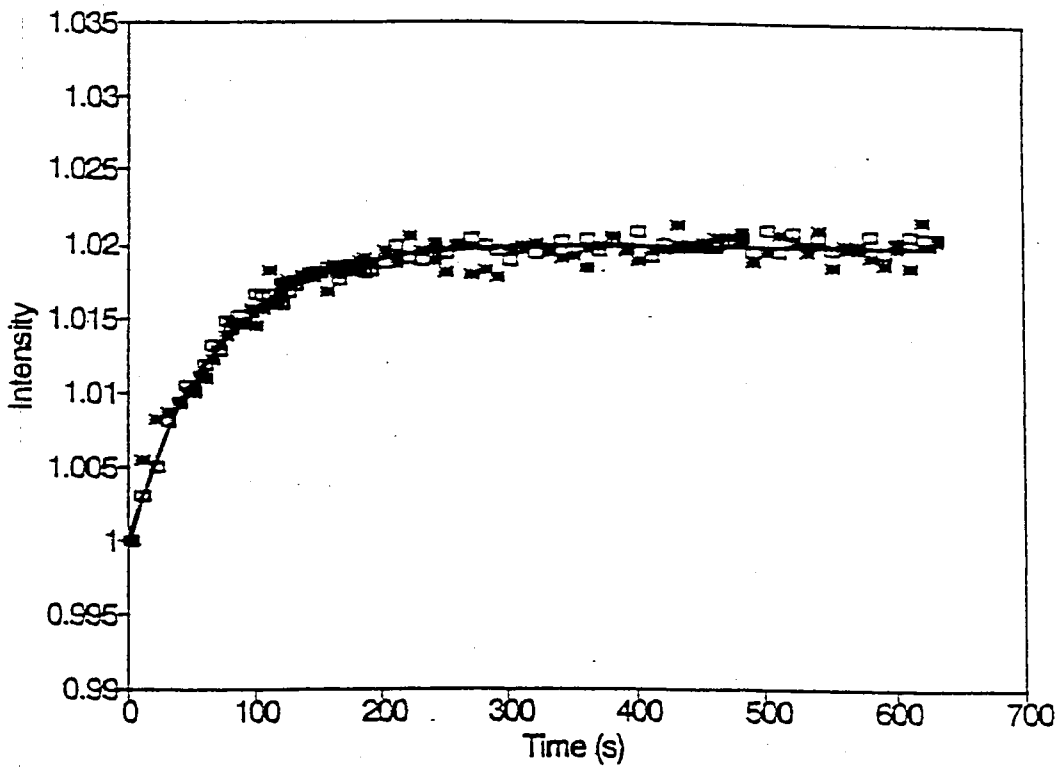

Figure 5.5. Turbidity for samples $\phi = 0.525, 0.554, 0.563$ and a single exponential decay (solid line) described in the text.

after shear melting. Relaxation associated with the shear melting process can also be ruled out because the sample viscosity increases dramatically with increasing volume fraction. One would expect that a turbidity change associated with this relaxation would be reflected as an increased decay time, T, with increased volume fraction and viscosity. The possibility of slow electronic settling times was ruled out by taking data while replacing the sample with an attenuator and finding no effect. However, a noncrystallizing sample with volume fraction less than the freezing value did evidence this decay.

While the samples are transparent, they do have a yellow appearance, indicating partial absorption of incident radiation. This may result from a reaction of decalin with water or other slow chemical degradation process. While absorption has been ignored in the analysis of previous experiments, we now wish to examine this as an explanation for the initial change in turbidity. Earlier work reported transmitted intensities not less than 50% of the incident intensity. The present samples also show similar reductions in intensity, but no samples appeared to be multiply scattering. In fact, the turbidity changes shown in figure 5.2 evidence only changes of order ten percent or less due to changes in absorption and scattering.

We argue that the initial change in turbidity is related to absorption. The absorbed radiation increases the sample temperature, changing the index of refraction. As a result, there is a shift in contrast between particle and solvent, which changes the scattering and consequently the turbidity. The incident radiation, which illuminates the sample uniformly, will produce a temperature difference between the sample and the cell walls held at fixed temperature. A time constant may be found for the build up of this temperature difference by solving a diffusion equation for the temperature distribution in the cell. The slowest mode decays exponentially with a decay time given by $T = \pi^2/(L^2\kappa)$. The thermal diffusion constant is given by $\kappa = k/\rho C$, where $k(\sim 0.0005 cal/cmsK)$ is the thermal conductivity, $\rho(= 0.8699 gm/cm^3)$ is the density and $C(\sim 0.3 cal/gmK)$ is the heat capacity of the solvent. Representative values are given for the conductivity and

specific heat, while the known value for the density of decalin is given in parentheses. The sample cell width is given by $L(= 1cm)$. These values give a decay time, $T = 55s$, in good agreement with our observations. If 50% of the $30mW$ maximum possible incident laser radiation, Q, is absorbed by the sample, then the temperature rise may be estimated as $\Delta \sim QT/\rho C$. For the values given above, this corresponds to a temperature rise on the order of one degree centigrade and a change in the index of refraction on the order of $\Delta n \sim 0.0004$. This could easily account for the observed initial few per cent change of the turbidity, since the samples are adjusted to be index matched.

In Bragg angle studies, the low order Bragg scattering grows on the metastable fluid structure factor and must be determine by a background subtraction process[4]. This subtraction is complicated by the observed loss in intensity of the fluid scattering. This intensity loss does not seem to be related to the total amount of fluid present, and our observed temperature dependence suggests an alternative way to model the scattered intensity loss.

In conclusion, we find the measured turbidity during crystallization in suspensions of hard spheres to be dominated by small angle scattering losses and to laser heating induced changes in particle solvent contrast. The time scale for these latter changes should not pose a problem in the previously measured small angle light scattering or Bragg angle measurements, except near the melting point where the nucleation/growth time scales and temperature relaxation time scales begin to overlap. If this is the case, then sample sizes can be reduced to reduce the temperature relaxation time scale. Absorption explains both the large loss of transmitted intensity without multiple scattering and the initial dynamics of the turbidity measurements.

Acknowledgements

The authors gratefully acknowledge support of this work through grant numbered DMR 9501865 from the National Science Foundation. The authors also thank W. van Megen and S. M. Underwood for the samples used in this experiment.

BIBLIOGRAPHY

1. P. N. Pusey, in *Liquids, Freezing and the Glass Transition*, edited by D. Levesque, J. P. Hansen, and J. Zinn-Justin (Elsevier, Amsterdam, 1990).

2. D. J. W. Aastuen, N. A. Clark, L. K. Cotter, and B. J. Ackerson, Phys. Rev. Lett. **57**, 1733 (1986); **57**, 2772 (1986).

3. J. K. G. Dhont, C. Smits, and H. N. W. Lekkerkerker, J. Coll. Int. Sci., **152**, 386 (1992).

4. J. L. Harland, S. I. Henderson, S. M. Underwood and W. van Megen, Phys. Rev. Lett. **75**, 3572, (1995).

5. K. Schätzel and B. J. Ackerson, Phys. Rev. E **48** , 3766 (1993).

6. Y. He, B. J. Ackerson, K. Schatzel, S. Underwood, and W. van Megen, submitted for publication.

7. D. J. W. Aastuen, N. A. Clark, J. C. Swindal, and C. D. Muzny, Phase Transitions **21**, 139 (1990).

8. K. Schätzel and B. J. Ackerson, Phys. Rev. Lett. **68** , 337 (1992).

9. Y. He, B. J. Ackerson and B. Olivier, submitted for publication.

10. B. J. Ackerson and K. Schätzel, Phys. Rev. E **52**, 6448 (1995).

11. K. A. Jackson, *Liquid Metal and Solidification* (ASM, Cleveland, 1958) p. 174.

12. W. W. Mullins and R. F. Sekerka, J. Appl. Phys. **34**, 323 (1963).

13. H. Furukawa, Physica A **123**, 497 (1984).

14. P. N. Pusey and W. van Megen, Nature (London), **320**, 340 (1986).

15. B. J. Ackerson and N. A. Clark, Phys. Rev. Lett. **46**, 123 (1981).

16. R. W. James, *The Optical Principles of the Diffraction of X-Rays*, **Vol. II**, edited by L. Bragg (G. Bell and Sons LTD, London, 1948).

CHAPTER VI

SUMMARY AND CONCLUSIONS

The phase transition of freezing of a liquid or melting of a solid is an old subject in physics. It is very important to today's science and engineering and has many applications. But today, people still have little knowledge about the phase transition from the microscopic kinetics theories aspect. More experimental data in freezing or melting are needed. One of the difficulties in the experimental research is that the dynamics of the nucleation and growth for pure atomic systems is too fast to monitor with usual equipment. Hard sphere colloidal systems give us an opportunity to study the phase transition with their relative slow crystallization processing and large interparticle distance of the crystals. This work presents three experimental methods to measure the dynamics of crystallization of a hard sphere colloidal system. The small angle light scattering technique developed by Schätzel and Ackerson was used to measure the nucleation and growth of the crystals for small size hard sphere particle system, which enable us to study the phase transition with less gravitational influence. More data with different volume fraction samples were taken than previously measured. The data support the previous work of Schätzel and Ackerson. All the data show that there are three growth regions. The crystals exhibited a power growth law instead of a linear growth in small and late time regions. In "crossover" time region, the characteristic length, $q_{1/2}$, is observed to decrease, which means crystals breakup or dissolve before ripening begins. The normalized structure factors have been fit by a functional form given by Furukawa. The scaling of the intensity versus angle data is different in different growth time regions and depends on the volume fraction. For small volume fraction samples, a complex large wavevector decay behavior was observed. It may suggest that there are substructures inside a crystal.

Turbidity measurements were applied to monitor the crystallization process. Turbidity data showed the dynamics of the crystal growth which agreed with the small angle light scattering measurements. Turbidity data evidenced a thermal blooming due to laser heating.

A special photographic technique was used to monitor the crystal growth in real space domain. Individual crystal growth was measured and the crystal morphology was observed. Substructures inside the crystals and the instabilities of the crystals were observed. All the real space measurements of the crystals support the small angle light scattering measured results.

Questions for future research include the following: For small angle light scattering measurement, we may improve the signal to noise ratio for high volume fraction samples by using more sensitive diode array as the light intensity detector. Various samples may be used in the experiment to study the effects of the polydispersity and "solfness" of particles in the crystallization process.

For photographic technique, a computer related digital image processing technique is needed to be developed to analyze the crystal images. Statistical data, such as size distribution, number density and size of the crystals as a function of time can be obtained easily with the help of this technique. My colleague in the laboratory Keith Davis is developing this kind of technique.

APPENDICES

APPENDIX A

CLASSICAL NUCLEATION AND GROWTH THEORY OF HARD SPHERE CRYSTALS

Microscopic theories for nucleation and growth based on statistical mechanics are still undeveloped. The classical theory is still often used to interpret data through kinetic coefficients may be order of magnitude off in fits to data. Russel [1] and Ackerson[2] developed a theory model for nucleation and growth of the hard sphere crystals based on the classical theories. This chapter gives a brief review of Ackerson's works.

Diffusion of the particles

Nucleation and growth of the colloidal crystals is due to the diffusion of the particles through one phase (liquid) into other phase (solid). We can distinguish two kinds of diffusion from their driving mechanism. One is called collective diffusion and the other called self diffusion.

The collective diffusion with collective diffusion coefficient, D_c, is caused by the concentration gradients of the particles suspended in the solvent. For hard sphere colloidal system, collective diffusion coefficient in fluid, D_c^f, is almost independent of volume fraction for small density gradients [3–5], and no experimental data of collective diffusion coefficient in solid, D_c^s has been measured. According to the classical crystal growth model , when the crystal grows, the particles diffuse to the surface of the crystal and then are incorporated into the crystal. As a result, a depletion zone will be produced round the crystal in the liquid. The equations of the collective diffusion of the particles for solid and liquid phase are

$$\frac{\partial \phi_f}{\partial t} = \nabla \cdot D_c^f(\phi_f) \nabla \phi_f \tag{A.1}$$

$$\frac{\partial \phi_s}{\partial t} = \nabla \cdot D_c^f(\phi_s) \nabla \phi_s \tag{A.2}$$

Where the f and s subscripts refer to the fluid and crystal, respectively.

In the hard sphere colloidal system, the random or diffusion motion of particles is Brownian due to random kicks with the molecules of the solvent. The self diffusion coefficient, D_s, describes the motion of a tagged particle in the suspension.. It is defined as $D_s =< \Delta r^2(t) > /6t$. The mean square displacement of the particles, $< \Delta r^2(t) >$, can be measured with photon correlation spectroscopy[6]. Experimental data and theoretical results from computer simulations[7,8] show that there are two different self diffusions associated with different time scales. One is the rapid diffusion within the "cage" of neraest neighbour and the other is the slower diffusion beyond their cage. Thus diffusion coefficients are function of sample concentration. In short-time, times much less then the time which is the needs for a particle to diffuse the mean interparticle separation, a particle does not interact with other particles. Only hydrodynamic interaction affects the particle diffusion by reducing the particle mobility. a measured short-time diffusion coefficient, D_s^0, as a function of volume fraction in dilute limit, $\phi_f \rightarrow 0$, is given as [9]

$$\frac{D_s^0}{D_0} = 1 - 1.83\phi_f, \tag{A.3}$$

and $D_s^0 \rightarrow 0$ as $\phi_f \rightarrow 0.64$ at random close packing. Here $D_0 = \frac{k_b T}{\pi \eta a}$ is Stokes-Einstein value, where a is the particle radius, T is the temperature and η is the viscosity of the solvent (D_0 has a value $0.41 \mu m^2/sec$ for the samples used in this work). At long times, a particle interacts with the surrounding solvent as well as other particles and then the particle diffusion involves both of hydrodynamic and structural effects. An additional retardation reduced by the structural effects leads to the long-time diffusion coefficient, D_s^∞, a dilute limit as

$$\frac{D_s^\infty}{D_0} = 1 - 1.21\phi_f, \tag{A.4}$$

and $D_s^\infty \rightarrow 0$ as $\phi_f \rightarrow 0.58$ at the glass transition where self diffusion is suppressed. For the liquid to solid phase transition, which relates to the particles movement on

the order of mean interparticle separation, the time scale is intermediate and then the corresponding diffusion coefficient is not clear. Several papers gave different expressions. Russel[1] has given the approximations for the sort-time and long-time diffusion coefficients as

$$\frac{D_s^0}{D_0} = (1 - \phi_f/3.7)(1 - \phi_f/0.64) \tag{A.5}$$

and

$$\frac{D_s^\infty}{D_0} = (1 - \phi_f/2.7)(1 - \phi_f/0.58) \tag{A.6}$$

which satisfy the limiting behavior discussed above. van Duijneveldt et al. gave different formula for the long time self diffusion by fitting the data measured on samples for volume fraction less than the freezing value, ϕ_f, as[10]

$$\frac{D_s^\infty}{D_0} = (1 - \phi_f/0.58)^{1.74} \tag{A.7}$$

and Harland et al. gave another expression as[11]

$$\frac{D_s^\infty}{D_0} = (1 - \phi_f/0.58)^{2.58}, \tag{A.8}$$

which is based on the slow structure relaxation rates for metastable colloidal fluids of hard spheres[12].

Nucleation

The Brownian motion of the colloidal particles causes at times the formation of very small solid particles or nuclei. Once the size of a nucleus is larger than a certain critical size, r^*, the nucleus can grow, leading to a phase transition in the system. In 1946, Frenkel gave the basic classical theory of homogeneous nucleation in his book[13]. When the nuclei are formed, the excess Gibbs free energy of a nucleus with radius r can be expressed as two terms contributed from surface and body energies respectively

$$\Delta G(r) = 4\pi r^2\gamma + \Delta\mu\phi_s(r/a)^3, \tag{A.9}$$

where γ is the surface tension averaged over all the possible orientation of the solid fluid interface. The density functional calculation of Marr and Gast[14] gave

$\gamma = 0.16kT/a^2$ for hard sphere system at equilibrum. Ackerson used this value in his calculation in the nonequilibrum growth process. kT is the thermal energy, a is the hard sphere radius, ϕ_s is the volume fraction of solid, and $\Delta\mu = \mu_s - \mu_f$ is chemical potential difference between the crystal and metastable liquid.

The excess Gibbs free energy, $\Delta G(r)$, first increases to its maximum, ΔG_m, then decreases as the size of the nucleus increases. Therefore, ΔG_m which is an enougy causing to nucleation determines the critical size, r^*. The Gibbsfree energy becomes the driving force for the nucleus growth when its size $r > r^*$. $d\Delta G(r)/dr = 0$ gives us r^* as

$$(r^*/a) = 8\pi\gamma a^2/(3\phi_f^3\Delta\mu) \tag{A.10}$$

and the maximum excess Gibbs free energy, ΔG_m, is

$$\Delta G_m = (4\pi\gamma a^2/3)(r^*/a)^2. \tag{A.11}$$

Following Russel, the equilibrium rate of nucleation, N, can be expressed as[1]

$$N = A(D_s(\phi_f)/a^5)\phi_f^{5/3} exp(-\Delta G_m/kT), \tag{A.12}$$

where D_s assumed to be the self diffusion constant in the metastable fluid state discussed above, factor A is unknown, but is dimensionless and presumably of order unity.

For hard sphere system, the chemical potential, μ, (in units of kT) is the function of volume fraction only. It can be calculated from the Helmholtz free energy

$$H/kT = \int Z(\phi)(d\phi/\phi) + c \tag{A.13}$$

and has the form as[2]

$$\mu/kT = \int Z(\phi)(d\phi/\phi) + Z(\phi) + c. \tag{A.14}$$

Here $Z(\phi) = \Pi/nkT$ is a function of osmotic pressure, Π, and particle number density n. The hard sphere state equations in metastable fluid and solid states can be used to find the explicit expression of the chemical potential as a function

of volume fraction. By fitting the data produced by the computer simulation of Woodcock[15] for hard sphere metastable phase, a simple expression of the state equation was given as

$$\Pi/nkT = Z(\phi_f) = 0.904/((\phi_f - 0.731)^2) + 0.016. \tag{A.15}$$

The equation of state for face-centered cubic crystal solid phase was given by computer simulation of Hall[16] as

$$\Pi/nkT = Z(\phi_f) = 2.17/(0.738 - \phi_s). \tag{A.16}$$

By enforcing the pressures of both fluid and solid to be equal in coexistent region and setting the freezing point, $\phi_{freezing}$, as 0.494, the melting point is $\phi_{melting} = 0.546$, which is essentially the same as the result in computer simulation[17].

Substituting Eqs. (A.15) and (A.16) into Eq. (A.14) and setting the chemical potentials and pressures of fluid and solid to be equal at the phase transition to determine the constant, c, gives

$$\begin{aligned} \Delta\mu/kT \;=\; & -11.137 - 0.904/(0.551 - 1.46\phi_f + \phi_f^2) - \\ & 1.643ln[\phi_f] + 0.821ln[0.551 - 1.462\phi_f + \phi_f^2] - \\ & 9.492arctan[7.91(\phi_f - 0.731)] + 2.17/(0.738 - \phi_s) - \\ & 2.904ln[0.738 - \phi_s] + 2.94ln[\phi_s]. \end{aligned} \tag{A.17}$$

Explicit expression for the rate of nucleation, N, as a function of volume fraction is obtained by substituting Eq. (A.18) into Eq. (A.12). This result is used to compare with the experimental data from SALA (small angle light scattering).

Growth

In order to simplify the theory, we only consider the growth. of a spherical crystal For a finite crystal size, r, the surface tension should effect the growth of the crystal. The "Gibbs-Thomson" effect[18] is included in the pressure balance

equation at the solid and fluid interface as

$$\Pi(\phi_s) = \Pi(\phi_f) + 2\gamma/r. \tag{A.18}$$

The classical Wilson-Frenkel growth law governs the crystal growth as follows[13,19].

$$dr/dt = \alpha(D_s(\phi_f)/2a)[1 - exp(\Delta\mu/kT)] \tag{A.19}$$

where α is unknown and assumed to be of order unity. For these equations, once the size of the nucleus larger than the critical size, r^*, the crystal will grow by addition of individual particles from the fluid phase, but will shrink for smaller number. Combining Eqs. (A.18) and (A.19) with the diffusion equations (A.1) and (A.2) in fluid and solid phase respectively, we have the equations for the classical growth model. With the approximation which self diffusion constant, $D_s(\phi_f)$, is assumed to be a constant, the equation of the model are expressed in the dimensionless form as

$$\phi_s Z(\phi_s) = \phi_f Z(\phi_f) + 4\pi K/3X. \tag{A.20}$$

$$dX/dt = \delta[1 - exp(\Delta\mu/kT)] \tag{A.21}$$

$$\frac{\partial\phi_f}{\partial\tau} = \nabla'^2\phi_f \tag{A.22}$$

$$\frac{\partial\phi_s}{\partial\tau} = \nabla'^2\phi_s \tag{A.23}$$

where the reduce time, $\tau = D_0 t/l^2$, reduce size, $X = r/l$, and $\Delta' = l\Delta$ are dimensionless variables, $\delta = \alpha l D_s(\phi_f)/2aD_0$ and $K = (2\gamma a^2/kT)a/l$ are parameters. δ is dimensionless growth velocity which determines the growth rate. l is the scale length in space. l can be any length, but it was found that it is convenient to set l as the initial nucleus size obtained in the experiment.

Results

The equations of the model are solved numerically with a computor. The results are following. There exists a critical nucleus size. The nucleus only grows

when greater than critical size, r^*. There is a kinetic parameter, δ, the dimensionless growth velocity contral the growth of the crystals. For large δ, the crystal dimemtion grows as $t^{1/2}$ (diffusion limited growth) in the coexistence region, but grows proportional to t (interface limited growth) above melting. For small δ, the growth appreximate a power law behavior intermediating between diffusion and interface limited growth. The crystal increases in density (volume fraction) as δ is reduced due to osmotic compression by the metastable fluid. This agrees with the observation in the experiment of Harland[11].

BIBLIOGRAPHY

1. W. B. Russel, Phase Transitions **21**, 127 (1990).
2. B. J. Ackerson and K. Schätzel, Phys. Rev. E **52**, 6448, (1995).
3. M. M. Kops Werkhoven and H. M. Fijnaut, J. Chem. Phys. **74**, 1618, (1981).
4. M. M. Kops Werkhoven and H. M. Fijnaut, J. Chcm. Phys. **77**, 2242, (1982).
5. W. van Megen, S. M. Owens, R. H. Ottewill, and P. N. Pusey, J. Chem. Phys. bf 82, 508, (1985).
6. R. Pecora, Ed. , it Dynamic Light Scattering (Plenum, New York, 1985).
7. Pusey and R. A. Tough, in *Dynamic Light Scattering: Applications of Photo Correlation Spectroscopy* edited by R. Pecora, 85, (1985).
8. W. B. Russel, D. A. Saville and W. R. Schowalter, Colloidal Dispersion, Cambridge University Press, Cambridge, (1989).
9. A. H. van Veluwen, H. N. W. Lekkerkerker, C. G. de Kruif, and A. Vrij, J. Chem. Phys. **87**, 4873, (1987).
10. J. S. van Duijneveldt and H. N. W. Lekkerkerker, in *Science and Technology of Crystal Growth*, edited by J. P. Erde and O. S. L. Bruinsma (Kluwer Academic, Dordrecht, 1995).
11. J. L. Harland, S. I. Henderson, S. M. Underwood and W. van Megen, Phys. Rev. Lett. **75**, 3572, (1995).
12. W. van Megen and S. M. Underwood, Phys. Rev. E **49**, 4206, (1994).
13. J. Frenkel, *Kinetic Theory of Liquids*, Oxford University Press, Oxford, 1964.
14. D. W. Marr and A. P. Gast, Phys. Rev. E **47**, 1212, (1993).
15. L. V. Woodcock, Ann. N. Y. Acad. Sci., **37**, 274, (1981).
16. K. R. Hall, J. Chem. Phys. **57**, 2252, (1972).
17. W. G. Hoover and F. H. Ree, J. Chem. Phys. **49**, 635, (1968).
18. J. W. Gibbs, *Collected Works*, (Yale University Press, New York,1948).
19. H. A. Wilson, Philos. Mag. **50**, 238, (1900).

VITA

YUEMING HE

Candidate for the Degree of

Doctor of Philosophy

Thesis: CRYSTALLIZATION IN HARD SPHERE COLLOIDAL SYSTEMS

Major Field: Physics

Biographical:

Personal Data: Born in Guangzhou, China, on January 18, 1960, the son of Chengxi and Xiuxian He.

Education: Received Bachelor of Science degree in Physics from South China Normal University, Guangzhou, China in 1983; received Master of Science Degree in Modern Optics from South China Normal University, Guangzhou, Chian in 1987; completed the requirements for the Doctor of Philosophy Degree at the Oklahoma State University, Stillwater, Oklahoma, December, 1996.

Professional Experience: Graduate Teaching and Research Assistant, Oklahoma State University, September 1990 to September 1995.